POLITECNICO DI TORINO

Master's Degree Course in Aerospace Engineering

Master's Degree Thesis

Numerical Analysis of Hypersonic Intakes for Airbreathing Propulsion Systems

Supervisors:
Prof. Andrea Ferrero
Dr. Bayindir Huseyin Saracoglu

Candidate:
Luigi Bellomo
S319837

ACADEMIC YEAR 2024/2025

Acknowledgements

I would like to express my sincere gratitude to Dr. Bayindir for giving me the opportunity to carry out this thesis work at the Von Karman Institute for Fluid Dynamics. His guidance has been fundamental in shaping this academic journey, and his passion for the field has greatly inspired my own.

I am also thankful to Professor Andrea Ferrero, whose course "Computational Fluid Dynamics for Propulsion Systems" introduced me to the fascinating world of fluid dynamics. His teaching sparked a deep interest in the subject that has since become a true academic passion.

Finally, I wish to extend my thanks to the entire Von Karman Institute, a stimulating and supportive environment that continuously motivated me to give my best throughout this experience.

Abstract

Ramjet and scramjet engines represent a key technology for high-speed airbreathing propulsion due to their ability to operate efficiently at supersonic and hypersonic speeds without requiring rotating parts. A crucial component of these engines is the air intake, which is responsible for compressing the incoming airflow through shock waves before combustion. The design of an efficient intake significantly affects the overall performance of the propulsion system. This thesis focuses on the design, analysis, and optimization of hypersonic intakes, with particular attention to the *Busemann intake*, which is known for its high efficiency in the inviscid flow regime.

The initial phase of this research involves the numerical generation of intake geometries using a MATLAB-based design algorithm. The intake configuration is defined by key parameters, including the freestream Mach number M_∞, the post-shock Mach number M_3, and the intake exit cross-sectional radius r. To evaluate the aerodynamic performance of the designed intakes, Computational Fluid Dynamics (CFD) simulations are performed in *Ansys Fluent*, solving the Navier-Stokes equations for an initial two-dimensional model, where geometric variations are analyzed to evaluate their impact on performance, flow uniformity, and startability.

Given that real-world applications deviate from the ideal inviscid model, additional *viscous corrections* are applied to account for boundary layer effects. These corrections address the increased pressure ratios relative to the ideal case and the reduction in intake efficiency caused by boundary layer-induced flow distortion. The correction methodology involves computing the boundary layer displacement thickness using Reynolds-Averaged Navier-Stokes (RANS) simulations and integrating it into the ideal inviscid design. Moreover, *truncated intake designs* are explored to mitigate the excessive length of the classical Busemann intake while maintaining optimal aerodynamic performance.

Following the optimization of the two-dimensional intake contour, a three-dimensional counterpart is generated using the *Wavecatching technique*, which traces streamlines to adapt the intake to an elliptical cross-section. A *mesh convergence study* is carried out for both 2D and 3D cases to ensure the reliability of numerical results. Finally, the off-design performance of the 3D intake is analyzed to evaluate the system's response to varying operating conditions. This analysis helps identify configurations that exhibit greater robustness against *unstart phenomena* and offer improved efficiency across a wider range of Mach numbers.

The results confirm the feasibility of the developed design methodology, demonstrating that the proposed intake geometries maintain high efficiency while addressing real-world constraints such as viscosity, manufacturability, and operational robustness.

Contents

Chapter 1

Introduction

1.1 General overview

The ambition to achieve hypersonic flight within the atmosphere has been a source of inspiration for generations of aerodynamicists, scientists, and engineers. By the late 1950s and early 1960s, it became evident that while rocket propulsion could enable space access and global reach via ballistic trajectories, only an airbreathing propulsion system had the potential to support sustained and practical hypersonic flight within the Earth's atmosphere.

The scramjet (supersonic combustion ramjet) engine represents a significant advancement in hypersonic airbreathing propulsion, offering a more efficient way of achieving high-speed atmospheric flight compared to traditional rocket propulsion. Unlike turbojets, which rely on mechanical compressors, and rockets, which must carry onboard oxidizers, scramjets use shock wave compression within the intake to decelerate and compress incoming air before combustion. This eliminates the need for moving parts, enhancing reliability and efficiency at supersonic and hypersonic speeds.

The fundamental advantage of scramjet propulsion lies in its higher specific impulse compared to chemical rockets. Since scramjets derive oxygen from the atmosphere instead of carrying it onboard, they achieve superior fuel efficiency, making them ideal for sustained hypersonic flight. Moreover, scramjets operate effectively within the atmosphere, allowing for greater maneuverability than rockets, which are limited to ballistic trajectories.

At speeds above Mach 5, conventional ramjets (which rely on subsonic combustion) are subject to increasing shock losses due to the necessity of decelerating supersonic airflow to subsonic speeds prior to combustion. This process gives rise to the generation of stronger shock waves, resulting in higher pressure losses within the intake, while also causing extremely high combustor temperatures. These effects lead to significant energy dissipation and impose structural limitations on the engine. Scramjets, by allowing supersonic airflow through the combustor, overcome these issues, enabling more efficient combustion and sustained propulsion at hypersonic speeds. This technology has the potential to revolutionize transcontinental travel, reducing flight times, while also playing a pivotal role in space access through air-breathing launch vehicles.

The operational flight corridor for scramjet-powered vehicles, for both cruise flight and ascent to low Earth orbit, is constrained by two primary factors. At higher altitudes, the limitation arises from the need to maintain sufficient air density to ensure an adequate mass flow rate for airbreathing propulsion. At lower altitudes, the constraint is dictated by the structural limits of the vehicle, primarily due to aerodynamic heating and mechanical stresses.
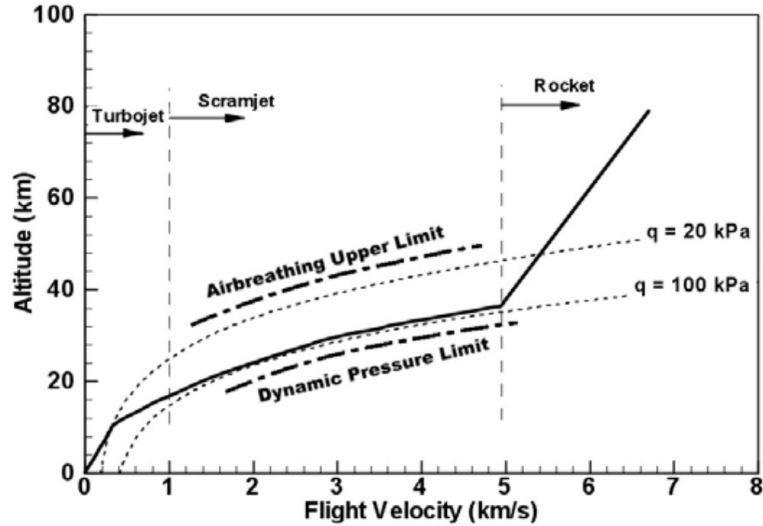

Figure 1.1: Hypersonic airbreathing flight corridor [1].

As illustrated in Figure 1.1, these operational boundaries are delineated, and a proposed ascent trajectory for an airbreathing access-to-space vehicle is presented. The trajectory involves the utilisation of turbojet propulsion up to Mach 3-4, followed by a transition to scramjet operation up to Mach 15-17, and subsequently to rocket-based propulsion for the final stage. This sequence ensures the requisite acceleration to achieve a low Earth orbital velocity of approximately 7.9 km/s [1].

A critical component of scramjet operation is the air intake, which must effectively compress and condition the incoming airflow for optimal combustion. The design and efficiency of the intake directly impact engine performance, influencing parameters such as:

- Compression ratio: Ensuring sufficient pressure increase for effective combustion.

- Flow uniformity: Maintaining a stable, predictable airflow distribution.

- Minimization of losses: Reducing total pressure losses to enhance efficiency.

At hypersonic speeds, intake efficiency must be maximized to minimize chemical non-equilibrium effects in the combustor and nozzle. However, designing a scramjet intake presents challenges due to the interdependence between the engine and airframe. Unlike conventional aircraft, scramjet-powered vehicles integrate the engine into the lower

fuselage, where it contributes significantly to lift, drag, and aerodynamic forces. This integration makes intake geometry optimization essential for balancing aerodynamic and propulsion performance.

Despite its advantages, scramjet technology faces several challenges:

1. Startability: Ensuring that the engine can transition smoothly from subsonic to supersonic combustion without excessive losses or instability.

2. Thermal Management: Hypersonic speeds expose the vehicle to extreme aerodynamic heating, requiring advanced materials and cooling techniques.

3. Off-Design Performance: Maintaining efficiency across a range of flight conditions remains difficult due to the fixed-geometry nature of most current scramjet intakes.

4. Integration with Space Launch Vehicles: For scramjets to support reusable space access, they must work in combination with other propulsion systems, such as rocket-based combined cycle (RBCC) engines.

Recent flight tests, including NASA's X-43A and X-51A programs Fig. 1.2, have demonstrated successful scramjet operation, proving the feasibility of sustained hypersonic propulsion. Future research is focusing on combined cycle engines, which integrate scramjets with turbojets and rockets to expand operational ranges, enabling efficient air-breathing propulsion from take-off to orbital insertion.

Figure 1.2: NASA X-43A [2].
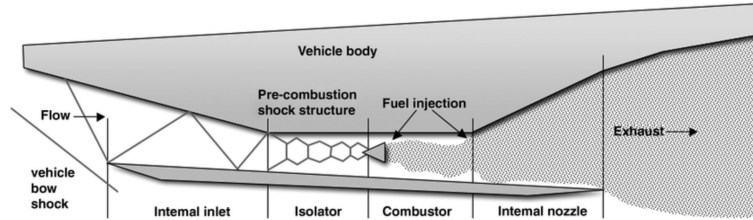
1.2 Hypersonic intakes

Figure 1.3: Schematic of vehicle-integrated scramjet engine [3].

A scramjet engine, as illustrated in Fig. 1.3, consists of four primary components: an inlet, an isolator, a combustor, and a nozzle. The inlet plays a fundamental role in the engine's performance, as it is responsible for compressing and decelerating the freestream air before it enters the combustor. This process is achieved through a combination of isentropic compression and oblique shock waves, ensuring that the airflow attains a sufficiently high static temperature ratio (typically in the range of 6–8) while maintaining an optimal thermodynamic cycle efficiency [4]. Additionally, the inlet must generate pressure and temperature levels adequate to sustain complete and stable combustion at supersonic speeds.

The isolator serves to separate the supersonic inlet flow from the backpressure fluctuations that arise in the combustor, mitigating disturbances that could otherwise compromise stability. Following compression, the airflow enters the combustor, where fuel is injected, mixed, and ignited while maintaining supersonic conditions. The challenge of supersonic combustion lies in the extremely short residence time of the airflow within the combustor. For instance, if the airflow velocity is 999 m/s (Mach 3), it would traverse a 1-meter-long chamber in just 1 ms. Given these constraints, achieving efficient fuel injection, mixing, and combustion requires sophisticated design strategies, which are beyond the scope of this study. The nozzle then expands and accelerates the hot gases, converting thermal energy into thrust.

For optimal engine performance, the intake must compress the airflow with minimal losses. The effectiveness of an inlet is evaluated based on both its performance and efficiency, which can be quantified using the following parameters:

- Compression ratio: The pressure ratio between the inlet and outlet.

- Contraction ratio: The ratio of inlet-to-exit flow areas.

- Mach number reduction: The ratio of inlet and exit Mach numbers.

- Total pressure recovery: A measure of how efficiently the intake preserves total pressure.

These parameters are strongly influenced by the geometry of the intake and are governed by the first and second law of thermodynamic.

For high-speed airbreathing engines, such as scramjets, thermodynamic cycle analyses indicate that intakes must provide contraction ratios between 6 and 20, while ensuring

minimal total pressure losses [5]. The choice of intake geometry is particularly critical, as it directly influences not only the shape of the engine but also the overall aircraft design. The airframe and propulsion system are deeply interconnected, with structural and thermal loads playing a key role in defining the intake configuration. Consequently, intake design significantly impacts the shape of the aircraft, requiring an integrated design approach. Given these interdependencies, the intake design process typically starts with simple compressive flow models that are analytically predictable and serve as a solid foundation for optimization. The simple flow models considered in intake design are primarily supersonic flows exhibiting either planar or axial symmetry. In planar flows, flow properties remain uniform within parallel geometric planes, whereas in axial flows, these properties are invariant across planes surrounding a common axis [6]. The presence of planar or axial symmetry significantly simplifies the flow characterization, reducing the number of independent spatial variables required for analysis from three to two, thereby streamlining both design and computational modelling.

Additionally, these flows often exhibit radial symmetry, meaning that in planar configurations, flow properties remain unchanged along flat surfaces, while in conical Taylor-Maccoll flows, they are consistent along cone surfaces. By incorporating flat plate models alongside conical symmetry, the number of variables necessary to fully describe the flow can be further reduced to just one, allowing for an even more simplified intake design process.

Among the most commonly employed simple planar flow models, oblique shock wave interactions and Prandtl-Meyer (P-M) expansion flows are frequently utilized due to their well-defined characteristics and predictable behavior. In contrast, axial flows, such as those occurring over conical surfaces, often rely on the Busemann flow model, which is particularly advantageous for hypersonic intakes. Notably, these simple flow models and their combinations do not generate curved shocks within the intake flow field, ensuring that the internal flow remains irrotational and uniform, which is essential for maximizing compression efficiency and minimizing total pressure losses.

To further refine intake performance, wavecatching techniques are employed. This method involves selecting specific streamlines from analytically known supersonic flows and using them to construct an optimized intake flow path. The resulting intake geometries enhance shock wave interactions, boundary layer control, and structural constraints, ultimately leading to maximum compression efficiency with minimal pressure losses.

1.2.1 Planar and axial flows

In an axisymmetric intake, flow convergence, rather than flow turning, serves as the primary mechanism for compressing the incoming air. Within a supersonic convergent duct, the flow—assuming it behaves isentropically—undergoes deceleration, leading to a Mach number reduction and the formation of a weak oblique shock at the intake's exit. This process enables high compression efficiency while minimizing shock-induced losses. The defining characteristic of an axial flow intake is its internal converging flow field, which plays a crucial role in maintaining efficient compression.

The incorporation of leading-edge truncation and wavecatching techniques offers significant advantages in terms of flow starting and minimizing viscous losses. Notably,

these methods ensure that high adverse pressure gradients are absent from the wall surface boundary layer, instead being confined to the inviscid core flow, thereby improving overall intake performance. Due to their high efficiency, hypersonic intakes featuring well-defined entrance and exit geometries have been extensively studied. These designs typically employ simple axisymmetric compressive flows to achieve optimal aerodynamic performance [7], [8].

A circular cross-section is often the preferred geometry for ramjet and scramjet combustors due to its structural and thermal advantages. A cylindrical shape is inherently more resistant to heat and pressure loads, while also minimizing frictional losses since a cylinder—given the same cross-sectional area—has the smallest surface area. Consequently, a cylindrical and axially symmetric geometry emerges as an optimal configuration for an intake positioned ahead of the combustor.

Given these considerations, it is particularly relevant to analyze axisymmetric flow behavior for hypersonic intake design. A streamtube geometry that satisfies the geometric, structural, and aerodynamic constraints can be effectively derived from axisymmetric and conical Taylor-Maccoll (T-M) flow, which provides an analytically predictable model for compressive intake flowfields [9], [10].

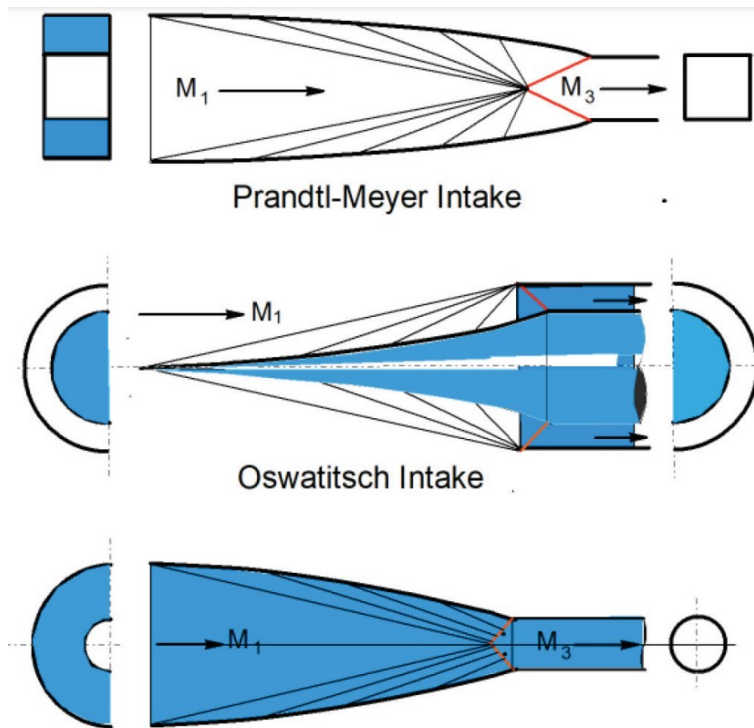### 1.2.2   Intake flow processes and types of inlets

Figure 1.4: Schematic of three hypersonic intakes [11].

Various fundamental flow mechanisms contribute to the reduction of Mach number within hypersonic intakes. These mechanisms can be categorized as follows: compressive flow turning, area contraction due to a converging passage, and flow deflection through oblique shock waves. While isentropic processes, such as flow turning and area contraction, result in no efficiency losses, flow deflection via oblique shocks introduces entropy generation, thereby reducing intake efficiency.

Since flow deflection through shock waves is often necessary, it is desirable to maintain shock strength as weak as possible to minimize losses. This can be achieved by ensuring that shocks occur at lower Mach numbers. In planar Prandtl-Meyer type flows, significant flow turning is required to achieve an exit flow parallel to the freestream, necessitating strong oblique shocks. In contrast, in an axial flow configuration, Mach number reduction is achieved primarily through area contraction, with minimal flow turning. A prime example of this approach is the Busemann flow, where compression is largely accomplished through flow convergence, rather than significant turning, thereby reducing the necessity for shock deflection. Furthermore, since Mach number reduction is substantial in Busemann flow, the rear-end oblique shock interacts with a lower Mach number flow, producing a weak shock and minimizing efficiency losses. This characteristic explains the high efficiency of Busemann intakes.

In general, intake flow classifications can be described using the concepts of flow convergence, flow turning, and flow deflection [11]. The Prandtl-Meyer flow is particularly suitable for planar configurations with variable geometry, as it provides efficient flow turning despite introducing efficiency losses due to oblique shock interactions. In contrast, isentropic flow convergence, which does not involve turning, offers an alternative method for Mach number reduction without introducing additional irreversibilities. Ideally, shock-induced flow deflection should be used only when necessary, as it represents a non-isentropic process that inherently introduces losses. The Busemann flow is an example that integrates all three of these compression mechanisms.

The three primary compression modes—the Prandtl-Meyer intake, the Oswatitsch intake, and the Busemann intake—are illustrated in Figure 1.4. To compare their performance, three intake designs were developed to achieve a Mach number reduction from 8.33 to 4.8, considering a static pressure ratio of 26.8. Experimental validation was conducted in a gun tunnel at Mach 8.33 [9]. The inviscid total pressure recovery values for the Busemann, Oswatitsch, and Prandtl-Meyer intakes were found to be 0.983, 0.763, and 0.763, respectively. However, experimental measurements yielded 0.484, 0.485, and 0.240, respectively. The discrepancy observed in the Prandtl-Meyer intake is attributed to its larger surface area, which increased viscous losses.

These results clearly demonstrate the superiority of axial flow-based Mach number reduction over planar flow-based configurations, primarily due to the greater efficiency of flow convergence. Consequently, this study focuses exclusively on the Busemann intake, which is based on axial flow compression rather than planar flow mechanisms, ensuring higher efficiency and reduced total pressure losses.

Prandtl-Meyer intake

Figure 1.5: Prandtl-Meyer intake mounted on Concorde [12].

The performance characteristics of the Prandtl-Meyer intake are primarily derived from a combination of isentropic flow turning through a compression fan, followed by flow deflection via an oblique shock. Notably, this type of intake does not incorporate flow convergence as a compression mechanism.

A practical example of an aircraft utilizing this intake configuration is the Concorde, which demonstrated exceptionally high performance, mechanical simplicity, and operational robustness. Additionally, its control system remained inactive for the majority of the flight, highlighting the intake's passive adaptability across various operating conditions. A comprehensive overview of the design methodology can be found in [13], while detailed geometric specifications are provided in [14].

Oswatitsch intake

Figure 1.6: Oswatitsch intake mounted on a missile [15].

The Oswatitsch intake exemplifies a flow configuration where flow divergence is followed by deflection through a shock wave. Compression in this intake design is achieved through either a single external shock or a series of multiple shocks. As demonstrated in [16], maximum pressure recovery is obtained when the shocks in a multi-shock system are of equal strength.

The number of ramps and corresponding shock waves directly influences both the degree of flow turning and the level of internal contraction, thereby impacting overall intake efficiency. A notable historical example of the Oswatitsch intake in practical application is found in the Trommsdorff projectiles utilized during World War II [17].

Busemann intake

Figure 1.7: Four-module Busemann intake [18].

Regarding the Busemann intake, the flow undergoes both turning and convergence before being deflected by a shock wave. In his foundational work, Busemann analytically demonstrated the feasibility of a supersonic, uniform, axial flow that undergoes isentropic compression, followed by shock-induced deceleration, resulting in a uniform subsonic flow.

The performance characteristics of the Busemann intake have been extensively investigated, with Mölder and Van Wie [19] proposing its application to flight vehicles. A notable practical implementation can be found in the JHU/APL missile-type intake [20], which employed a four-module design based on the streamline tracing approach, Figure 1.7. This intake was integrated into a scramjet engine and successfully launched in Barbados in 1972. Further refinement and analysis of the four-module intake were conducted by Matthews and Jones [21], who explored its aerodynamic performance and design optimizations.

1.3 Objective of the thesis

The objective of this thesis is to design, analyze, and optimize hypersonic air intakes, with a particular focus on the Busemann intake, recognized for its high aerodynamic efficiency. The study begins with the numerical generation of intake geometries using a MATLAB-based design algorithm, where key parameters define the intake configuration.

Following this, a two-dimensional analysis is conducted through Computational Fluid Dynamics (CFD) simulations in Ansys Fluent, investigating various geometric variations to assess their impact on aerodynamic performance. Given that real-world applications deviate from ideal inviscid conditions, the study also incorporates viscous corrections to account for boundary layer effects, ensuring a more accurate representation of intake behavior.

Once the optimized intake geometry was obtained, a three-dimensional analysis was conducted to evaluate its performance under on-design boundary conditions. In addition, the intake was tested under various off-design scenarios using multiple configurations of the 3D design. This analysis aimed to identify which configurations offer greater robustness and efficiency across a wider operational envelope.

Chapter 2

Theoretical background

This chapter presents a theoretical introduction to the underlying physics relevant to this study. For a more comprehensive treatment of aerodynamics, refer to the relevant literature [22], [23].

2.1   One-Dimensional Flow

By definition, a one-dimensional flow is one in which the flow field properties vary only with one coordinate direction. A truly one-dimensional flow is illustrated in the left side of Fig. 2.1 , where the flowfield variables are a function of x only, and as a consequence the streamtube area must be constant. On the other hand, there are many flow problems where the streamtube area varies with x $(A(x))$, as shown in the left side of Fig. 2.1. For such a variable area streamtube, nature dictates that the flowfield is three-dimensional flow, where the flow properties in general are function of x, y and z. However, if the variation of area $A = A(x)$ is gradual, it is often convenient and sufficiently accurate to neglect the y and z variations, and to assume that the flow properties are functions of x only. Such a flow is defines as *quasi-one-dimensional flow.*
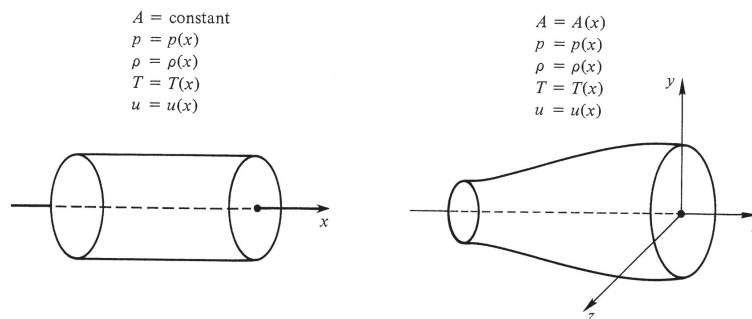

$$A = \text{constant}$$
$$p = p(x)$$
$$\rho = \rho(x)$$
$$T = T(x)$$
$$u = u(x)$$

$$A = A(x)$$
$$p = p(x)$$
$$\rho = \rho(x)$$
$$T = T(x)$$
$$u = u(x)$$

Figure 2.1: Comparison between one-dimensional and quasi-one-dimensional flows [22].
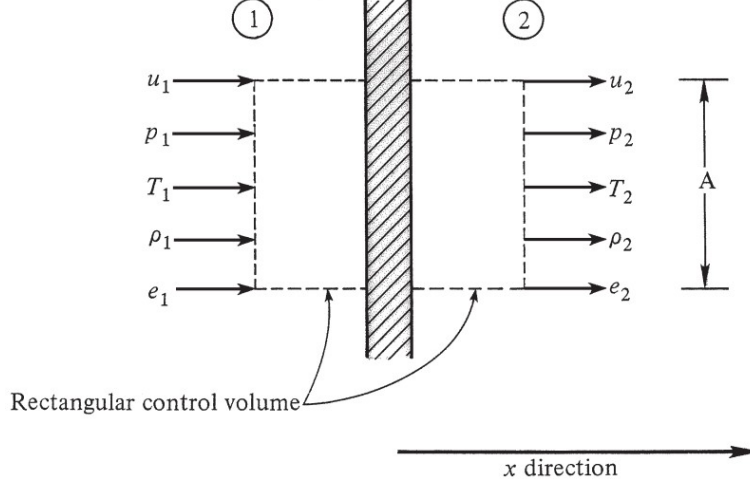
One-Dimensional flow equations

Figure 2.2: Rectangular control volume for one-dimensional flow [22].

Consider the flow through one-dimensional region, as represented by the shaded area in Fig. 2.2. This region may be a normal shock wave, or it may be a region with heat addition; in either case, the flow properties change as a function of x as the gas flows through the region. To calculate the changes, apply the integral conservation equations to the rectangular control volume shown by the dashed lines in Fig. 2.2. Since the flow is one-dimensional, u_1, p_1, T_1, ρ_1 and e_1 are uniform over the left-hand side of the control volume, as well as u_2, p_2, T_2, ρ_2, and e_2 are uniform over the right-hand side of the control volume. Assume that the left and right hand sides each have an area equal to A perpendicular to the flow. Also, assume that the flow is *steady*, such that all derivatives with respect to time are zero, and assume that body forces are not present. With this assumptions, the continuity equation:

$$\frac{\partial}{\partial t} \int_{\text{Vol}} \rho \, d\text{Vol} = - \int_S \rho(\overline{V} \cdot \bar{n}) \, dS \tag{2.1}$$

For steady flow, Eq. (2.1) becomes

$$\int_S \rho(\overline{V} \cdot \bar{n}) \, dS = 0 \tag{2.2}$$

Evaluating the surface integrals on the left-hand side, where V and dS are parallel but in opposite directions, yields $-\rho_1 u_1 A$; on the right-hand side, where V and dS are parallel and in the same direction, the result is $\rho_2 u_2 A$. The upper and lower horizontal faces of the control volume both contribute nothing to the surface integral because V and dS are perpendicular to each other on these faces. Hence, from Eq. (2.2),

$$\rho_1 u_1 = \rho_2 u_2 \tag{2.3}$$

Equation (2.3) is the *continuity equation* for steady one-dimensional flow.

18

The momentum equation:

$$\frac{\partial}{\partial t}\int_{\text{Vol}}\rho\bar{V}\,d\text{Vol}+\int_{\text{S}}\rho\bar{V}(\bar{V}\cdot\bar{n})\,dS=-\int_{\text{S}}(p\cdot\bar{n})\,dS+\int_{\text{Vol}}\rho\bar{f}\,d\text{Vol} \tag{2.4}$$

The first term is zero because steady flow is considered. Also, because there are no body forces, the last term is zero. Hence, Eq. (2.4) becomes:

$$\int_{\text{S}}\rho\bar{V}(\bar{V}\cdot\bar{n})\,dS=-\int_{\text{S}}(p\cdot\bar{n})\,dS \tag{2.5}$$

Equation (2.5) is a vector equation. However, since the analysis is conducted under the assumption of one-dimensional flow, only the scalar x component of Eq. (2.5) needs to be considered, which is

$$\int_{\text{S}}\rho\bar{V}(\bar{V}\cdot\bar{n})\,dS=-\int_{\text{S}}((p\cdot\bar{n})\,dS)_x \tag{2.6}$$

In Eq. (2.6), the expression $((p\cdot\bar{n})\,dS)_x$ is the x component of the vector $(p\cdot\bar{n})\,dS$. Evaluating the surface integrals in Eq, (2.6) over the left and right hand sides of the dashed control volume in Fig. 2.2, it can be obtained

$$p_1+\rho_1 u_1^2=p_2+\rho_2 u_2^2 \tag{2.7}$$

Equation (2.7) is the *momentum equation* for steady one-dimensional flow.

The energy equation:

$$\frac{\partial}{\partial t}\int_{\text{Vol}}\rho\left(e+\frac{V^2}{2}\right)d\text{Vol}+\int_{\text{S}}\rho\left(e+\frac{V^2}{2}\right)(\bar{V}\cdot\bar{n})\,dS$$
$$=-\int_{\text{S}}p(\bar{V}\cdot\bar{n})\,dS+\int_{\text{Vol}}\rho(\bar{f}\cdot\bar{V})\,d\text{Vol}+\int_{\text{Vol}}\rho\dot{q}\,d\text{Vol} \tag{2.8}$$

The first and the fourth terms are zero because of steady flow and zero body forces, respectively. The last term physically represents the total rate of heat added to the gas inside the control volume. For simplicity, this volume integral is denoted by $\dot{Q}$. Hence, Eq. (2.8) becomes

$$\int_{\text{S}}\rho\left(e+\frac{V^2}{2}\right)(\bar{V}\cdot\bar{n})\,dS=-\int_{\text{S}}p(\bar{V}\cdot\bar{n})\,dS+\dot{Q} \tag{2.9}$$

Evaluating the surface integrals over the left and right hand faces on the control volume in Fig. 2.2 , dividing by Eq. (2.3) and recalling the definition of enthalpy, $h=e+pv$, Eq. (2.9) becomes

$$h_1+\frac{u_1^2}{2}+q=h_2+\frac{u_2^2}{2} \tag{2.10}$$

Equation (2.10) is the *energy equation* for steady one-dimensional flow.

In summary, Eqs. (2.3), (2.7) and (2.10) are the governing fundamental equations for steady one-dimensional flow. They are algebraic equations that relate properties at two different locations, 1 and 2, along a one-dimensional, constant-area flow. The assumption

of one-dimensionality has afforded a great simplification over the integral equations (2.1) (2.4) (2.8). However, within the assumption of steady one-dimensional flow, the algebraic Eqs. (2.3), (2.7) and (2.10) still represent the full authority and power of the integral equations, i.e. they still say that mass is conserved, force equals time rate of change of momentum and energy is conserved.

2.2   Isentropic relation and total condition

Consider again Eq. (2.10). Assuming no heat addition, this becomes

$$h_1 + \frac{u_1^2}{2} = h_2 + \frac{u_2^2}{2} \tag{2.11}$$

where points 1 and 2 correspond to the region 1 and 2 identified in Fig. 2.2. Applying the equations to a calorically perfect gas, where $h = c_p T$, Eq. (2.11) becomes

$$c_p T_1 + \frac{u_1^2}{2} = c_p T_2 + \frac{u_2^2}{2} \tag{2.12}$$

where

$$c_p = \frac{\gamma R}{\gamma - 1} \tag{2.13}$$

and Eq. (2.11) becomes

$$\frac{\gamma R T_1}{\gamma - 1} + \frac{u_1^2}{2} = \frac{\gamma R T_2}{\gamma - 1} + \frac{u_2^2}{2} \tag{2.14}$$

Since $a = \sqrt{\gamma R T}$, Eq. (2.14) becomes

$$\frac{a_1^2}{\gamma - 1} + \frac{u_1^2}{2} = \frac{a_2^2}{\gamma - 1} + \frac{u_2^2}{2} \tag{2.15}$$

By definition of *total conditions*, consider a fluid element at point A with velocity, temperature and pressure V, T, and p respectively. If this fluid element is *isentropically* decelerated to zero velocity, i.e., brought to a stagnation state, the pressure and temperature attained at $V = 0$ are defined as *total pressure* p_0 and *total temperature* T_0, respectively. If T and u are the actual values of static temperature and velocity, respectively, at point A, then $T_1 = T$ and $u_1 = u$. Also, by definition of total conditions, $u_2 = 0$ and $T_2 = T_0$. Hence, Eq. (2.11) becomes

$$c_p T + \frac{u_2}{2} = c_p T_0 \tag{2.16}$$

Equation (2.16) provides a formula from which the defined total temperature T_0 can be calculated for the given actual conditions of T and u at any point in a general flowfield. However, in the derivation of Eq. (2.16), only the energy equation for an adiabatic flow is used. Isentropic conditions have not been imposed so far. Hence, the definition of T_0 such as expressed in Eq. (2.16) is less restrictive than the definition of total condition given above. Isentropic flow implies reversible and adiabatic conditions. Eq. (2.16) tells

that, for the definition of T_0, only the adiabatic portion of the isentropic definition is required. Now it can be redefined T_0 as that temperature that would exist if the fluid element were brought to rest *adiabatically*. However, for the definition of total pressure p_0, and total density ρ_0, the imagined isentropic process is still necessary. Several useful equations for total conditions are obtained below

$$\frac{T_0}{T} = 1 + \frac{u^2}{2c_pT} = 1 + \frac{u^2}{\frac{2\gamma RT}{(\gamma-1)}} = 1 + \frac{u^2}{\frac{2a^2}{(\gamma-1)}} = 1 + \frac{\gamma-1}{2}\left(\frac{u}{a}\right)^2 \tag{2.17}$$

Hence,

$$\frac{T_0}{T} = 1 + \frac{\gamma-1}{2}M^2 \tag{2.18}$$

Equation (2.18) gives the ratio of total to static temperature at a point in a flow as a function of the Mach number M at that point. Furthermore, for an isentropic process

$$\frac{p_0}{p} = \left(\frac{\rho_0}{\rho}\right)^\gamma = \left(\frac{T_0}{T}\right)^{\frac{\gamma}{\gamma-1}} \tag{2.19}$$

Combining Eqs. (2.18) and (2.19), it can be found

$$\frac{p_0}{p} = \left(1 + \frac{\gamma-1}{2}M^2\right)^{\frac{\gamma}{\gamma-1}} \tag{2.20}$$

$$\frac{\rho_0}{\rho} = \left(1 + \frac{\gamma-1}{2}M^2\right)^{\frac{1}{\gamma-1}} \tag{2.21}$$

Equations (2.20) and (2.21) give the ratios of total to static pressure and density, respectively, at a point in the flow as a function of Mach number M at that point. The flowfield itself does not need to be adiabatic or isentropic from one location to another. Rather, the isentropic process is used conceptually to define the total conditions at a specific point. If the actual flow between A and B is non adiabatic and irreversible, then $T_{0_A} \neq T_{0_B}$, $p_{0_A} \neq p_{0_B}$, and $\rho_{0_A} \neq \rho_{0_B}$. On the other hand, if the general flowfield is isentropic throughout, then T_0, p_0, and ρ_0 are constant values at every point in the flow.

2.3 Quasi-One-dimensional Flow

$A = A(x)$
$u = u(x)$
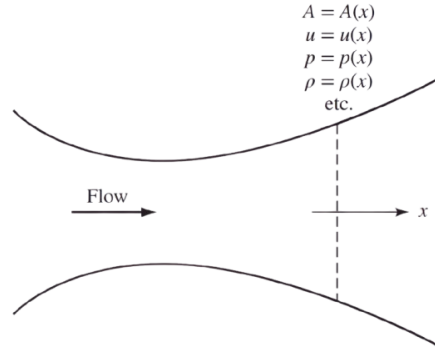$p = p(x)$
$\rho = \rho(x)$
etc.

Flow

x

Figure 2.3: Quasi-one-dimensional flow[22].

In Sec. 2.1 one-dimensional flow was treated as strictly constant-area flow. In the present section, this restriction will be relaxed by allowing the streamtube area A to vary with distance x, as shown in Figs. 2.1 and 2.3. The flow is considered to have uniform properties across each cross-sectional area, implying that all variables are functions solely of x and, if the flow is unsteady, also of time t. Such a flow, where $A = A(x)$, $p = p(x)$, $\rho = \rho(x)$ and $V = u = u(x)$ for steady flow, is defined as *quasi-one-dimensional flow.* For this flow, it is the area change that causes the flow properties to vary as a function of x. However, quasi-one-dimensional flow is an approximation; the flow in the variable-area streamtube is three-dimensional, but for a wide variety of engineering problems, quasi-one-dimensional results are frequently sufficient.

2.3.1 Governing Equations

To understand the physical implications of the quasi-one-dimensional flow assumption, consider the actual three-dimensional flow through a variable-area duct, as illustrated in Fig. 2.1. In this case, the flow properties exhibit spatial variations in all three coordinate directions: x, y, and z. However, under the quasi-one-dimensional assumption, as depicted in Fig. 2.3, the flow properties are considered to vary solely as a function of the streamwise coordinate x, i.e., $u = u(x)$, $p = p(x)$, etc. This implies that the flow properties are assumed to be uniform across any cross-sectional area A, effectively representing some averaged value of the actual distribution of flow variables over the cross-section.

It is important to recognize that quasi-one-dimensional flow is an approximation of the actual physical behavior of the flow. However, despite this simplification, the governing equations derived for quasi-one-dimensional flow rigorously satisfy the fundamental conservation principles, including mass conservation, Newton's second law, and the first law of thermodynamics. Therefore, while the physical model is an approximation, the resulting equations remain exact representations of these fundamental conservation laws.

Crucially, the equations formulated in this section strictly enforce the fundamental conservation principles without any compromise in the overall physical consistency of the

flow. This is achieved by employing the integral forms of the conservation equations and applying them rigorously to the quasi-one-dimensional flow model shown in Fig. 2.3. The following sections will detail the derivation and application of these equations in a mathematically exact manner.
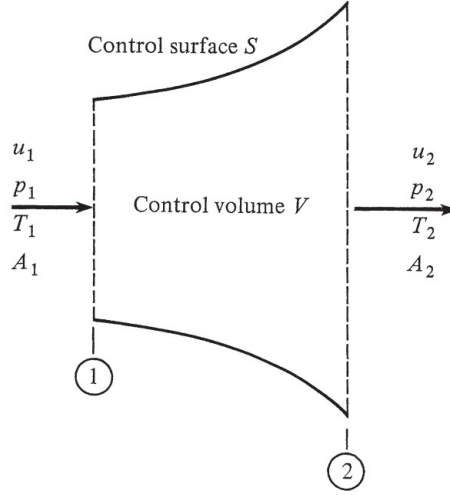

Figure 2.4: Finite control volume for quasi-one-dimensional flow[22].

Algebraic equations for steady quasi-one-dimensional flow can be obtained by applying the integral form of the conservation equations to the variable-area control volume sketched in Fig. 2.4.

The continuity equation

$$\frac{\partial}{\partial t} \int_{\text{Vol}} \rho \, d\text{Vol} = -\int_S \rho(\overline{V} \cdot \bar{n}) \, dS \tag{2.22}$$

when integrated over the control volume in Fig. 2.4 leads, for steady flow, directly to

$$\rho_1 u_1 A_1 = \rho_2 u_2 A_2 \tag{2.23}$$

This is the continuity equation for steady quasi-one-dimensional flow.

The integral form of the momentum equation

$$\frac{\partial}{\partial t} \int_{\text{Vol}} \rho \overline{V} \, d\text{Vol} + \int_S \rho \overline{V}(\overline{V} \cdot \bar{n}) \, dS = -\int_S (p \cdot \bar{n}) \, dS + \int_{\text{Vol}} \rho \bar{f} \, d\text{Vol} \tag{2.24}$$

Applied to Fig. 2.4, assuming steady flow and no body forces, it directly becomes

$$p_1 A_1 + \rho_1 u_1^2 A_1 + \int_{A_1}^{A_2} p \, dA = p_2 A_2 + \rho_2 u_2^2 A_2 \tag{2.25}$$

This is the momentum equation for steady quasi-one-dimensional flow.

The integral form of the energy equation

$$\frac{\partial}{\partial t} \int_{\text{Vol}} \rho \left(e + \frac{V^2}{2} \right) d\text{Vol} + \int_S \rho \left(e + \frac{V^2}{2} \right) (\overline{V} \cdot \bar{n}) \, dS$$
$$= -\int_S p(\overline{V} \cdot \bar{n}) \, dS + \int_{\text{Vol}} \rho(\bar{f} \cdot \overline{V}) \, d\text{Vol} + \int_{\text{Vol}} \rho \dot{q} \, d\text{Vol} \tag{2.26}$$

23

Applied to Fig. 2.4, and assuming steady adiabatic flow with no body forces, it directly yields

$$-(-p_1 u_1 A_1 + p_2 u_2 A_2) = \rho_1 \left(e_1 + \frac{u_1^2}{2}\right)(-u_1 A_1) + \rho_2 \left(e_2 + \frac{u_2^2}{2}\right) u_2 A_2$$

Rearranging,

$$p_1 u_1 A_1 + \rho_1 u_1 A_1 \left(e_1 + \frac{u_1^2}{2}\right) = p_2 u_2 A_2 + \rho_2 u_2 A_2 \left(e_2 + \frac{u_2^2}{2}\right) \tag{2.27}$$

Divide Eq. (2.27) by (2.23):

$$\frac{p_1}{\rho_1} + e_1 + \frac{u_1^2}{2} = \frac{p_2}{\rho_2} + e_2 + \frac{u_2^2}{2} \tag{2.28}$$

Noting that $h = e + \frac{p}{\rho}$, Eq. (2.28) becomes

$$h_1 + \frac{u_1^2}{2} = h_2 + \frac{u_2^2}{2} \tag{2.29}$$

This is the energy equation for steady adiabatic quasi-one-dimensional flow. It states that the total enthalpy is constant along the flow:

$$h_0 = const \tag{2.30}$$

Note that Eqs. (2.29) and (2.30) are identical to the adiabatic one-dimensional energy equation derived in Sec. 2.1. Indeed, this is a general result; in any adiabatic steady flow, the total enthalpy is constant along a streamline.
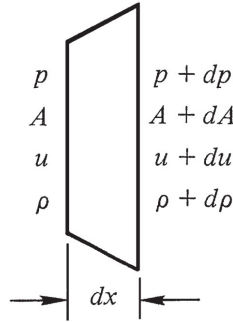
Figure 2.5: Incremental volume[22].

The differential forms of the steady, quasi-one-dimensional continuity, momentum, and energy equations are now expressed as follows. From Eq. (2.23),

$$\rho u A = const$$

Hence,

$$\boxed{d(\rho u A) = 0} \tag{2.31}$$

To obtain a differential form of the momentum equation, Eq. (2.25) is aplied to the infinitesimal control volume sketched in Fig. 2.5, where the length in the x direction is dx:

$$pA + \rho u^2 A + p\, dA = (p + dp)(A + dA) + (\rho + d\rho)(u + du)^2(A + dA)$$

Neglecting all second-order terms involving products of differentials, this becomes

$$A\, dp + Au^2\, dp + \rho u^2\, dA + 2\rho u A\, du = 0 \tag{2.32}$$

Expanding Eq. (2.31), and multiplying by u,

$$\rho u^2\, dA + \rho u A\, du + Au^2\, d\rho = 0$$

Subtracting this equation from Eq. (2.32), yields

$$\boxed{dp = -\rho u du} \tag{2.33}$$

This equation is called *Euler's equation.*

Finally a differential form of the energy equation is obtained from Eq. (2.29) which states that

$$h + \frac{u^2}{2} = const$$

Hence,

$$\boxed{\text{dh} + \text{udu} = 0} \tag{2.34}$$

2.3.2 Area-velocity relation

A significant amount of physical insight into quasi-one-dimensional flow can be derived from a specific combination of the differential forms of the conservation equations introduced at the conclusion of Section 2.3.1. From Eq. (2.31),

$$\frac{d\rho}{\rho} + \frac{du}{u} + \frac{dA}{A} = 0 \tag{2.35}$$

To eliminate $\frac{d\rho}{\rho}$ from Eq. (2.35), Eq. (2.33) is considered:

$$\frac{dp}{p} = \frac{dp}{d\rho}\frac{d\rho}{\rho} = -udu \tag{2.36}$$

Recall that it is considered adiabatic, inviscid flow, i.e., there are no dissipative mechanism such as friction, thermal conduction, or diffusion acting on the flow. Thus, the flow is isentropic. Hence, any change in pressure, dp, in the flow is accompanied by a corresponding isentropic change in density, $d\rho$. Therefore, it can be written

$$\frac{dp}{d\rho} = \left(\frac{\partial p}{\partial \rho}\right)_s = a^2 \tag{2.37}$$

Combining Eqs. (2.36) and (2.37),

$$a^2 \frac{d\rho}{\rho} = -udu$$

or

$$\frac{d\rho}{\rho} = -u\frac{du}{a^2} = -\frac{u^2}{a^2}\frac{du}{u} = -M^2\frac{du}{u} \tag{2.38}$$

Substituting Eq. (2.38) into Eq. (2.35),

$$\boxed{\frac{dA}{A} = (M^2 - 1)\frac{du}{u}} \tag{2.39}$$
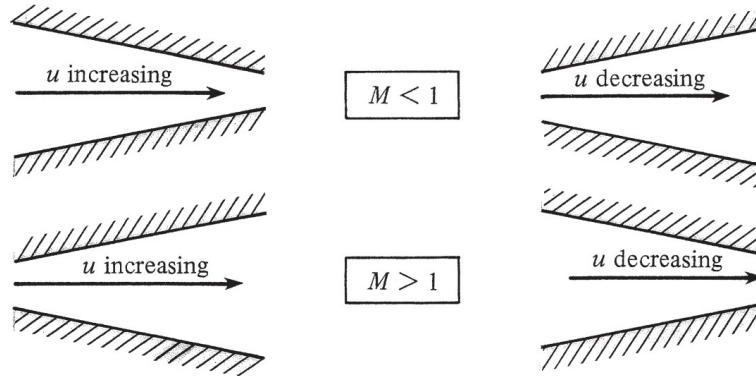
Figure 2.6: Flow in converging and diverging ducts[22].

Equation (2.39) represents a fundamental result known as the *area–velocity relation*, which provides key insights into compressible flow behavior:

1. **Incompressible Flow ($M \to 0$):** In the limiting case of incompressible flow, Equation (2.39) simplifies to $Au = $ const, which corresponds to the classical continuity equation for incompressible fluids.

2. **Subsonic Flow ($0 < M < 1$):** In this regime, an increase in velocity ($du > 0$) corresponds to a decrease in cross-sectional area ($dA < 0$), and vice versa. Consequently, the behavior observed in incompressible flow remains valid: velocity increases in a converging duct and decreases in a diverging duct. This trend is illustrated in the upper part of Figure 2.6.

3. **Supersonic Flow ($M > 1$):** Unlike subsonic flow, an increase in velocity is now associated with an increase in cross-sectional area, and vice versa. This leads to a fundamental distinction: for supersonic flow, velocity increases in a diverging duct and decreases in a converging duct, as depicted in the lower part of Figure 2.6.

4. **Sonic Flow ($M = 1$):** At Mach 1, Equation (2.39) yields $dA/A = 0$, mathematically indicating a minimum or maximum in the area distribution but the physically meaningful solution corresponds to a minimum in the cross-sectional area.

These findings clearly demonstrate that for a gas to undergo isentropic expansion from subsonic to supersonic speeds, it must pass through a convergent–divergent duct

(or streamtube), as illustrated in the upper part of Figure 2.7. Furthermore, at the minimum area dividing the convergent and divergent sections, the flow must reach Mach 1, as indicated in item 4. This critical point is referred to as the throat of the duct.

Conversely, for a gas to undergo isentropic compression from supersonic to subsonic speeds, it must also pass through a convergent–divergent duct. The throat, where the flow becomes sonic, similarly serves as the transition point between the supersonic and subsonic regimes, as shown in the lower part of Figure 2.7.
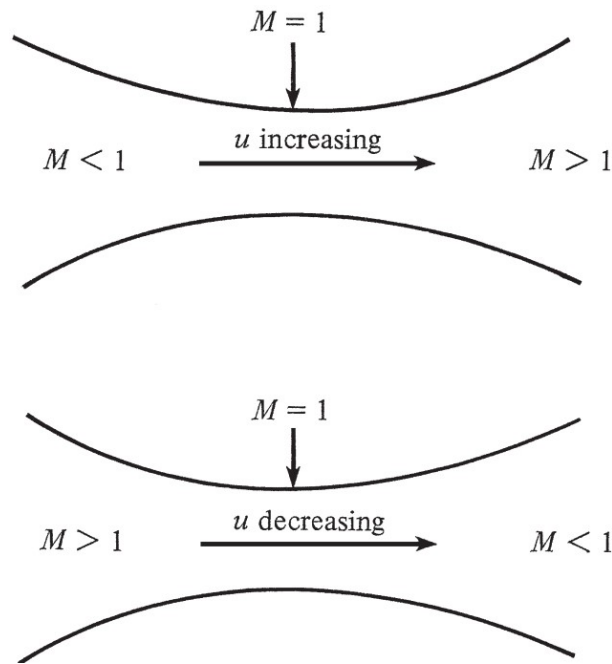
Figure 2.7: Flow in a convergent-divergent duct[22].

2.4 Shock waves

In this section, it will be examined the fundamental characteristics of shock waves, which are thin regions in a fluid where rapid changes in flow properties occur due to compressibility effects. Given their extremely small thickness, shock waves are often idealized as surfaces of discontinuity across which pressure, velocity, density, and temperature undergo abrupt variations. These waves propagate at supersonic speeds and introduce irreversible effects, such as an increase in entropy. The discussion will cover the governing equations, physical behavior, and practical implications of shock waves in high-speed flows, providing a foundation for their role in aerodynamics, propulsion systems, and other applications in compressible fluid dynamics.

2.4.1 Normal Shock relations

$$p_1 \qquad p_2 > p_1$$
$$T_1 \qquad T_2 > T_1$$
$$\rho_1 \qquad \rho_2 > \rho_1$$
$$u_1 \qquad u_2 < u_1$$
$$M_1 > 1 \qquad M_2 < 1 \qquad x \text{ direction}$$

① ②

Given conditions ahead of the shock wave

Unknown conditions behind the shock wave
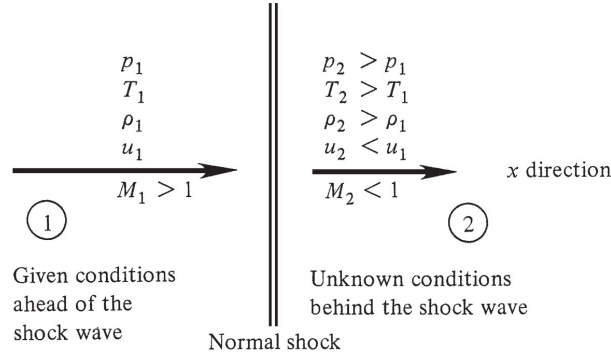
Normal shock

Figure 2.8: Diagram of a normal shock[22].

In this section, the fundamental principles of compressible flow are applied to the specific case of a normal shock wave, with the objective of analyzing the physical mechanisms responsible for variations in flow properties within a one-dimensional, constant-area flow. Normal shocks are commonly encountered in supersonic flowfields and play a crucial role in high-speed aerodynamics. By definition, a normal shock wave is a thin, nearly discontinuous region that is oriented perpendicular to the incoming flow, as depicted in Fig. 2.8. The shock thickness is typically on the order of a few molecular mean free paths, approximately 10^{-5}cm for air under standard atmospheric conditions. Across this thin region, significant changes occur in flow properties: static pressure, temperature, and density increase, while velocity decreases, transitioning the flow from supersonic to subsonic conditions.

$M_\infty < 1$
$V_\infty < a_\infty$

(a) Subsonic flow

$M_\infty > 1$
$V_\infty > a_\infty$
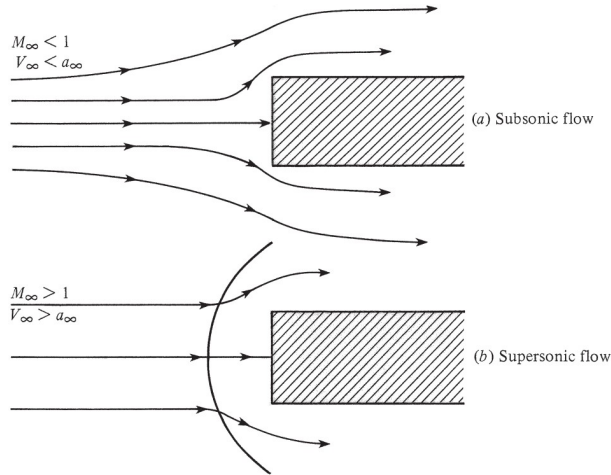
(b) Supersonic flow

Figure 2.9: Comparison between subsonic and supersonic streamlines for flow over a flat-faced cylinder or slab [22].

Shock waves naturally arise in supersonic flows as a response to the fundamental problem of how disturbances propagate within fluid. To gain an intuitive understanding

of this phenomenon, a flat-faced cylinder placed in a high-speed flow is considered , as illustrated in Fig. 2.9. Since the flow consists of individual molecules, those that collide with the cylinder undergo a change in energy and momentum, which is subsequently transmitted to the surrounding molecules. In subsonic conditions ($V_\infty < a_\infty$), these disturbances propagate upstream via sound waves, allowing the flow to gradually adjust to the presence of the obstacle, as seen in Fig. 2.9a. However, in supersonic conditions ($V_\infty > a_\infty$), disturbances cannot propagate upstream. Instead, they accumulate in a narrow region ahead of the obstacle, forming a shock wave, as shown in Fig. 2.9b.

Ahead of the shock wave, the flow has no idea of the presence of the body. However, immediately after passing through the shock, the flow slows to subsonic speeds, allowing the streamlines to quickly adapt to the body's presence. While the scenario depicted in Fig. 2.9b represents one particular case, the fundamental mechanism behind shock wave formation applies to many high-speed flow situations.

To begin a quantitative analysis of the changes occurring across a normal shock wave, reference is made to Figure 2.8, in which the shock is modeled as a discontinuity across which flow properties undergo abrupt variations. For the purpose of this analysis, it is assumed that all flow conditions upstream of the shock (region 1) are known, with the objective of determining the corresponding downstream conditions (region 2). Since no heat is added to or removed from the flow as it passes through the shock, the process is adiabatic. Consequently, the fundamental equations governing normal shocks are directly derived from Eqs. (2.3), (2.7), and (2.10), with the heat transfer term set to zero ($q = 0$).

$$\rho_1 u_1 = \rho_2 u_2 \qquad \text{(continuity)}$$

$$p_1 + \rho_1 u_1^2 = p_2 + \rho_2 u_2^2 \qquad \text{(momentum)}$$

$$h_1 + \frac{u_1^2}{2} = h_2 + \frac{u_2^2}{2} \qquad \text{(energy)}$$

By combining the continuity and momentum equations with the definition of the speed of sound in an adiabatic flow, the Prandtl relation is obtained, a useful intermediate relation for normal shock:

$$a^{*2} = u_1 u_2 \tag{2.40}$$

or

$$M_2^{*2} = \frac{1}{M_1^{*2}} \tag{2.41}$$

where the starred (*) notation denotes flow properties at the critical condition, where the Mach number is exactly 1. These properties correspond to the state a fluid element would reach if it were isentropically accelerated or decelerated to sonic conditions. The critical condition of the Mach number can be expressed as

$$M^{*2} = \frac{(\gamma + 1)M^2}{2 + (\gamma - 1)M^2} \tag{2.42}$$

Based on the preceding physical considerations, the flow upstream of a normal shock wave must be supersonic, i.e., $M_1 > 1$, which implies $M_1^* > 1$. Consequently, according to Equation (2.41), it follows that $M_2^* < 1$, and therefore $M_2 < 1$, confirming that the

downstream flow is subsonic. Hence, the Mach number behind the normal shock is always subsonic. This is a general result, not just limited to a calorically perfect gas.

Substituting Eq. (2.42) into (2.41) and solving for M_2^2 it can be obtained:

$$M_2^2 = \frac{1 + \frac{\gamma-1}{2}M_1^2}{\gamma M_1^2 - \frac{\gamma-1}{2}} \tag{2.43}$$

Equation (2.43) demonstrates that, for a calorically perfect gas with a constant ratio of specific heats γ, the downstream Mach M_2 number is a function of only the upstream Mach number M_1 . It should be noted that, when $M_1 = 1$, the downstream Mach number remains $M_2 = 1$, corresponding to an infinitely weak normal shock, also known as a Mach wave. In contrast, as M_1 becomes larger than unity, the shock strength rises, and M_2 decreases progressively below 1. In the limiting case where $M_1 \to \infty$, M_2 approaches a finite minimum value, given by $M_2 = \sqrt{\frac{\gamma-1}{2\gamma}}$, which for air is approximately 0.378.

The upstream Mach number M_1 plays a fundamental role in determining shock wave characteristics, as evident from Equation (2.43). Additionally, the ratios of other thermodynamic properties across the shock can also be expressed as functions of M_1, further emphasizing its significance in shock wave analysis. The expression of density, pressure and temperature as a function of the upstream Mach number M_1 are respectively

$$\frac{\rho_2}{\rho_1} = \frac{u_1}{u_2} = \frac{(\gamma+1)M_1^2}{2+(\gamma-1)M_1^2} \tag{2.44}$$

$$\frac{p_2}{p_1} = 1 + \frac{2\gamma}{\gamma+1}\left(M_1^2 - 1\right) \tag{2.45}$$

$$\frac{T_2}{T_1} = \frac{h_2}{h_1} = \left[1 + \frac{2\gamma}{\gamma+1}\left(M_1^2 - 1\right)\right]\left[\frac{2+(\gamma-1)M_1^2}{(\gamma+1)M_1^2}\right] \tag{2.46}$$

Taking a look on Eqs. (2.43), (2.44), (2.45) and (2.46), for a calorically perfect gas with a given γ, all this thermodynamic properties across the shock are functions of M_1 only, further emphasize the importance of Mach number in the quantitative governance of compressible flowfields.

The result presented in this section are reasonable accurately up to approximately $M_1 = 5$ in air standard conditions. At higher Mach numbers, the temperature behind the normal shock becomes high enough that γ is no longer constant.

Earlier in this section, it was established that the flow upstream of a normal shock wave must be supersonic, as previously discussed in the context of shock wave formation. While this has been easily observed from physical principles, it is noteworthy that Equations (2.43), (2.44), (2.45) and (2.46) are mathematically valid for both $M_1 < 1$ and $M_1 > 1$. However, to demonstrate that these equations are physically meaningful only when $M_1 > 1$, it is necessary to invoke the second law of thermodynamics, which governs the irreversibility and entropy changes of shock waves

$$s_2 - s_1 = c_p \ln\frac{T_2}{T_1} - R\ln\frac{p_2}{p_1} \tag{2.47}$$

with Eqs. (2.45) and (2.45), the second law of thermodynamics can be expressed

$$
\begin{aligned}
s_2 - s_1 = c_p \ln &\left\{ \left[1 + \frac{2\gamma}{\gamma + 1}(M_1^2 - 1) \right] \left[\frac{2 + (\gamma - 1)M_1^2}{(\gamma + 1)M_1^2} \right] \right\} \\
&- R \ln \left[1 + \frac{2\gamma}{\gamma + 1}(M_1^2 - 1) \right]
\end{aligned}
\tag{2.48}
$$

Equation (2.48) establishes that the entropy change across a normal shock wave depends only on the upstream Mach number M_1. Specifically, the equation indicates that if $M_1 = 1$, then $s_2 - s_1 = 0$, if $M_1 < 1$, then $s_2 - s_1 < 0$ and if $M_1 > 1$ then $s_2 - s_1 > 0$. Since it is necessary that $s_2 - s_1 \geq 0$ from the second law, it follows that the upstream Mach number must be at least unity $M_1 \geq 1$.

This result once more shows how the second law determines the direction of physical processes. If M_1 is subsonic, Equation (2.48) would imply a decrease in entropy across the shock, which is physically impossible. Hence, the only feasible scenario is when $M_1 \geq 1$, which, in turn dictates from Equations (2.43), (2.44), (2.45) and (2.46) that $M_2 \leq 1$, $\frac{\rho_2}{\rho_1} \geq 1$, $\frac{p_2}{p_1} \geq 1$, and $\frac{T_2}{T_1} \geq 1$. These relationships confirm the fundamental behaviour illustrated in Figure 2.8, demonstrating that across a normal shock wave, pressure, density, and temperature increase, while velocity and Mach number decrease to subsonic values.
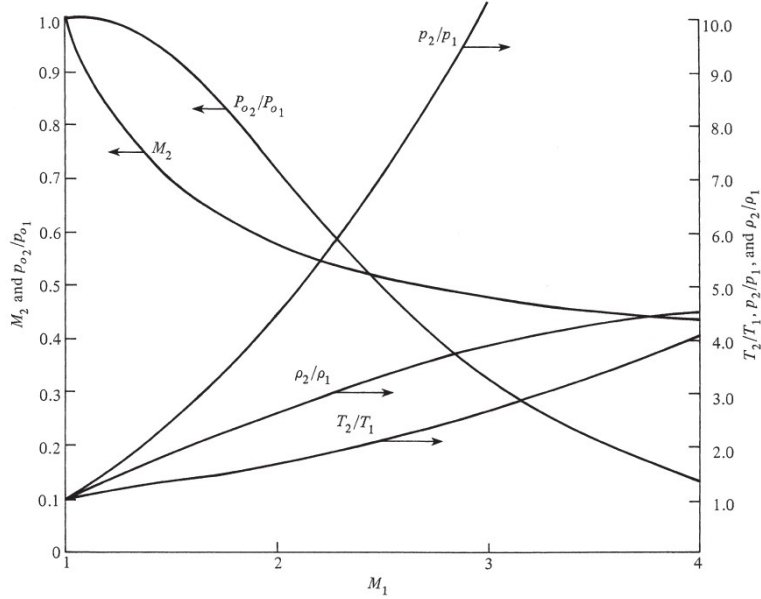
Figure 2.10: Properties behind a normal shock wave as a function of upstream Mach number [22].

Regarding the total conditions T_0 and p_0 ahead and behind the normal shock wave, from the Eq. (2.49)

$$
c_p T_1 + \frac{u_1^2}{2} = c_p T_2 + \frac{u_2^2}{2}
\tag{2.49}
$$

and from the definition of total temperature of Eq. (2.50)

$$c_p T + \frac{u_2}{2} = c_p T_0 \tag{2.50}$$

it yields

$$\boxed{T_{0_1} = T_{0_2}} \tag{2.51}$$

Hence, the total temperature remains constant across a stationary normal shock wave. In general, this result is a consequence of the conservation of total enthalpy across the shock, which holds for calorically and thermally perfect gases. Therefore, Eq. (2.47) becomes

$$\boxed{s_2 - s_1 = -R \ln \frac{p_{0_2}}{p_{0_1}}} \tag{2.52}$$

or

$$\frac{p_{0_2}}{p_{0_1}} = e^{-\frac{s_2 - s_1}{R}} \tag{2.53}$$

In conclusion, from Eqs. (2.48) and (2.53) the ratio of total pressure across the normal shock depends only on M_1. Given that $s_2 > s_1$, the total pressure decreases across the shock, consistent with the increase in entropy. Additionally, to enhance physical intuition, these variations are visually represented in Figure 2.10.

Through these results obtained for the normal shock wave, since the static pressure always increases across the shock, the wave itself can also be visualized as a thermodynamic compression mechanism. Furthermore, the changes across a normal shock wave can be expressed in terms of purely thermodynamic variables without explicit reference to a velocity or Mach number.

$$e_2 - e_1 = \frac{p_1 + p_2}{2} \left(\frac{1}{\rho_1} - \frac{1}{\rho_2} \right) \tag{2.54}$$

or

$$\boxed{e_2 - e_1 = \frac{p_1 + p_2}{2} \left(\nu_1 - \nu_2 \right)} \tag{2.55}$$

Equation (2.55) is called *Hugoniot equation*. It has certain advantages because it relates only thermodynamic quantities across the shock. Moreover, no assumptions have been made regarding the specific type of gas; Equation (2.55) remains a general relation applicable to perfect gases, chemically reacting gases, and real gases. Additionally, it is noteworthy that Equation (2.55) follows the form $\Delta e = p_{ave} \Delta \nu$, indicating that the change in internal energy is equal to the average pressure across the shock multiplied by the change in specific volume.
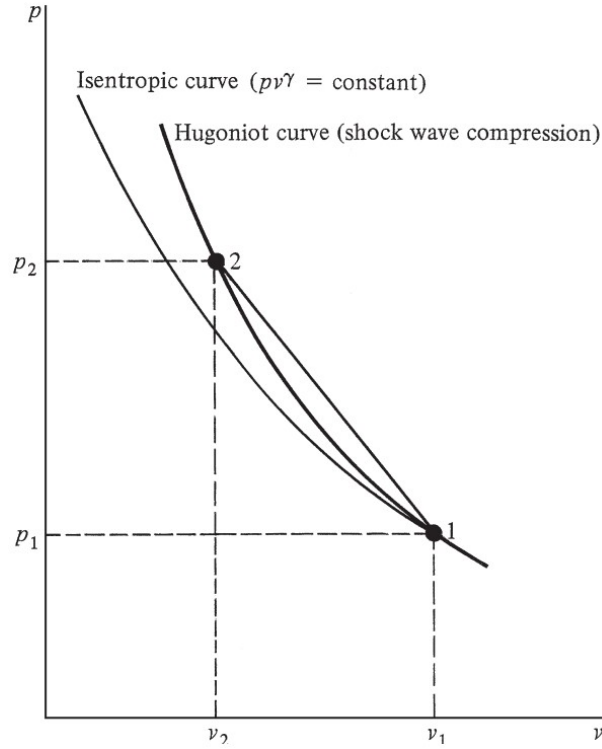
Figure 2.11: Comparison between Hugoniot curve and isentropic compression [22].

Shock wave compression is a highly effective process, however not necessarily efficient. To illustrate this, consider the comparison between the isentropic and Hugoniot curves originating from the same initial state (p_1, v_1), as depicted in Figure 2.11. At this point, both curves share the same slope, which can be demonstrated by noting that point 1 on the Hugoniot curve corresponds to an infinitely weak shock, or a Mach wave. However, as the specific volume decreases, the Hugoniot curve rises above the isentropic curve, indicating that for a given reduction in specific volume, a shock wave produces a greater pressure increase than an isentropic compression. This advantage, however, comes at the cost of increased entropy and a corresponding loss in total pressure, i.e., the shock compression is less efficient than the isentropic compression.

Eq. (2.55) can be also written as

$$\frac{p_2}{p_1} = \frac{\left(\frac{\gamma+1}{\gamma-1}\right)\frac{\nu_1}{\nu_2} - 1}{\left(\frac{\gamma+1}{\gamma-1}\right) - \frac{\nu_1}{\nu_2}} \tag{2.56}$$

33
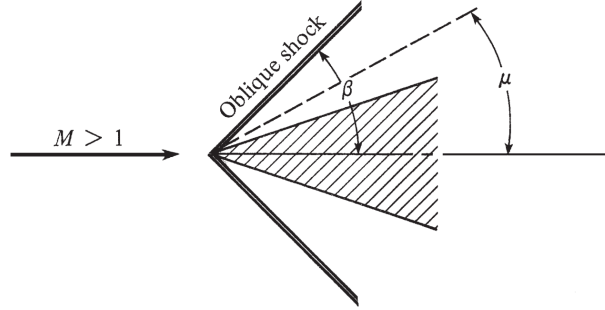
2.4.2 Oblique Shock

Figure 2.12: Oblique shock wave [22].

An oblique shock wave forms when a supersonic flow encounters a disturbance, such as a wedge or compression corner, causing a discontinuous change in flow properties at an angle to the free stream. Unlike normal shocks, where the flow is entirely decelerated to subsonic speeds, an oblique shock allows the flow to remain supersonic under certain conditions.
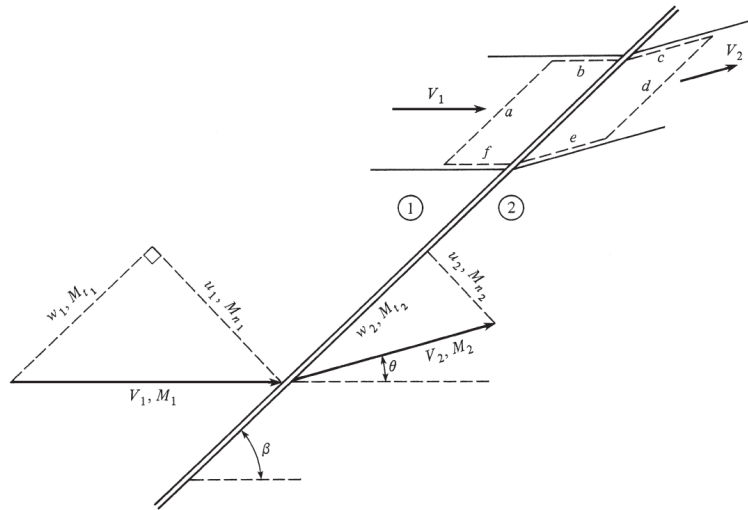
Figure 2.13: Oblique shock wave geometry [22].

The geometric representation of flow through an oblique shock wave is illustrated in Figure 2.13. Upstream of the shock, the flow velocity V_1 is horizontal, with a corresponding Mach number M_1. The oblique shock forms a wave angle β relative to V_1, and the flow is deflected by an angle θ in the direction of the shock. Downstream of the shock, the velocity and Mach number are denoted as V_2 and M_2, respectively. The velocity components perpendicular and parallel to the shock wave are given by u_1 and w_1 for the upstream flow and u_2 and w_2 for the downstream flow. Consequently, the normal and tangential Mach numbers across the shock are represented as M_{n_1}, M_{t_1} upstream and M_{n_2}, M_{t_2} downstream.

The integral forms of the conservation equations were previously applied in Section 2.1 to a one-dimensional flow control volume, leading to the normal shock relations presented in Section 2.4.1. A similar approach is adopted for oblique shocks. A control volume bounded by two streamlines across an oblique shock is considered, as indicated by the dashed lines in Figure 2.13. Faces *a* and *d* are parallel to the shock wave. Applying the integral form of the continuity equation to this control volume under steady-state conditions yields:

$$\rho_1 u_1 = \rho_2 u_2 \tag{2.57}$$

where $A_1 = A_2$ represent the areas of faces *a* and *d*. The control volume faces *b, c, e,* and *f* are aligned with the velocity vector, thus their contributions to the surface integral vanish ($V \cdot dS = 0$).

The integral form of the momentum equation is a vector equation. By resolving it into components parallel and perpendicular to the shock, and considering steady flow without body forces, the tangential momentum equation simplifies to:

$$(-\rho_1 u_1)w_1 + (\rho_2 u_2)w_2 = 0 \tag{2.58}$$

Dividing by the continuity equation it yields:

$$w_1 = w_2$$

This result is significant, indicating that the tangential component of velocity remains unchanged across an oblique shock wave.

Applying the normal component of the momentum equation it can be obtained

$$(-\rho_1 u_1)u_1 + (\rho_2 u_2)u_2 = -(p_1 + p_2)$$

or

$$p_1 + \rho_1 u_1^2 = p_2 + \rho_2 u_2^2 \tag{2.59}$$

The integral form of the energy equation applied to the control volume in Figure 2.13 for a steady adiabatic flow with no body forces, it yields

$$\left(h_1 + \frac{V_1^2}{2}\right)\rho_1 u_1 = \left(h_2 + \frac{V_2^2}{2}\right)\rho_2 u_2 \tag{2.60}$$

Dividing Eq. (2.60) by (2.57) and recall from the geometry of Figure 2.13 that $V^2 = u^2 + w^2$ and $w_1 = w_2$

$$V_1^2 - V_2^2 = \left(u_1^2 + w_1^2\right) - \left(u_2^2 + w_2^2\right) = u_1^2 - u_2^2$$

Eq. (2.60) becomes

$$h_1 + \frac{u_1^2}{2} = h_2 + \frac{u_2^2}{2} \tag{2.61}$$

Careful examination of Equations (2.57), (2.59), and (2.61) reveals that they have the same mathematical form as the normal shock continuity, momentum, and energy equations. In both cases, the velocity components normal to the wave determine the flow

35

properties across the shock. Consequently, the variations across an oblique shock wave are dictated by the normal component of the upstream velocity. Moreover, applying the same algebraic manipulations used for the normal shock equations in Section 2.4.1 to Equations (2.57), (2.59), and (2.61) results in identical expressions describing the changes across an oblique shock, expressed in terms of the normal component of the upstream Mach number. That is, for an oblique shock wave with

$$M_{n_1} = M_1 \sin \beta \tag{2.62}$$

For a calorically perfect gas,

$$M_{n_2}^2 = \frac{M_{n_1}^2 + \frac{2}{\gamma - 1}}{\left[\frac{2\gamma}{(\gamma - 1)}\right] M_{n_1}^2 - 1} \tag{2.63}$$

Note that the Mach number behind the oblique shock, M_2, can be found from M_{n_2} and the geometry of Figure 2.13 as

$$M_2 = \frac{M_{n_2}}{\sin (\beta - \theta)} \tag{2.64}$$

In Sec. 2.4.1 it was emphasized that changes across a normal shock were a function of only the upstream Mach number. Now the changes across an oblique shock are function of two quantities, both M_1 and β. It can also be noted that normal shock are just a special case of oblique shocks where $\beta = \pi/2$.

Equation (2.64) demonstrates that M_2 cannot be found until the flow deflection angle θ is obtained. However, θ is also a unique function of M_1 and β, as follows, from the geometry of Figure 2.13

$$\tan \beta = \frac{u_1}{w_1} \tag{2.65}$$

and

$$\tan(\beta - \theta) = \frac{u_2}{w_2} \tag{2.66}$$

Combining Eqs. (2.65) and (2.66) together, and noting that $w_1 = w_2$

$$\frac{\tan(\beta - \theta)}{\tan \beta} = \frac{u_2}{u_1} \tag{2.67}$$

Combining Eq. (2.67) with Eqs. (2.57) and (2.62) and with some trigonometric manipulation, it can be obtained

$$\tan \theta = 2 \cot \beta \left[\frac{M_1^2 \sin^2 \beta - 1}{M_1^2(\gamma + \cos 2\beta) + 2} \right] \tag{2.68}$$

Equation (2.68) is called the $\theta - \beta - M$ *relation*, and specifies θ as a unique function of M_1 and β.
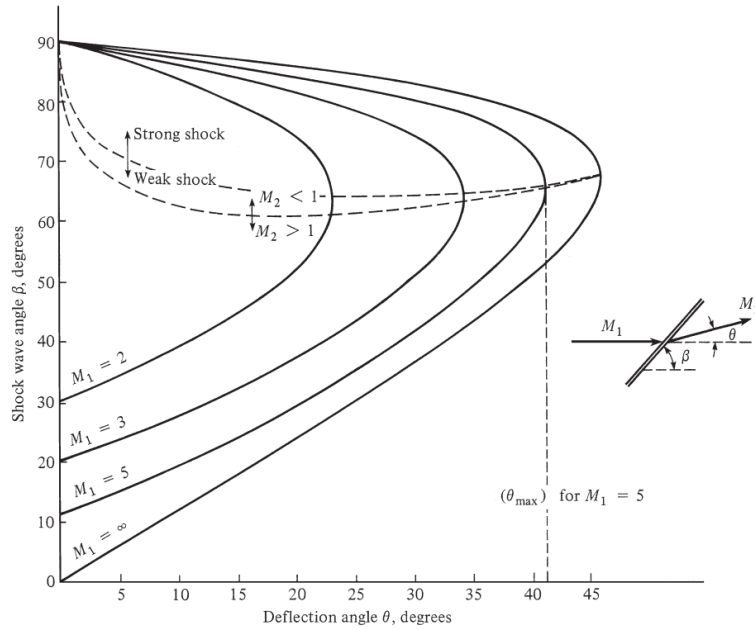
Figure 2.14: θ-β-M curves. Oblique shock properties [22].

The relationship between the wave angle β, deflection angle θ, and Mach number M_1 is fundamental in the analysis of oblique shocks. The results derived from this relation are plotted in Figure 2.14 for $\gamma = 1.4$. This figure presents a graphical representation of the wave angle β versus deflection angle θ, with the Mach number M_1 as a parameter. Several key observations can be made:

1. **Existence of a Maximum Deflection Angle**: For a given upstream Mach number M_1, there exists a maximum deflection angle $\theta_{\max}$. If the physical geometry requires a deflection angle greater than this limit $\theta > \theta_{\max}$, then no solution exists for a straight oblique shock wave . Instead, the shock becomes curved and detached, as illustrated in Figure 2.15, which compares wedge and corner flows for cases where θ is below or above $\theta_{\max}$.

2. **Weak and Strong Shock Solutions**: When the deflection angle is below the maximum limit $\theta < \theta_{\max}$, the θ-β-M relation predicts two possible wave angles β for a given Mach number. These correspond to the weak shock and strong shock solutions, as depicted in Figure 2.16. The strong shock solution corresponds to the larger β, resulting in more severe changes in flow properties, whereas the weak shock solution is associated with the smaller β. In most practical scenarios, the weak shock solution is favored and typically observed in nature. However, the occurrence of the strong shock solution depends on downstream pressure conditions. If the downstream pressure increases due to an external mechanism, the strong shock (dashed line in Figure 2.16) can be forced to occur. In the strong shock case, the downstream Mach number M_2 is subsonic, whereas in the weak shock case, M_2 remains supersonic, except for conditions near $\theta_{\max}$ (see Figure 2.14).

37

3. **Special Cases**: if $\theta = 0$, then $\beta = \frac{\pi}{2}$ corresponding to a normal shock, or $\beta = \mu$, corresponding to a Mach wave.

4. **Effect of Mach Number on Wave Angle**: For a fixed deflection angle θ, decreasing the upstream Mach number leads to an increase in the wave angle (for the weak shock solution). As the Mach number decreases to a critical value, the wave angle reaches its maximum ($\theta = \theta_{\max}$), beyond which no oblique shock solutions exist. For Mach numbers below this limit, the shock wave detaches, as illustrated in Figure 2.15.

This analysis highlights the critical role of the upstream Mach number in determining shock behavior, providing insight into when attached oblique shocks, detached shocks, or strong/weak solutions occur.
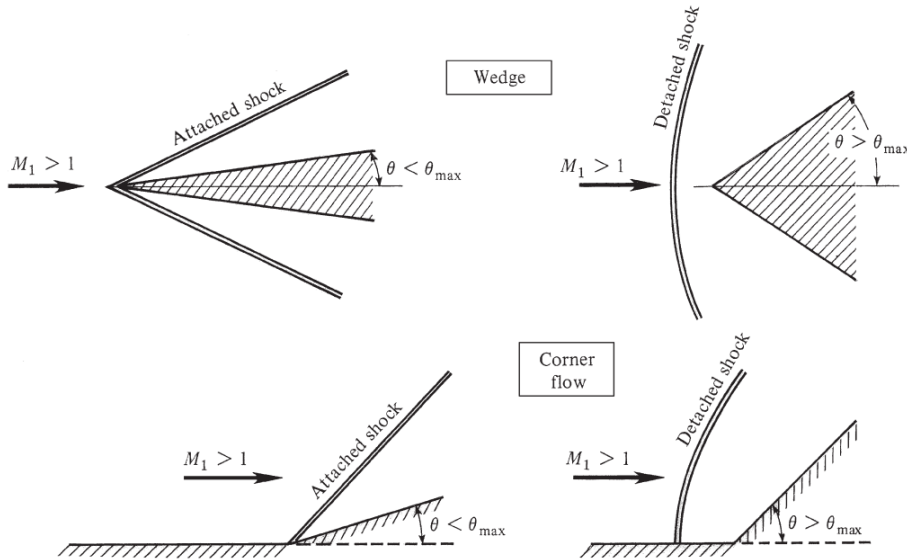
Figure 2.15: Attached and detached shocks [22].
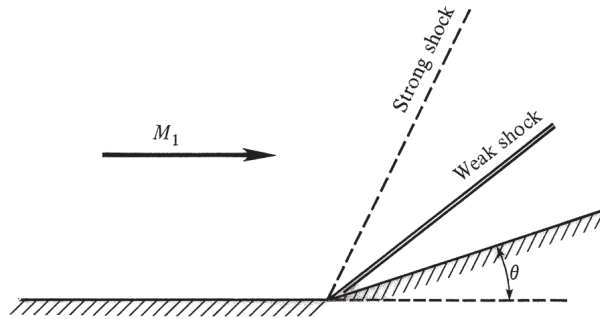
Figure 2.16: Weak and strong shocks [22].

38
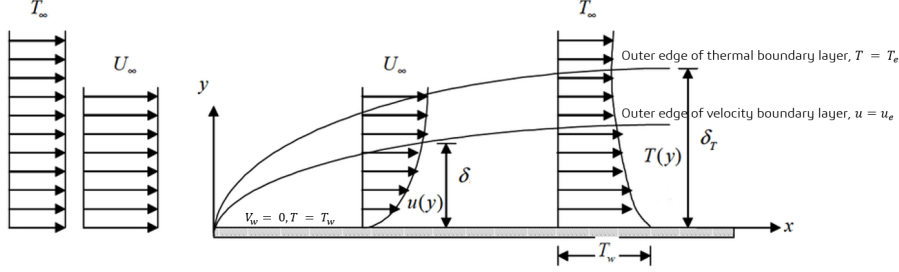
2.5   Boundary Layer

Figure 2.17: Boundary Layer properties [24].

The boundary layer is a thin region of fluid flow adjacent to a solid surface, where the effects of viscous friction cause a progressive reduction in velocity from the freestream value to zero at the wall, a condition known as the *no-slip condition*. Similarly, the fluid temperature at the wall equals the surface temperature T_w, as shown in Fig. 2.17.

Above the surface, the velocity increases with the normal coordinate y until it effectively reaches the freestream velocity V_∞. The distance from the surface where the velocity attains 99% of the freestream value is defined as the velocity boundary-layer thickness δ. In Fig. 2.17, which illustrates the flow over a flat plate, the velocity at the outer edge of the boundary layer is given by $u_e = V_\infty$. For bodies with arbitrary shapes, u_e corresponds to the inviscid velocity at the body surface.

At a given streamwise location x, the velocity distribution within the boundary layer, denoted as $u(y)$, is referred to as the velocity profile. Similarly, the thermal boundary layer develops due to temperature variations in the normal direction. The thermal boundary-layer thickness δ_T is defined as the distance at which the temperature reaches 99% of the external temperature T_e. The variation of temperature within this layer, denoted as $T(y)$, is referred to as the temperature profile.

The presence of a velocity gradient at the wall generates a shear stress, which is given by:

$$\tau_w = \mu \left(\frac{du}{dy} \right)_{y=0} \tag{2.69}$$

where μ is the dynamic viscosity and $\left(\frac{du}{dy} \right)_{y=0}$ is the velocity gradient evaluated at the wall. A fundamental boundary-layer property is the *displacement thickness* (δ^*), defined as:

$$\delta^* \equiv \int_0^{y_e} \left(1 - \frac{\rho u}{\rho_e U_e} \right) dy \tag{2.70}$$

This quantity has two significant physical interpretations:

1. The displacement thickness represents the reduction in mass flow caused by the presence of the boundary layer. It quantifies the extent to which the boundary layer displaces the inviscid flow, effectively reducing the available flow passage.

2. In practical applications, the displacement thickness modifies the effective shape of a body interacting with the freestream. While the physical body geometry is defined by its physical shape, the presence of the boundary layer alters the perceived shape. The freestream flow behaves as if it were interacting with an enlarged body, where the displacement thickness is added to the original geometry.

2.6   Shock Wave-Boundary-Layer Interactions (SWBLI)

Shock wave–boundary layer interactions (SBLIs) significantly influence the performance of aerodynamic surfaces and propulsion systems, occurring on both external and internal surfaces. These interactions introduce complex flow structures, where the boundary layer encounters an adverse pressure gradient imposed by the shock, while the shock propagates through a multilayered viscous-inviscid flow.

In turbulent flows, SBLIs enhance turbulence production, increasing viscous dissipation, which leads to higher drag on wings and reduced engine efficiency due to performance losses in turbine blades and increased internal flow losses. The distortion of the boundary layer velocity profile due to the adverse pressure gradient amplifies the displacement thickness, affecting the surrounding inviscid flow. In extreme cases, a strong shock can induce boundary layer separation, causing significant flowfield modifications, formation of vortices and complex shock patterns, and large-scale unsteadiness such as intake buzz, or nozzle side loads, all of which can degrade vehicle performance or induce structural damage.

Shock-induced separation is essentially a compressible counterpart of classical flow separation, sharing similar boundary-layer behavior but with additional shock patterns in the outer inviscid flow, which can drastically alter the global flow structure. SBLIs occur across a wide range of Mach numbers, from transonic to hypersonic flows, where their impact becomes particularly severe due to the intensity of the shocks.

a – oblique shock reflection   b – ramp induced shock wave

c – normal shock wave   d – adaptation shock at a nozzle exit
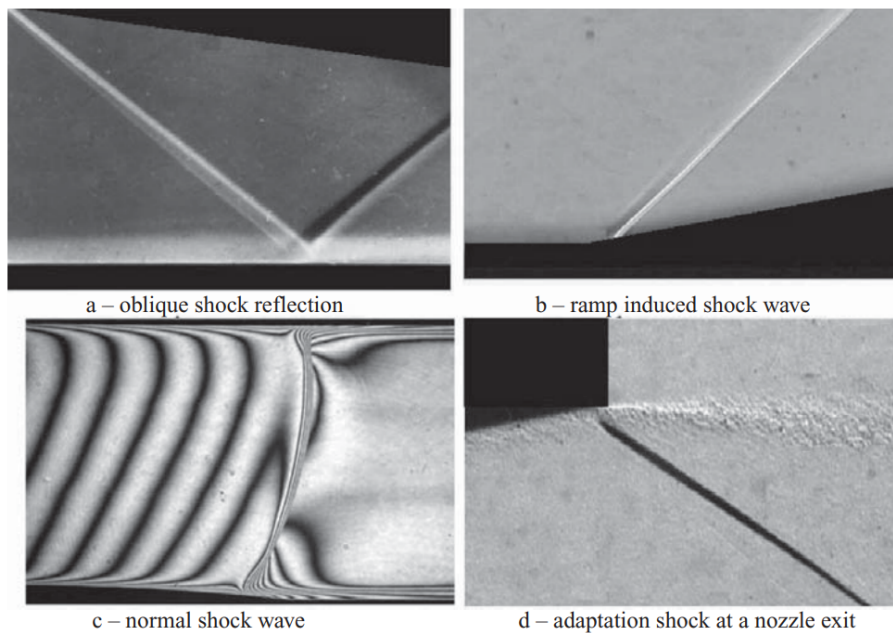
Figure 2.18: Basic SBLIs [23].

In two-dimensional supersonic flows, shock wave–boundary layer interactions (SBLIs) can be classified into four fundamental types:

1. **Oblique-Shock Reflection**: When an oblique shock impinges on a flat surface (Fig. 2.18a), the supersonic upstream flow (M_1) is deflected by an angle $\Delta\varphi_1$ across the incident shock. To maintain a parallel downstream flow, a reflected shock forms, causing a deflection $\Delta\varphi_2 = -\Delta\varphi_1$. This type of interaction commonly occurs inside mixed-compression supersonic air intakes or when shocks generated by obstacles interact with nearby surfaces.

2. **Ramp-Induced Shock**: A ramp flow occurs when a sudden change in wall inclination generates a shock wave (Fig. 2.18b). The flow is deflected by an angle $\Delta\varphi_1$, which corresponds to the wedge angle β. Such shocks are observed in supersonic air-intake compression ramps, control surfaces, or sharp changes in surface direction.

3. **Normal Shock**: A normal shock can develop when a supersonic flow undergoes a back-pressure increase that forces a transition to subsonic flow. This occurs in channel flows with a two-throat system, where a normal shock forms due to downstream choking, necessitating a stagnation pressure drop to satisfy mass conservation. Unlike oblique shocks, a normal shock decelerates the flow without changing the velocity direction, resulting in a subsonic Mach number behind the shock. However, in most practical applications, the shock is not perfectly normal (i.e., the interferogram in Fig. 2.18c) but rather a strong oblique shock, even in weak transonic cases. Such shocks are found in turbomachinery cascades, air intakes, supersonic diffusers, shock tubes, and transonic profiles, where they terminate a supersonic pocket. When the downstream flow is subsonic, disturbances can propagate upstream, leading to unsteady phenomena such as air-intake buzz.

4. **Oblique Shock Induced by a Pressure Jump**: If a supersonic flow encounters a pressure discontinuity (e.g., at the exit of an overexpanded nozzle), an oblique shock forms (Fig. 2.18d). In this scenario, the pressure jump induces the flow deflection, unlike in the first two cases, where the flow deflection caused the pressure jump. This represents a mirror case of the deflection–pressure jump duality.

From a macro prospective shock wave–boundary layer interactions (SBLIs) can be classified as weak or strong, with strong interactions capable of inducing boundary layer separation near the impingement point. In the following paragraphs only the two most common interactions will be discussed: shock impingement on a flat-plate boundary layer and compression ramp interaction.

2.6.1 Weak interactions
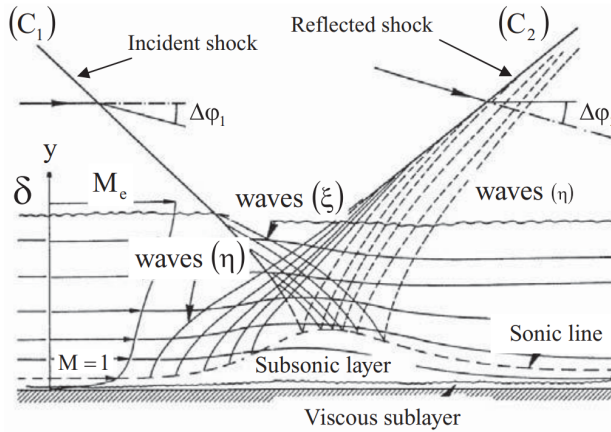
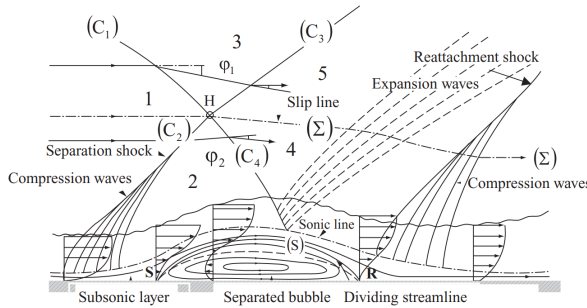**Figure 2.19:** A sketch of a turbulent shock reflection without boundary-layer separation [23].
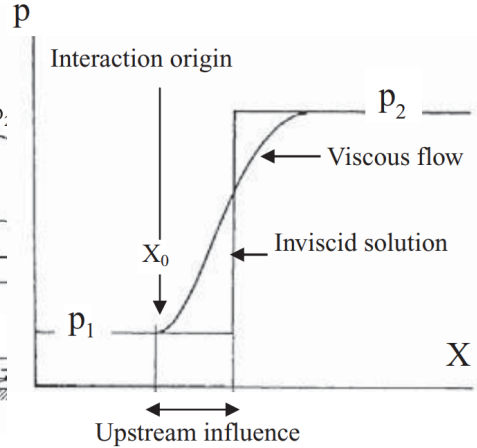
Figure 2.20: Pressure distribution in a weak SBLIs [23].

The interaction between an oblique shock wave and a turbulent boundary layer is sketched in Figure 2.19. A similar structure appears in a laminar boundary layer, though the interaction region extends further downstream. As the incident shock (C_1) penetrates the inviscid portion of the boundary layer, it bends due to the local Mach number decrease, weakening until it vanishes at the sonic line. The pressure rise across the incident shock (C_1) is felt upstream of its expected impingement point in the absence of a boundary layer through the subsonic part of the boundary layer. Consequently, the wall-pressure distribution spreads over a length scale comparable to the boundary-layer thickness, deviating from the prediction of a purely inviscid solution. As illustrated in Figure 2.20, the pressure begins to increase upstream of the inviscid pressure jump, progressively rising until it matches the downstream inviscid level. This weak interaction process results in a pressure distribution that deviates only slightly from the inviscid solution, making viscous effects a secondary correction. Such behaviour is said to be a *weak interaction* process in the sense that the flow is weakly affected by viscous effects. The expansion of the subsonic layer affects the outer supersonic flow, generating compression waves (η) that merge to form the reflected shock (C_2). A boundary layer with a fuller velocity profile has a thinner subsonic region, leading to shorter upstream influence.
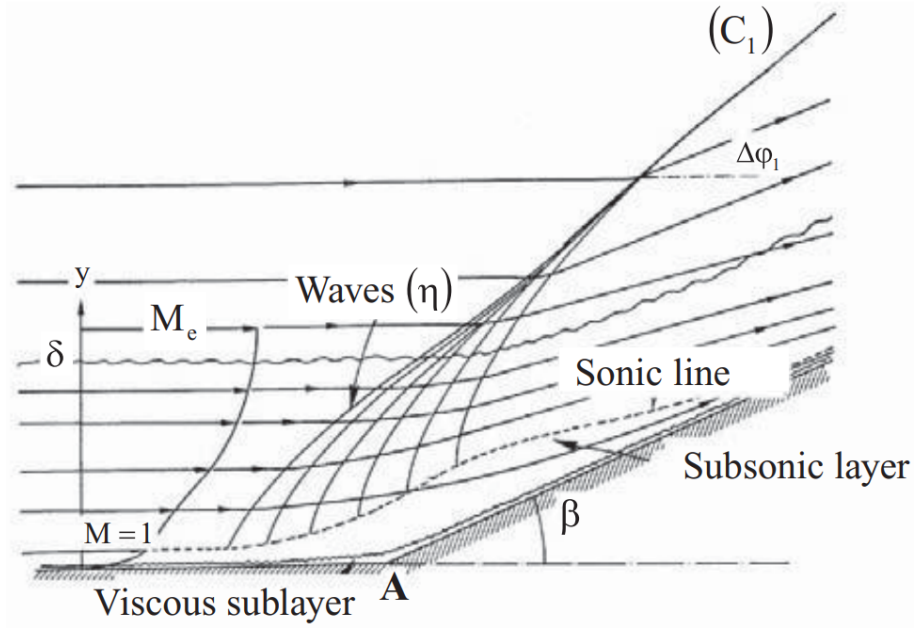
Figure 2.21: Ramp-induced shock without boundary-layer separation [23].

A similar mechanism occurs in ramp-induced interactions (Figure 2.21), where the pressure rise from shock (C_1) propagates upstream through the subsonic boundary layer, inducing compression waves (η) in the supersonic region. These waves coalesce into (C_1), which increases in intensity with distance from the surface until reaching the inviscid solution. However, at high Mach numbers, the subsonic channel has a minor effect on the overall interaction structure, and most of the physics can be interpreted in terms of an inviscid process, as in the incident-shock induced interaction.

2.6.2 Strong interactions

Figure 2.22: A sketch of a turbulent shock reflection with boundary-layer separation [23].
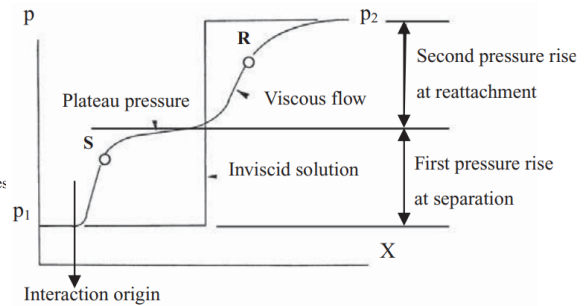
Figure 2.23: Wall pressure distribution in a shock-separated flow [23].

The boundary layer is characterized by a decrease in stagnation pressure towards the wall, while remaining nearly constant along streamlines over short distances. Neglecting compressibility, the Bernoulli equation relates pressure increases to flow retardation, which is most pronounced in the inner boundary layer where p_{st} is lowest. Under an adverse pressure gradient, flow near the wall can stagnate or reverse, leading to separation. This flow structure is sketched in Fig. 2.22. Downstream of the separation point (S), a recirculating bubble forms, enclosed by a dividing streamline (S) that separates the reversed flow from the main stream. This streamline originates at (S) and ends at the reattachment point (R). Intense mixing in the detached shear layer transfers mechanical energy from the high-speed outer flow to the separated region, causing the velocity U_s along the dividing streamline to increase until it slows down near reattachment. The transmitted shock (C_4) enters the separated viscous flow and is reflected as an expansion wave due to the nearly constant pressure inside the separation bubble. This reflection deflects the shear layer back toward the wall, leading to reattachment at point R, where the bubble disappears, and the flow along (S) slows down until it stagnates. This process generates compression waves, which merge to form a reattachment shock in the outer flow. As shown in Figure 2.23, the wall pressure distribution initially shows a sharp increase at the separation point, followed by a plateau pressure, characteristic of separated flows. A second, more progressive pressure rise occurs during reattachment. In this situation, the flowfield structure is markedly different from what it would be for the purely inviscid case, and the shock reflection is said to be a *strong viscous-inviscid interaction*.
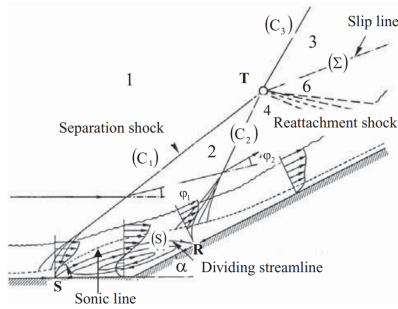
Figure 2.24: Ramp-induced shock with boundary-layer separation [23].
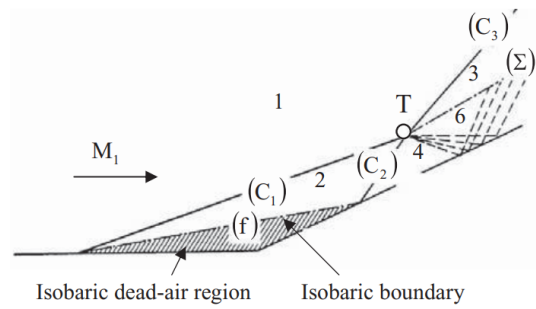
Figure 2.25: Wall pressure distribution in a shock-separated flow [23].

The case of ramp-induced separation is shown in Figure 2.24. When the flow deflection caused by the ramp generates a shock wave stronger than the boundary layer can sustain, separation occurs at point S, located upstream of the ramp apex. Similar to shock reflection, a separation shock (C_1) forms due to the convergence of compression waves generated by the separation process. Downstream of S, the near-wall fluid in the boundary layer recirculates, forming a separation bubble similar to previous cases. The flow reattaches at point R, producing a reattachment shock (C_2), which is less inclined than the separation shock due to the change in flow direction and the lower Mach number downstream of (C_2). The equivalent inviscid representation of this case is shown in Fig. 2.25. A simpler two-shock system forms with a separation shock emanating from the inviscid separation point and a reattachment shock from the inviscid reattachment

point. If the Mach number is high enough, the two converging shocks intersect at a small distance from the wall.

Chapter 3

Implementation of theory

The conventional methodology for intake design starts with the implementation of a simplified compressive flow model, which combines a sequence of isentropic flow regions and oblique shocks. The resulting geometry is then evaluated for its ability to start, and if the flow does not start, the design must be revised. An effective air intake design takes into account the following factors:

- The intake must efficiently meet the specified requirements for contraction, compression, and Mach number reduction.

- It should reliably start and maintain steady operation throughout the vehicle's flight envelope, with starting occurring below the cruise Mach number.

- Performance degradation due to off-design Mach numbers or changes in the angle of attack should be minimized.

- The flow direction at the intake exit should align with the freestream to prevent losses in the combustion chamber and the nozzle.

- Overboard mass flow spillage should be minimized and, if unavoidable, restricted to the intake starting phase.

At the downstream end of the intake, critical design challenges typically arise. This is where the starting process ends, shocks interact with the boundary layer, and conditions for the combustor are established.

3.1 Busemann flow

One of the most optimal geometries for a combustor, capable of withstand extreme heat and pressure loads, is the circular cross section. This shape minimizes the ratio of surface area to volume, effectively reducing friction losses to the lowest possible level. Consequently, the study of asymmetric flow has been conducted extensively. Such geometries, inspired by Busemann's research on streamtube designs, are referred to as Busemann flow and Busemann intakes.
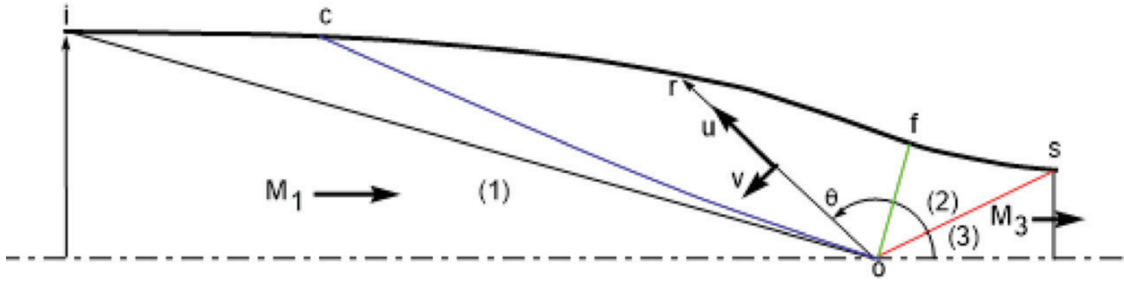
Figure 3.1: Visualization of Busemann Flow Dynamics [11].

Fig. 3.1 presents a schematic representation of Busemann flow. In region (1), the uniform freestream flow undergoes isentropic compression from the freestream Mach cone up to the conical shock cone (2). Upon passing through the conical shock, the flow transitions into a uniform, parallel flow in region (3). The flow remains axially and conically symmetric, as well as irrotational throughout. The isentropic contraction and compression between regions (1) and (2) are followed by a loss of total pressure across the shock, occurring between regions (2) and (3). The green line marks a cone that contains the inflection points of all Busemann streamlines. This inflection point cone plays a critical role in initiating supersonic flow within the intake.

3.2   Axisymmetric Compression Flow Field

The compression flow field is a fundamental aspect of the intake design process. The basic Busemann intake surface is axisymmetric and features a converging duct aligned with the freestream along its axis of symmetry. At the leading edge, a conical Mach wave of zero strength forms, as the geometry does not induce any flow deflection. Downstream, the flow begins turning towards the axis, resulting in a reduction in flow area, compression of the flow, and an increase in pressure along the surface.

The inflection point mentioned above represents the location of the minimum turning angle of the flow. Beyond this point, the flow begins to turn away from the axis, passing through a conical shock, where it is deflected to become uniform and parallel to the axis at the intake exit. In particular, the flow within a Busemann intake exhibits both axial and conical symmetry. This symmetry establishes a focal point along the axis from which rays can be drawn in any direction. Along each of these rays, the flow conditions remain constant.

3.2.1   Taylor-Maccoll Equations

To better understand intake flows, it is often advantageous to reduce the number of physical dimensions considered, simplifying the analysis by focusing on fewer variables. This reduction is justified when the flow properties remain constant with respect to the eliminated dimension, which occurs when the flow exhibits some form of symmetry. For example, planar flow in the (x, y) system is derived by eliminating the z-variable from

the Cartesian (x, y, z) system. Similarly, in a spherical coordinate system (r, θ, ϕ), axial flow in the (r, θ) system can be achieved by removing the circumferential angle ϕ.

If the flow properties are also invariant in the radial direction r for an axial flow, the flow becomes strictly one-dimensional with respect to the angular variable θ. This leads to the derivation of the Taylor-Maccoll equations, which describe flows that exhibit conical symmetry. Conical flows, governed by the Taylor-Maccoll equations, include supersonic flow over an axisymmetric cone at $0°$ angle of attack, as well as Busemann flow and axisymmetric conical flows.

The Taylor-Maccoll equation itself is a nonlinear, second-order total differential equation, where the radial velocity U is the dependent variable and the spherical polar angle θ is the independent variable [11].

$$\frac{\gamma - 1}{2} \left[1 - U^2 - \left(\frac{dU}{d\theta}\right)^2 \right] \left[2U + \frac{dU}{d\theta} \cot\theta + \frac{d^2U}{d\theta^2} \right] - \frac{dU}{d\theta} \left[U\frac{dU}{d\theta} + \frac{dU}{d\theta}\frac{d^2U}{d\theta^2} \right] = 0 \quad (3.1)$$

and the streamline equation is

$$\frac{dr}{d\theta} = r\frac{U}{V} \tag{3.2}$$

The governing equation for steady, axisymmetric, and conical flow of a perfect gas has not yet yielded an explicit algebraic solution. Furthermore, no numerical schemes exist for directly solving the second-order form presented earlier. However, the equation can be reformulated into two first-order equations (3.3) and (3.4), by introducing an additional dependent variable, V. This reformulation allows the use of standard numerical methods to solve the system efficiently.

The first-order formulations of Eq. (3.2) correspond to the momentum equations in polar coordinates, applied in the r and θ directions:

$$\frac{dV}{d\theta} = -U + \frac{a^2(U + V\cot\theta)}{V^2 - a^2} \tag{3.3}$$

$$\frac{dU}{d\theta} = V \tag{3.4}$$

where a is the speed of sound, and it can be written in terms of total conditions and velocities through the energy equations. The second of these equations is the irrotationality condition, which implies that conical flows are necessarily irrotational flows.

3.3 Starting of the intake
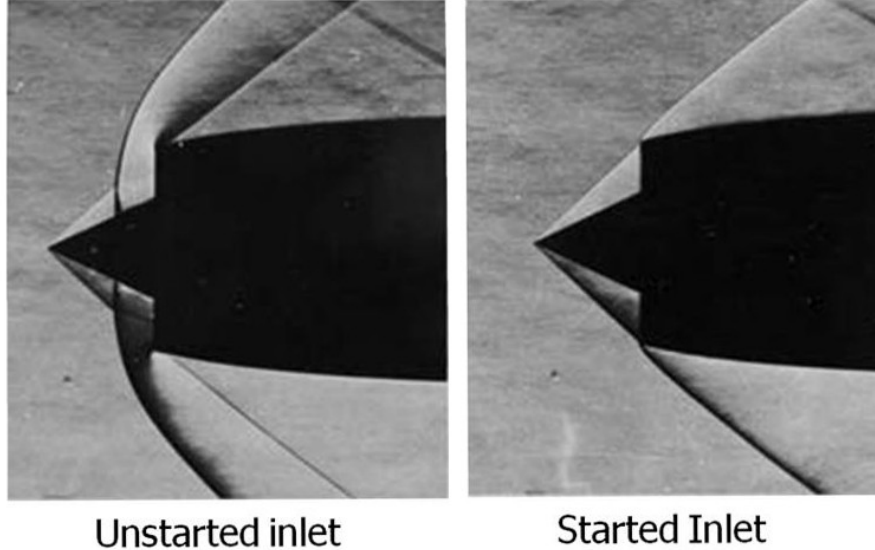
Figure 3.2: Started and Unstarted condition [25].

A Busemann intake, or more generally any converging duct in supersonic flow, can support two distinct flow configurations for the same freestream Mach number. The first configuration features a bow shock positioned ahead of the intake, which diverts part of the flow externally, and the resulting internal flow becomes subsonic. This indicates that the flow is unstarted. In contrast, the second configuration is characterized by the absence of a bow shock and overboad spillage, allowing the flow to remain supersonic throughout the intake. Started flow is essential for proper engine operation. Ensuring that the flow is started is critical for engine efficiency, as unstarted flow leads to significant total pressure losses and reduced mass flow, which is essential for thrust [4]. In order to initiate and maintain a stable supersonic flow, it is necessary to displace the normal shock in front of the intake downstream, thus allowing the converging section of the intake to establish supersonic conditions. This requirement imposes key constraints on the intake design. Although an inviscid design may rely on simplified flow assumptions, the actual starting flow is often three-dimensional. The shock wave and boundary layer interaction (SWBLI) must be considered, since it plays a crucial role in the intake starting process, particularly when strong shocks are present. Shock swallowing and intake flow starting are intrinsically unsteady processes. However, if the shock wave propagates much slower than the surrounding flow, the flow can be approximated as quasi-steady, allowing the application of steady-state flow equations. Instead, if the shock moves rapidly, the intake is considered to be over-started. This implies that the intake is not operating at its maximum contraction potential, resulting in performance losses. The application of steady-state flow principles results in the Kantrowitz criterion [26], which defines the conditions for flow starting in a converging duct through shock swallowing. This criterion

states that if the exit remains unchoked the shock in front of the duct will be ingested, and supersonic flow will be established throughout the duct. This occurs when the ratio of the exit-to-entry area of the duct is greater than the **Kantrowitz criterion**:

$$\frac{A^{**}}{A_1} = \left(\frac{(\gamma + 1)M_1^2}{(\gamma - 1)M_1^2 + 2} \right)^{0.5} \left(\frac{(\gamma + 1)M_1^2}{2\gamma M_1^2 - (\gamma - 1)} \right)^{\frac{1}{\gamma - 1}} \tag{3.5}$$

Spontaneous starting occurs above this line; however, the resulting compression is insufficient. An intake that starts spontaneously must undergo further contraction in order to operate near the isentropic condition and achieve optimal performance. Obviously, the closer the intake approaches the isentropic limit, the more challenging the starting process becomes. The **isentropic limit** is defined by:

$$\frac{A^*}{A_1} = \frac{1}{M_1} \left[\frac{2}{\gamma + 1} \left(1 + \frac{\gamma - 1}{2} M_1^2 \right) \right]^{\frac{\gamma + 1}{2(\gamma - 1)}} \tag{3.6}$$
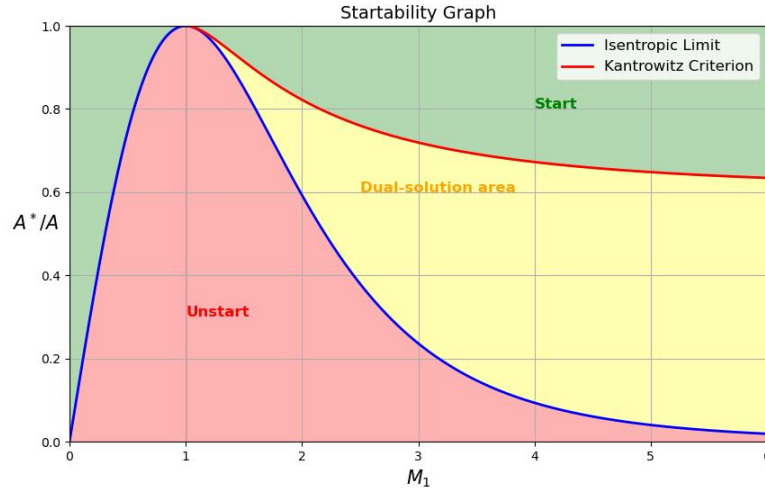
Figure 3.3: Kantrowitz criterion and isentropic limit.

The adiabatic contraction line represents the theoretically highest attainable compression, corresponding to a total pressure recovery of 100%. A duct with an exit-to-entry area ratio, denoted as A_e/A_1, that lies between these two limits will operate in a stable supersonic condition, if it has been started. A value of A_e/A_1 close to A^*/A_1 is an indication that the intake is difficult to start, whereas a value near A^{**}/A_1 suggests that the intake is more likely to start.

3.3.1 Startability Index

In order to quantify the difficulty of starting an intake, it is useful to introduce an index S_i. By considering the Kantrowitz and isentropic contraction ratios as the upper and

lower limits, respectively, this index provides a measure of the intake's position within that range.

$$S_i = \frac{\frac{A_e}{A^*} - 1}{\frac{A^{**}}{A^*} - 1} \tag{3.7}$$

Referred to as the **startability index**, it represents the ratio of contractions, based on the assumption that startability improves as contraction decreases. The index takes a value of 1 at the Kantrowitz condition, where the intake just starts spontaneously. Conversely, at a contraction corresponding to the isentropic area ratio, below which the intake can no longer remain started, it reaches a value of 0.

The startability index can be applied to the entire intake, as well as to specific internal sections, to evaluate their individual tendencies to start spontaneously.

3.4 Truncation effects

Truncation effects can be categorized into two types: leading-edge truncation effects and rear-side truncation effects. In general, the shape of a truncated intake deviates significantly from its original design [27]. As a result, the computed flow field variables differ from those of the non-truncated counterpart, indicating that the two flow fields are no longer similar.

3.4.1 Leading edge truncation
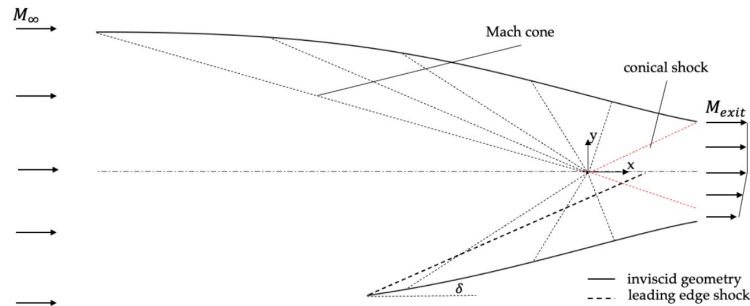
Figure 3.4: Leading edge truncation [28].

Busemann intakes exhibit excellent performance characteristics due to their isentropic compression but they tend to become excessively long, thus increasing skin friction drag and weight. A closer examination of the leading-edge surface of a Busemman intake reveals that it does not present deflection or curvature in the direction parallel to the axis of symmetry, meaning it does not contribute to the compression of the entering airflow. Consequently, the leading-edge surface's contribution in the overall compression process is negligible. Moreover, this surface sustains a boundary layer with high shear, leading to significant efficiency losses. In order to mitigate these losses, leading-edge truncation is often introduced as a means of improving efficiency. However, truncation induces a positive flow deflection at the leading edge, generating a shock. This results

in a deterioration of efficiency due to the total pressure loss in the inviscid flow. Thus, intake design requires a trade-off between boundary layer losses and shock-induced losses. Optimizing the amount of truncation is crucial to minimizing the sum of both losses. Studies in [29] [30] [31] have investigated truncation effects, showing that reducing the intake length by truncation angles between $2°$ and $6°$ are usually sufficient. At the truncated leading edge, an oblique shock forms, which interferes with the isolines of isentropic compression as it propagates downstream. This interaction leads to a reduction in compression efficiency, which worsens as the truncation angle increases. Additionally, truncation disrupts the homogeneity of the outflow, further affecting intake performance.

3.4.2 Rear side truncation
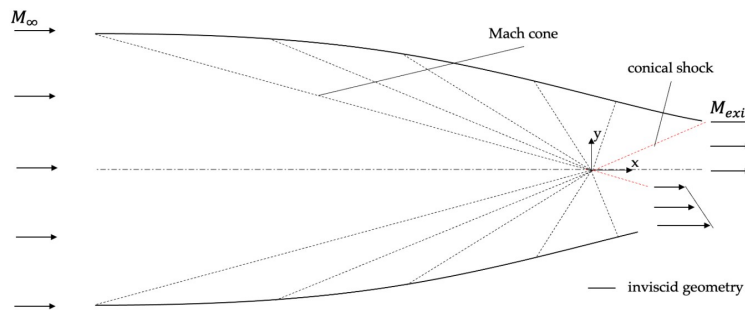
Figure 3.5: Rear side truncation [28].

Further reduction of the Busemann intake length can be achieved by truncating its rear side. A schematic representation of a truncated Busemann contour is shown in Fig. 3.5. While the impact on length reduction is less pronounced compared to leading-edge truncation, the rear side truncation introduces an oblique shock at higher Mach number, hence high shock losses. Therefore, it may be advantageous to limit the leading-edge truncation to a certain degree and achieve the desired length reduction by a combination of both. This modification shortens the structure of the isolines, and an expansion at the beginning of the isolator further disturbs the flow field. Consequently, the flow through the isolator is no longer homogeneous. In general, truncation reduces the overall compression compared to the original, non-truncated geometry. Although rear-side truncation complicates an analytical formulation of the flow field, it offers additional benefits. Specifically, it reduces the internal contraction ratio, defined as the ratio between the cowl closure cross-sectional area and the combustion chamber area. In general, a lower internal contraction ratio improves the intake's starting characteristics.

3.5 Viscous effects

Typically, at the leading edge of the intake a boundary layer naturally forms and evolves under the influence of the edge properties known from the inviscid flow field. However, due to the displacement effect of the boundary layer, the compression region is further contracted, altering its properties. This interaction affects the development of the

boundary layer, which in turn influences the core flow. The effect of this phenomenon is illustrated at the bottom of Fig. 3.6 for a classical Busemann flow field. In general, the effective contraction of the Busemann contour is known to increase due to the additional displacement caused by the boundary layer. As a result, both pressure and temperature are higher than the one predicted by the inviscid analytical models. Moreover, the flow through the isolator may become non-uniform due to disturbances in the flow field. This effect is strongly dependent on the Reynolds number, becoming more pronounced as the Reynolds number decreases. One approach to address this issue involves computing the displacement thickness of the viscous boundary layer. By incorporating the displacement thickness into the intake design, the contour can be adjusted accordingly, leading to a corrected geometry with lower internal and overall contraction ratio. The key objective is to protect the inviscid core flow from the additional contraction of the boundary layer, as schematically represented in Fig 3.7. Wie and Mölder [32] implemented this correction by utilizing the edge pressure distribution from analytical compression flow solutions as input for a boundary layer code to calculate the displacement thickness. Their numerical investigations on axisymmetric cases demonstrated that corrected geometries produced viscous simulations that closely matched analytical predictions. For a classical, non-truncated contour, they observed an initial expansion near the leading edge due to the widening of the flow, which further justified the truncation of the leading edge. Smart [33] utilized a finite difference boundary layer code to incorporate viscous effects under on-design conditions. In his methodology, the transition from laminar to turbulent flow was initiated at a predetermined location downstream of the leading edge within the boundary layer model. Similarly, Matthews and Jones [34] estimated viscous properties using a turbulent flat plate correlation combined with the reference temperature method for an axisymmetric spike intake. Their analytical predictions successfully captured intake performance, highlighting the necessity of considering isolator skin friction to ensure agreement between analytical and experimental data.
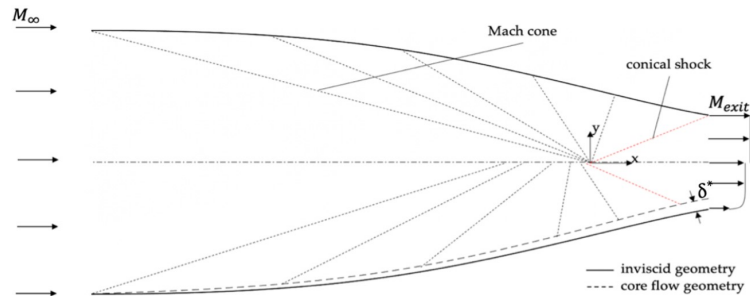
Figure 3.6: Schematic of classical Busemann flow (top), schematic of viscous effects in uncorrected Busemann contour (bottom) [28].
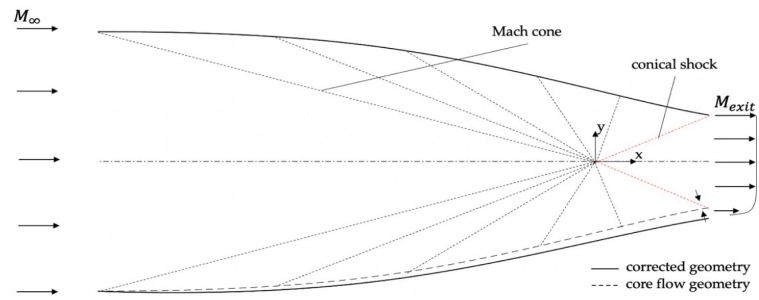
Figure 3.7: Schematic of classical Busemann flow (top), schematic of viscous effects in corrected Busemann contour (bottom) [28].

Chapter 4

Design strategy

4.1 Overview

The objective of this chapter is to present the methodology that has been utilised to effectively design and analytically predict the performance of a 2D Busemann intake, and the procedure necessary to obtain a 3D intake, starting from its 2D counterpart.

4.2 Modified Taylor-Maccoll equations

Starting from the Taylor-Maccoll equations introduced in the previous chapter:

$$\frac{dV}{d\vartheta} = -U + \frac{a^2(U + V\cot\vartheta)}{V^2 - a^2} \tag{4.1}$$

$$\frac{dU}{d\vartheta} = V \tag{4.2}$$

And the streamline equation:

$$\frac{dr}{d\vartheta} = \frac{rU}{V} \tag{4.3}$$

Instead of using velocity components as dependent variables, the equations are reformulated to express the radial and angular Mach number components as dependent variables. This transformation eliminates the need for explicit reference to the speed of sound and total conditions. By adopting this approach, boundary conditions—defined in terms of Mach number components at the upstream and downstream sides of conical shocks—can be directly applied to the solution of the equations. Additionally, since the total conditions do not influence the Mach number distribution, they do not need to be explicitly considered. Thus, the Taylor-Maccoll equations have been rewritten in terms of the radial and angular Mach numbers, denoted as u and v, where $u = \frac{U}{a}$ and $v = \frac{V}{a}$, with a is the local speed of sound.

$$\frac{du}{d\vartheta} = v + \frac{\gamma - 1}{2} uv \frac{u + v\cot\vartheta}{v^2 - 1} \tag{4.4}$$

$$\frac{dv}{d\vartheta} = -u + \left(1 + \frac{\gamma - 1}{2}v^2\right)\frac{u + v\cot\vartheta}{v^2 - 1} \tag{4.5}$$

Equations 4.4 and 4.5 provide valuable physical interpretations when expressed in terms of the Mach number components u and v. It is important to note that these equations no longer explicitly include the speed of sound or any total conditions. The streamline equation becomes:

$$\frac{dr}{d\theta} = \frac{ru}{v} \tag{4.6}$$

The flow Mach number is:

$$M = \sqrt{u^2 + v^2} \tag{4.7}$$

The singularity in this form of the Taylor-Maccoll equations arises when $v = \pm 1$, where the term $(v^2 - 1)$ in the denominators becomes zero. This singularity occurs when the angular Mach number component reaches the sonic condition, corresponding to the co-incidence of a radial and a Mach wave [7]. By formulating the equations without explicit reference to total conditions or the speed of sound, the application of boundary conditions becomes more straightforward and computationally efficient.

4.3 Boundary conditions

The computation of Busemann flow and the corresponding streamline geometry is derived from the Taylor-Maccoll equations (4.4) and (4.5). These equations are numerically integrated with respect to the radial coordinate r, progressing from the front of the conical shock toward the freestream. For the integration process, appropriate boundary conditions must be specified, u_2, v_2, and θ_2. As previously discussed, a fundamental requirement for the flow entering the combustor is that it remains both parallel to the freestream and uniform. Consequently, the values of u_2, v_2, and θ_2 must be carefully selected to satisfy these conditions, ensuring a consistent solution. Given the freestream Mach number in front of the shock, denoted as M_2, and the corresponding aerodynamic shock angle θ_{23}, the radial and angular Mach number components upstream of the shock can be expressed as:

$$u_2 = M_2\cos\theta_{23} \tag{4.8}$$

$$v_2 = -M_2\sin\theta_{23} \tag{4.9}$$

From the equation that relates the Mach number, shock angle, and flow deflection across the shock, the amount of flow deflection can be obtained as:

$$\cot\delta_{23} = \tan\vartheta_{23}\left[(\gamma + 1)\frac{M_2^2}{2(M_2^2\sin^2\vartheta_{23} - 1)} - 1\right] \tag{4.10}$$

The angular location of the shock, which is the starting value for the variable of integrations, is:

$$\theta_2 = \theta_{23} - \delta_{23} \tag{4.11}$$

Equations (4.4) (4.5) are then numerically integrated from θ_2 to θ_1. Since, the value of θ_1 is not known a priori, the integration proceeds until the vertical (or cross-stream) Mach

number, given by $(u \sin \theta + v \cos \theta)$ becomes zero, indicating that the freestream has been reached.

For the numerical integration of the Taylor-Maccoll equations, a MATLAB function was utilized, specifically ode89, which employs the 8th-9th order Runge-Kutta method. Although this approach is more computationally expensive, it ensures a highly precise contour, which is crucial for our design. Even minor errors can significantly impact the internal flow characteristics, making high accuracy essential.

4.4   Design steps
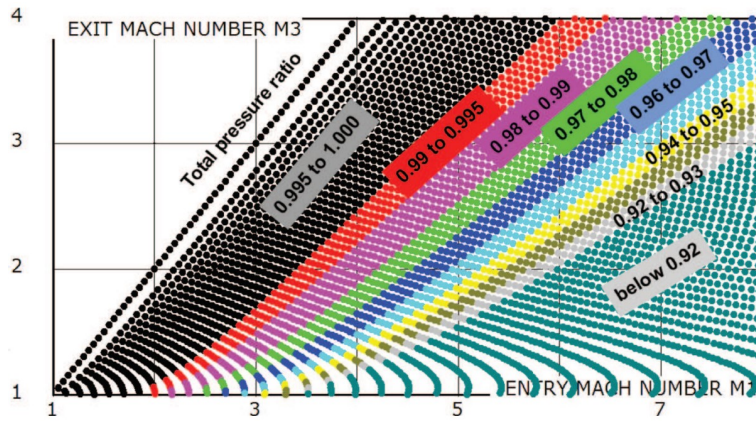
Figure 4.1: Inviscid performance of Busemann Intake [11].

It is possible to calculate the intake's efficiency before the integration, using the total pressure ratio as:

$$\frac{p_{t_3}}{p_{t_2}} = \left[\frac{(\gamma + 1)k^2}{(\gamma - 1)k^2 + 2} \right]^{\frac{\gamma}{\gamma - 1}} \left[\frac{\gamma + 1}{2\gamma k^2 - (\gamma - 1)} \right]^{\frac{1}{\gamma - 1}} \tag{4.12}$$

And the exit Mach number:

$$M_3^2 = \frac{(\gamma + 1)^2 M_2^2 k^2 - 4(k^2 - 1)(\gamma k^2 + 1)}{[2\gamma k^2 - (\gamma - 1)] [(\gamma - 1)k^2 + 2]} \tag{4.13}$$

Where $k^2 = M_2^2 \sin^2 \theta_{23}$. By setting a target efficiency, the value of k can be determined using Eq. (4.12). Subsequently, by specifying the downstream Mach number M_3, the parameter M_2 can be computed by inverting Eq. (4.13). Then one obtains:

$$\vartheta_{23} = \sin^{-1} \frac{k}{M_2} \tag{4.14}$$

$$u_2 = M_2 \cos \vartheta_{23} \tag{4.15}$$

$$v_2 = -M_2 \sin \vartheta_{23} \tag{4.16}$$

Following this, θ_{23} and δ_{23} are found using the same approach as before, and the integration is performed until $(u + v \cot \theta) \geq 0$. It is important to note that, since the integration starts from k and M_2, it may not yield the exact desired freestream Mach number, and an iterative adjustment of the input condition $\frac{p_{t_3}}{p_{t_2}}$ is required to achieve the target freestream Mach number.
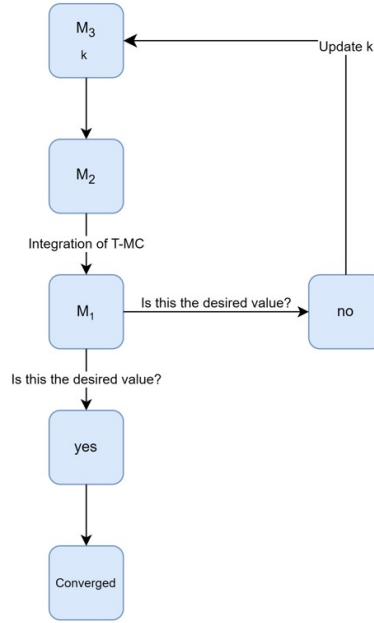
Figure 4.2: Iteration for achieving the target freestream Mach number value.

4.5   Inflection point

To demonstrate that the Taylor-Maccoll streamline can exhibit points of zero and infinite curvature, it is essential to derive an equation describing its curvature. The Busemann streamline contains two points where curvature is zero, one of which plays a crucial role in the starting of a Busemann-type intake. To determine the flow properties at the inflection cone, it is necessary to consider the fundamental equation governing the Taylor-Maccoll streamline:

$$\frac{dr}{d\theta} = \frac{ru}{v} \tag{4.17}$$

Taking another θ-derivative of eq. (4.17) gives:

$$\frac{d^2 r}{d\vartheta^2} = -r \frac{u}{v^2} \frac{dv}{d\vartheta} + \frac{r}{v} \frac{du}{d\vartheta} + \frac{ru^2}{v^2} \tag{4.18}$$

60

In polar coordinates the curvature of a planar curve is [35]:

$$D = \left(\frac{\partial \delta}{\partial s} \right) = \frac{r^2 + 2\left(\frac{dr}{d\vartheta} \right)^2 - r \frac{d^2 r}{d\vartheta^2}}{(r^2 + \left(\frac{dr}{d\vartheta} \right)^2)^{3/2}} \tag{4.19}$$

Eliminating the derivatives of r with (4.17) and (4.18) gives:

$$D = \frac{r^2 + 2(\frac{ru}{v})^2 + r^2 \frac{u}{v^2} \frac{dv}{d\vartheta} - \frac{r^2 du}{v d\vartheta} - (\frac{ru}{v})^2}{(r^2 + r^2 u^2/v^2)^{3/2}} \tag{4.20}$$

In this expression the derivatives $dv/d\theta$ and $du/d\theta$ are given by the Taylor-Maccoll Eqs. (4.1) and (4.2) thus the curvature can be written as:

$$D = \frac{uv(u + v \cot \vartheta)}{r(v^2 - 1)(v^2 + u^2)^{3/2}} \tag{4.21}$$

The curvature of the Taylor-Maccoll streamline is derived in terms of polar coordinates (r, θ) and the radial and angular Mach number components (u, v), based on the above equation. Analysing Eq. (4.21) reveals several significant characteristics regarding the curvature of the T-M streamline:

- The parameter D is inversely proportional to r, meaning that as $r \to 0$, $D \to \infty$. This implies that streamlines near the origin of T-M flows exhibit high curvature. This high curvature is a necessary condition for flow over a cone, as the flow deflection induced by the conical shock alone is insufficient to align the flow tangentially to the cone surface. As a result, the flow near the tip, just downstream of the conical shock, must rapidly adjust to the inclination imposed by the cone. It is important to note that, in terms of gradients of dependent variables (such as streamline curvature), conical flow is not fully conically symmetric (i.e., independent of r) because curvature varies inversely proportional to r. This dependence extends to other flow property gradients as well.

- When $v = 0$, the Taylor-Maccoll (T-M) streamlines exhibit an asymptotic behaviour where $D = 0$. In the case of flow over a cone, the velocity component v is zero at the cone surface, confirming that the streamlines asymptotically approach the cone surface. However, a Busemann flow does not exhibit an asymptotic condition where $v = 0$ or $u = 0$.

- When $u = 0$, the curvature D also becomes zero, indicating the presence of an inflection point along the streamline, where the radial Mach number vanishes. In flow over a cone, the condition $u = 0$ does not occur, meaning the streamlines remain consistently curved in a monotonically positive manner. However, in Busemann flow, there exists a specific location, denoted as θ_0, where the streamline curvature transitions from concave (toward the axis) to convex. The numerical integration of the Taylor-Maccoll equations has shown that this transition point θ_0 always falls within the interval θ_2 to $\theta/2$, slightly upstream of the Busemann shock. Each

Busemann streamline contains an inflection point and these points form a conical surface. At this angular position, the flow is everywhere normal to the inflected flow cone surface, allowing a conical normal shock to form at this location since the flow remains supersonic. The flow immediately downstream of the conical normal shock is inclined toward the axis. The intake would start spontaneously if the contraction downstream of the conical normal shock surface does not lead to choking, because then the shock would move downstream.. This feature has not been appreciated for Busemann flow [36]. The phenomenon serves as a conical and axisymmetric realization of the Kantrowitz criterion for one-dimensional flow starting. It follows the same principle: flow choking downstream of a normal shock, except in this case, the normal shock adopts a conical shape. The presence of a normal shock at the inflection point, combined with a choked exit, aligns with the Kantrowitz criterion for flow starting in the internal contraction downstream of the inflection [11].

- An inflection point also occurs when $(u + v \cot \theta) = 0$. This term represents the Mach number component normal to the flow axis, which becomes zero exclusively in Busemann flow, precisely where it joins the freestream. Consequently, the leading edge of Busemann flow exhibits both zero deflection and zero curvature. As previously discussed, this implies that the leading-edge wave is neither compressive nor expansive but instead behaves as a simple Mach wave. Since the incoming freestream flow experiences no deflection or curvature at the Busemann leading edge, a hypersonic air intake based on Busemann flow is inherently ineffective in generating compression at its leading edge.

- The case where $v \to \pm 1$ then $D \to \infty$ is not of interest when dealing with Busemann flow because it does not exhibit such a limit line.

- In the denominator of eq. (4.21), the quantity $(v^2 + u^2)^{3/2}$ is just M^3. It is always a positive quantity for all flow conditions and does not significantly influence D, apart from causing streamlines to gradually lose their curvature at hypersonic speeds.

The inflection point was identified as a key characteristic of the Busemann flow. Furthermore, it is of significant importance in the context of intake starting, as the ray extending from the origin to the surface is perpendicular to the surface at this point. Additionally, a conical normal shock may form at the inflection point.

4.6 Leading edge truncation

In the case of a classical Busemann intake, both weight and friction drag are higher, which, in a comprehensive analysis, may decrease the advantages of isentropic compression compared to a truncated intake. As a result, Busemann intakes are typically truncated. In the present study, truncation of the leading edge has been considered as an independent design parameter. The gradual deflection from the streamwise direction, necessary at the leading edge to achieve isentropic compression, presents a critical constraint for two main reasons:

- The overall geometry becomes excessively long.

- The sharpness of the leading edge or the minimum wall thickness is constrained by manufacturing limitations.

The angle between the free-stream velocity vector and the local velocity vector is called the truncation angle, δ. In a classical, fully enclosed Busemann intake, the Taylor-Maccoll equations must be numerically integrated until the total velocity matches the free-stream velocity, i.e., $\delta = 0$. For a truncated configuration, however, the integration is carried out until δ reaches the specified truncation angle. Truncation angles in the range of approximately $\delta = 2°$ to $\delta = 5°$ are sufficiently large to accommodate manufacturing constraints while significantly reducing the intake length. As a result of truncation, the leading edge is no longer parallel to the freestream, creating a sharp corner that generates an oblique shock propagating downstream toward the centerline. However, this oblique shock alters the isentropic compression characteristic of the classical Busemann flow. Additionally, the bow shock wave undergoes reflection from the symmetry line at a location beyond the theoretical focal point of the classical Busemann intake. As the bow shock approaches the symmetry axis, its slope becomes progressively steeper, ultimately forming a standing normal shock wave near the symmetry axis [37]. Notably, for typical truncation angles investigated ($\delta \leq 6°$), the radial extent of this normal shock remains minimal. The subsequent reflection of the shock from the symmetry line then propagates through the inlet-throat plane, below the inlet shoulder of the ideal Busemann intake. The introduction of additional non-ideal effects, such as leading-edge blunting and viscosity, induces a shift in the bow shock location in the opposite direction to that caused by truncation. These effects lead to the upstream displacement of the bow shock within the inlet. The influence of viscosity further contributes to this upstream shift by increasing the inlet contraction due to displacement thickness. Moreover, the computed static pressure ratio at the intake exit, and consequently the static temperature ratio, does not necessarily align with the intended design values. In a numerical study conducted by Zhao and Song [31], the impact of truncation in inviscid flow was analyzed for truncation angles of up to $\delta = 6°$. Their findings indicated that a stronger oblique shock is generated at the leading edge, increasingly distorting the flow field as the truncation angle grows. Additionally, intake efficiency was observed to decrease with increasing truncation angles. The Busemann intake truncation consists of neglecting the initial part of the geometry, that contracts, even if moderately, the flow; thus, the resulting truncated geometry won't match the desidered exit pressure, resulting in a flow field having a lower pressure ratio between the inlet and the outlet. Iteration over the initial values that define the geometry is made in order to circumvent this inconvenient. This translates into considering the initial input data:

- Free stream Mach number

- Exit Mach number

- Truncation angle

Is considered a first guess of efficiency value and, from eqs. (4.12) and (4.13) we obtain the initial values of u_2, v_2 and θ_2. The integration can now proceed until the angle between

the total velocity and the freestream reaches the specified truncation angle δ. The total velocity computed at this point corresponds to the flow immediately downstream of the oblique shock wave. To verify whether it matches the desired freestream velocity, the oblique shock relations are applied as follows.
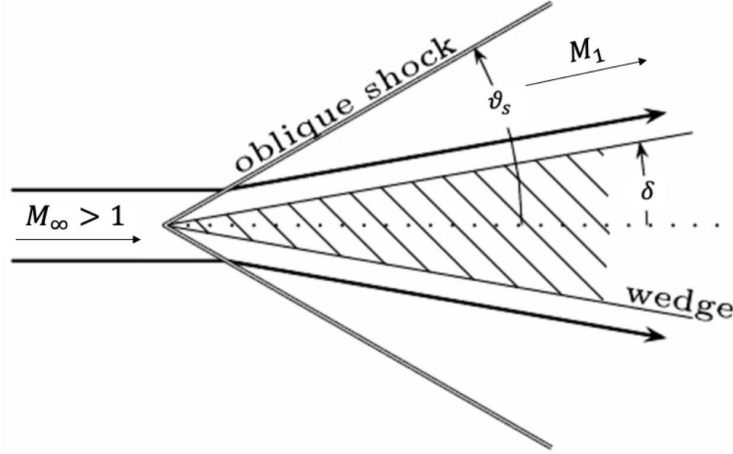
Figure 4.3: Supersonic flow over a wedge [28].

As illustrated in Fig. 4.3, given the desired freestream Mach number M_∞ an the truncation angle δ, the shockwave angle θ_s can be calculated by inverting

$$\cot \delta = \tan \vartheta_s \left[\frac{(\gamma + 1)M_\infty^2}{2(M_\infty^2 \sin^2 \vartheta_s - 1)} - 1 \right] \tag{4.22}$$

Now It is possible to determine the Mach number behind the oblique shock M_1

$$M_1^2 \sin^2(\vartheta_s - \delta) = \frac{(\gamma - 1)M_\infty^2 \sin^2 \vartheta_s + 2}{2\gamma M_\infty^2 \sin^2 \vartheta_s - (\gamma - 1)} \tag{4.23}$$

The total velocity, and consequently the Mach number, can be determined using the following relation

$$a = \sqrt{\gamma R T} \tag{4.24}$$

with a the speed of sound $[m/s]$, R the universal gas constant $[J/kgK]$ and T the temperature $[K]$, and

$$M = \frac{u}{a} \tag{4.25}$$

obtained from the integration of the Taylor-Maccoll equations is compared with M_1 and an iterative process is conducted on the intake efficiency until convergence is achieved. Additionally, by applying the oblique shock relations, the static pressure ratio, static temperature ratio, and total pressure ratio across the shock can be determined.

$$\frac{P_1}{P_\infty} = \frac{2\gamma M_\infty^2 \sin^2 \vartheta_s - (\gamma - 1)}{\gamma + 1} \tag{4.26}$$

$$\frac{T_1}{T_\infty} = \frac{\left[2\gamma M_\infty^2 \sin^2 \vartheta_s - (\gamma - 1)\right] \left[(\gamma - 1)M_\infty^2 \sin^2 \vartheta_s + 2\right]}{(\gamma + 1)^2 M_\infty^2 \sin^2 \vartheta_s} \tag{4.27}$$

$$\frac{P_{t1}}{P_{t\infty}} = \left[\frac{(\gamma + 1)M_\infty^2 \sin^2 \vartheta_s}{(\gamma - 1)M_\infty^2 \sin^2 \vartheta_s + 2}\right]^{\frac{\gamma}{\gamma - 1}} \left[\frac{\gamma + 1}{2\gamma M_\infty^2 \sin^2 \vartheta_s - (\gamma - 1)}\right]^{\frac{1}{\gamma - 1}} \tag{4.28}$$

4.7 Viscous effects
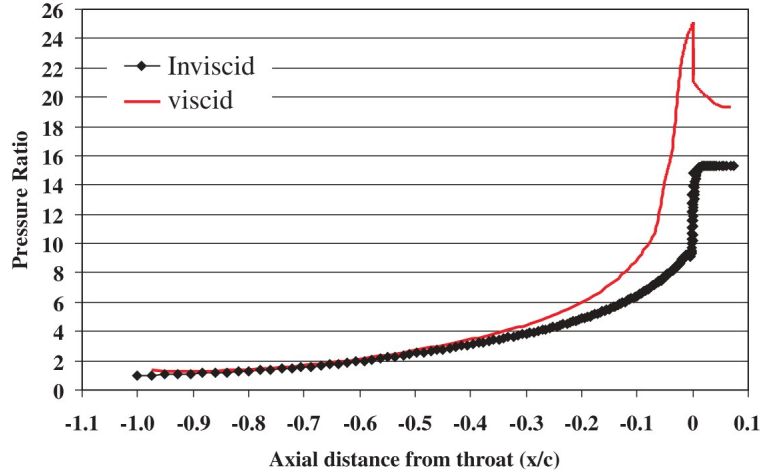
Figure 4.4: Comparison of inviscid and viscous surface static pressure in the uncorrected inlet [38].

The higher the efficiency of the intake, the longer and more slender its design tends to be, which in turn increases the surface area and shear stress near the leading edge. As a consequence, viscous losses become significantly higher. Moreover, due to the extended surface length, a thick boundary layer forms at the intake exit, increasing the risk of boundary layer separation and associated efficiency losses. The boundary layer development displaces the flow, causing the conical shock's focal point to shift upstream. As the shock propagates downstream, it reflects off the axis of symmetry and subsequently impinges on the intake surface ahead of the corner. Additionally, the presence of the boundary layer induces an overcompression of the internal flow, as it effectively reduces the available flow area by an amount corresponding to the boundary layer displacement thickness. This reduction leads to a higher pressure peak compared to the ideal case, further impacting the intake's performance, as shown in Fig. 4.4. To restore the inviscid flow topology and maintain the intended pressure distribution, the intake geometry must be adjusted to account for the boundary layer displacement thickness [38]. Therefore, accurately determining this thickness is crucial for a reliable assessment of intake performance. The complex interactions between shock waves and the boundary layer over the curved surfaces of Busemann intakes pose significant challenges in precisely identifying the boundary layer edge [39]. Typically, viscous corrections are applied only once to

65

obtain the final intake geometry. However, studies [40] have emphasized the importance of iterative corrections, where the displacement thickness is continuously updated to enhance accuracy. To account for viscous effects, the boundary layer displacement thickness is added to the inviscid contour, thereby widening the intake geometry and compensating for the additional contraction caused by the viscous boundary layer, as displayed in Fig 4.5.
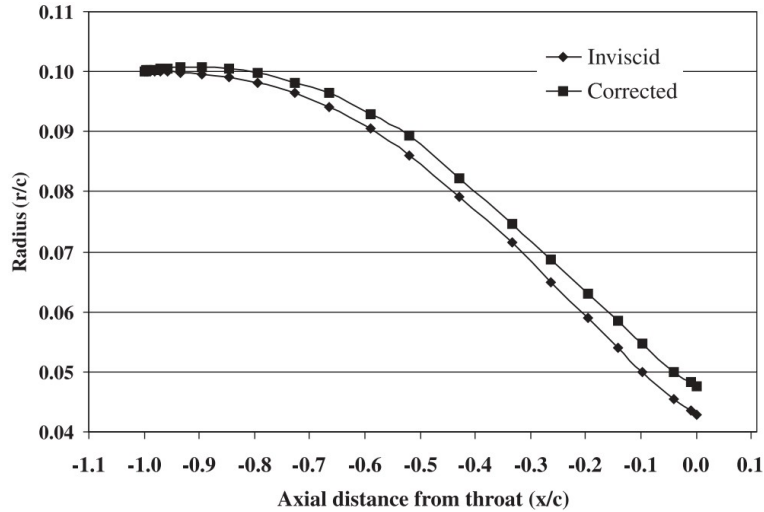
Figure 4.5: Comparison of inviscid and corrected internal profiles [38].

4.8   Startability of the Busemann intake

According to the Kantrowitz criterion for intake starting [26], the duct flow starts if the normal shock, initially positioned ahead of the intake, moves downstream and eventually exits the duct if the duct itself isn't chocked. It is important to note that this criterion must be valid for the normal shock throughout the entire duct length. The intake will successfully start if the shock at the inflection point continues propagating downstream and exits through the internal flow section, thereby satisfying the Kantrowitz condition. The entry area of the internal flow is defined by the conical surface at the inflection point, where the flow is perpendicular to the surface itself. At this location, a stationary, conical, and normal shock is consistent with the flow conditions. From a Busemann intake analysis, it is possible to determine the size of this entry area. To apply the Kantrowitz starting criterion, the precise value of this area must be computed.

4.8.1   Weak shock configuration

It is important to note that eq. (4.10) gives two solutions for given M_2 and δ_2: a weak and a strong shock. This result indicates that two distinct Busemann intakes can be generated, differing in the velocity of the exit flow. In the weak shock configuration, the exit flow remains supersonic, whereas in the strong shock configuration, it becomes subsonic. Due to its supersonic exit flow, the weak shock intake is more suitable for scramjet

66

applications. However, in such applications, the high level of flow contraction required makes it challenging for a Busemann intake with a weak shock to start spontaneously. To determine the startability of a wavecatcher Busemann intake, the following approach is adopted. First, a Busemann intake designed with a weak shock configuration is analyzed to evaluate whether it provides an adequate level of compression or not:

- With the weak shock angle specified, the integration of the Taylor-Maccoll equations begins using the initial values of M_3 and r.

- The integration proceeds until the inflection point is reached, where $u = 0$.

- The conical surface area at the inflection point is then calculated.

- The Kantrowitz criterion is applied at both the intake exit and the inflection point to determine whether the internal flow passage will start.

- If the intake successfully starts, the integration continues to determine the freestream Mach number M_∞ along with other performance parameters.
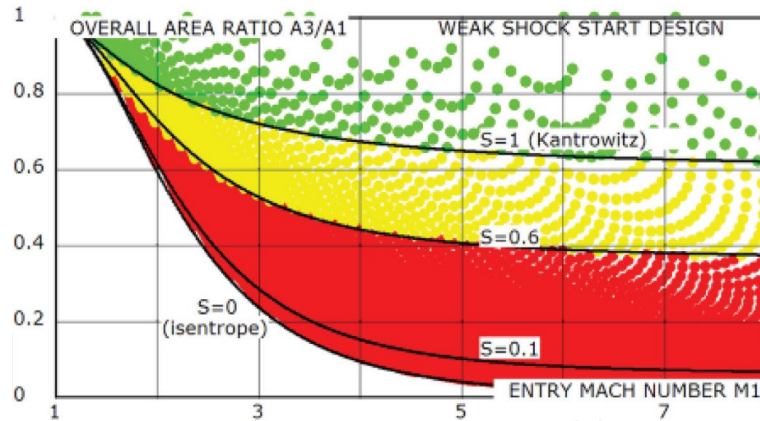
Figure 4.6: Busemann intake startability based on weak shock design: green—full Busemann start; green and yellow—wavecatcher start with spillage; and red—no start [11].

Numerous calculations were conducted, beginning with weak shock waves, and the results were represented on a graph plotting the area ratio A_3/A_1 against the entry Mach number, in Fig. 4.6. Each result is represented as a dot, with its color indicating the intake's startability. Green dots mean that the fully internal Busemann intake successfully starts, while yellow dots indicate that the wavecatcher Busemann intake module starts, (as determined by the fourth point above), and red dots represent cases where starting does not occur. Curves representing the "startability index" $S = \frac{A_1 - A_i}{A_k - A_i}$ illustrate the position of each dot on the overall area ratio scale. Here, $S = 0$ corresponds to the isentropic limit, while $S = 1$ aligns with the Kantrowitz criterion, with intermediate fractional values forming curves between these boundaries. The curve for $S = 0.6$ appears to effectively define the startability limit for wavecatcher Busemann intake designs based on the weak shock condition. As shown in the figure 4.6, the wavecatcher design reduces

the startable area ratio from approximately 0.6 to 0.4. However, this reduction remains insufficient for optimal performance. For efficient engine operation, it is preferable for intakes to function near the $S = 0.1$ curve in Figure 4.6. Unfortunately, weak shock Busemann intake designs that are capable of starting do not achieve the necessary level of contraction.

4.8.2 Strong shock configuration
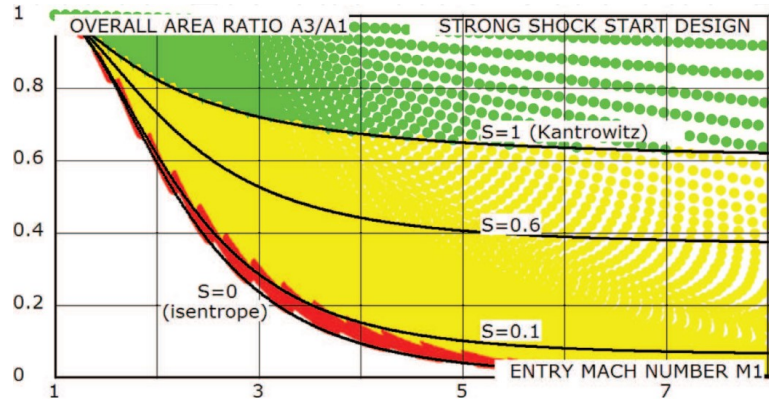
Figure 4.7: Busemann intake startability based on strong shock design: green—full Busemann start; green and yellow—wavecatcher start with spillage; and red—no start [11].

By following the previous steps, a strong-shock Busemann intake can be designed through the integration of the Taylor-Maccoll equations. The results are illustrated in Figure 4.7, where each outcome is represented as a dot: green indicates that the fully internal Busemann intake starts, yellow if the wavecatcher Busemann intake module starts (as determined in step fourth), while red denotes cases where the intake does not start. The strong shock configuration features a high overall contraction ratio but a low internal contraction, meaning that while it can start spontaneously at contraction levels suitable for scramjet applications as a wavecatcher, the presence of a strong shock and subsonic exit flow makes it unsuitable for a scramjet combustor. In a wavecatcher module, the strong shock near the start condition can be stabilized by applying appropriate backpressure. If the backpressure is reduced, the strong shock moves downstream and is replaced by a weak shock structure. This approach opens new possibilities: a Busemann intake module with a strong shock can be designed to start spontaneously at a high overall contraction ratio. Then, by lowering the backpressure, the strong shock can be eliminated, resulting in a supersonic exit flow with a weak shock structure, making the flow field suitable for scramjet operation. Notably, in this transition, the upstream flow—extending from the freestream to the strong shock location—remains unchanged, allowing the intake to function under the strong shock design flow up to the corner while ensuring successful starting. Since the internal contraction remains constant, it is theoretically possible to start the intake using the weak shock configuration from the outset. Thus, the strong shock Busemann shape serves as a design tool that enables a modified Busemann intake to achieve high compression and efficiency while maintaining a supersonic exit Mach

number. This intake configuration retains a high overall contraction ratio but features a low internal contraction that allows for spontaneous starting. The resulting supersonic exit flow is no longer conical, though it preserves axial symmetry.
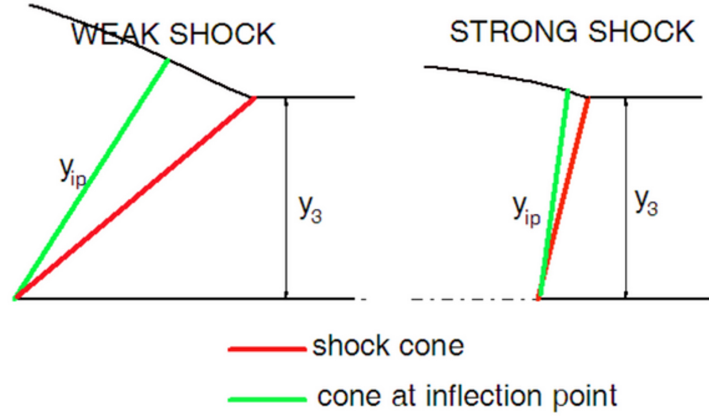
Figure 4.8: Comparison of weak and strong shock design [18].

Compared to the weak shock case (Figure 4.6), the strong shock design significantly improves startability, as reflected in the expanded yellow region, allowing starting conditions closer to the $S = 0.1$ curve, which is acceptable for scramjet applications. This improvement arises because, in the strong shock configuration, the angular separation between the strong shock (located at the corner) and the inflection cone is small Fig. 4.8, leading to similar values for the areas A_f and A_3, meaning that internal contraction is minimal. As a result, the conical normal shock at the inflection location can be more easily ingested. The goal of the strong shock design is to produce a wavecatcher Busemann intake that features a high overall contraction ratio with low internal contraction while ensuring spontaneous startability. The calculated intake geometry is compatible with a normal conical shock positioned at the inflection point, allowing for a selection of configurations where the internal contraction enables shock ingestion.

4.9   3D intake design methodology
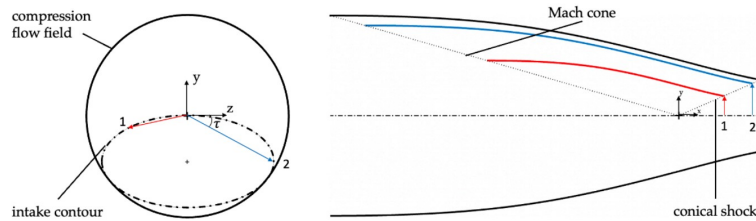
Figure 4.9: Schematic of streamline tracing with elliptical intake contour inside compression flow field [28].

69

Considering an axisymmetric streamtube, the fundamental Busemann flow is confined within it. However, its axisymmetric shape may not be easily integrated into the overall aircraft structure. Consequently, modifications to its cross-sectional shape are required. By tracing the streamlines of the Busemann flow, these modifications can be carried out while preserving the flow characteristics. This process involves assembling scaled Busemann streamlines to construct the intake's module wall surfaces.

The wavecatching technique is based on generating flow path surfaces that deviate from the classic axisymmetric Busemann flow surface. The procedure begins by selecting the desired Busemann flow and determining its streamline profile, $r = f(\theta)$, as shown in Figure 4.9. The intake surfaces are then created by assembling adjacent Busemann streamlines, defined as $\bar{r} = y(\phi)f(\theta)$, where r is the radial coordinate along the streamline, $y(\phi)$ is a scaling factor that varies between streamlines, and $f(\theta)$ represents the Busemann streamline shape [33].

The scaling factor quantifies the distance of a streamline from the axis of symmetry. The parameter ϕ uniquely identifies each streamline based on its position along the cross-sectional perimeter relative to the axis of symmetry. The scaling factor $y(\phi)$ is defined as the ratio between ϕ and the exit radius r of the original compression flow field. The angle τ is defined as the angle between the z-axis and the line connecting the symmetry axis to a given point on the cross-sectional perimeter. The Cartesian coordinates of the points defining the surface of the streamline-traced Busemann intake are then computed accordingly:

$$x = \bar{r}\cos(\theta) \qquad y = \bar{r}\sin(\theta)\cos(\tau) \qquad z = \bar{r}\sin(\theta)\sin(\tau) \qquad (4.29)$$

To simplify all this process, it was automated in MATLAB, where each streamline was saved as a separate `.txt` file and organized into a folder. Subsequently, a SolidWorks macro was developed to import each streamline as a curve. This automation enables the creation of a lofted surface and the generation of the 3D geometry, as illustrated in the figures 4.10 below.

Side

Front

Top

3D view
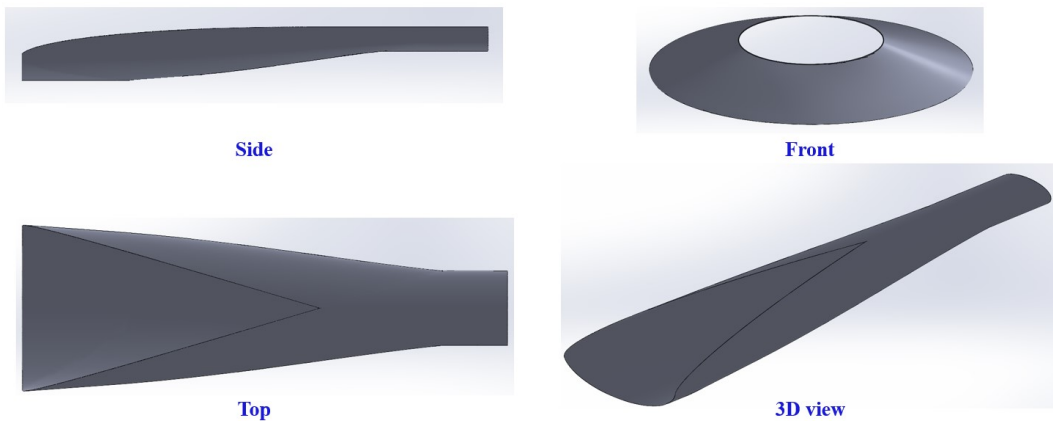
Figure 4.10: Streamline traced Busemann Intake designed for $M_\infty = 5$, $M_{exit} = 3$, $\delta = 5°$, with flate plate.

4.10   CFD

Once the designed geometries were generated using the MATLAB code, a Computational Fluid Dynamics (CFD) analysis was conducted to verify their consistency with analytical predictions and to assess the impact of applied corrections. Additionally, multiple simulations were performed to gain a deeper understanding of how various design choices influence flow development.

4.10.1   Mesh

For the numerical simulations, meshes were generated using the Ansys software package, specifically Workbench for the 2D cases and Fluent Meshing for the 3D cases. Since the 3D design is significantly more complex than the 2D ones, Fluent Meshing was preferred to ensure a higher-quality mesh. For the 2D cases, after conducting multiple simulations, a structured mesh was adopted for both inviscid and viscous cases. A structured mesh was chosen because it facilitates more accurate data extraction for calculating the boundary layer displacement thickness while also reducing computational costs of the mesh generation as the number of elements increases in the study. An example of the 2D mesh is shown in Figs. 4.11(a), 4.11(b). For the 3D mesh, refer to Section 5.2.1.
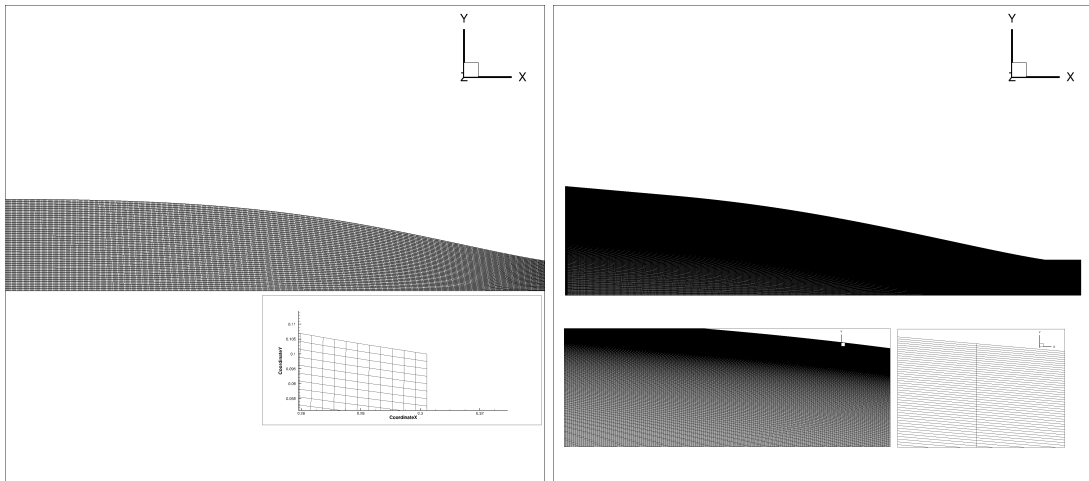
((a)) A uniform Structured Mesh for the inviscid case.

((b)) A structured mesh for the viscous case, with a bias factor applied to ensure that the first layer thickness is approximately $1 \times 10^{-4} m$, thereby achieving $y^+ < 1$.

4.10.2   Ansys Fluent

ANSYS Fluent was employed to solve the Reynolds-Averaged Navier-Stokes (RANS) equations. As a finite volume solver, Fluent was used with implicit time stepping in this study. The software also allows for domain parallelization across multiple cores, significantly improving computational efficiency—especially for the 3D case, which involves a higher number of elements and, consequently, greater computational cost.

For the viscous simulations, the Shear Stress Transport (SST) $k-\omega$ turbulence model was utilized, as it has been shown to accurately predict hypersonic intake flow fields [41].

To further reduce computational time, only half of the geometry was analyzed for the 2D case, applying an axisymmetric boundary condition along the x-axis. The remaining boundary conditions were applied as shown in Fig. 4.12.
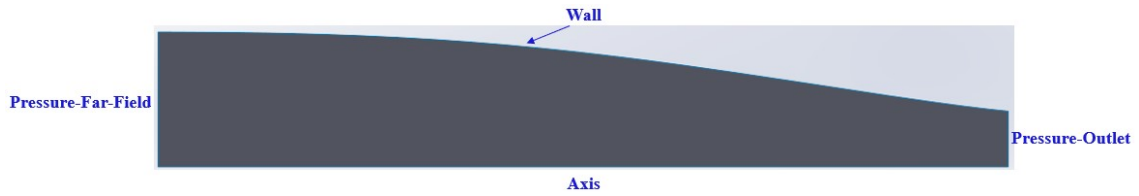
Figure 4.12: Boundary Conditions.

Chapter 5

Results and analysis

5.1 2D Analysis

This chapter presents the implementation of the intake design, as introduced in Chapter 4. The discussion begins with the output from the MATLAB design code (Section 4.4), and continues with the analysis of two-dimensional simulations. This is followed by a three-dimensional study conducted under both on-design and off-design conditions for multiple intake configurations.

5.1.1 Design code

In the MATLAB code presented in Section 4.4, the design parameters chosen for solving the Taylor-Maccoll equations are the upstream Mach number M_1, the downstream Mach number M_2, and the radius at the entrance of the combustion chamber r. Given these parameters, the code determines the optimal contour for maximum efficiency.

Since the equations solved are inviscid, the pressure and temperature distributions remain unchanged for different imposed values of r. Consequently, the intake length is dimensionalized by r to express the length ratio, providing a more generalized representation of the intake geometry.
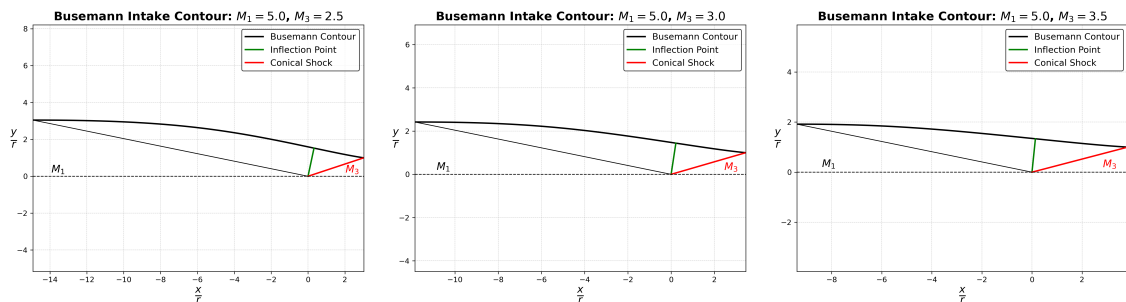
Figure 5.1: Busemann Intake for different M_3 value, 2.5, 3, 3.5 respectively.

Figure 5.1 illustrates a series of Busemann intake contour designs obtained by varying the downstream Mach number M_3, while keeping the upstream Mach number fixed at

73

$M_1 = 5$. The figure shows the resulting intake contours corresponding to different input parameters, highlighting the position of the conical shock and the inflection point. The characteristics and implications of the inflection point are discussed in greater detail in Section 4.5.

As expected, a lower M_3 requires a longer compression surface to gradually decelerate the flow through isentropic compression, whereas a higher M_3 results in a shorter compression surface.

This behaviour can be explained by considering that the optimal contour design aims to achieve maximum efficiency, where the only source of pressure loss is the conical shock wave. To minimize these losses and maximize efficiency, the intake should be designed to achieve the lowest possible Mach number ahead of the shock, allowing for maximum isentropic compression before the shock interaction. Since lower Mach numbers ahead of the shock, correspond to reduced pressure losses, an intake designed to pre-compress the flow to a lower Mach number before the shock will experience higher efficiency compared to a configuration where the flow remains at higher Mach numbers, leading to greater pressure losses.
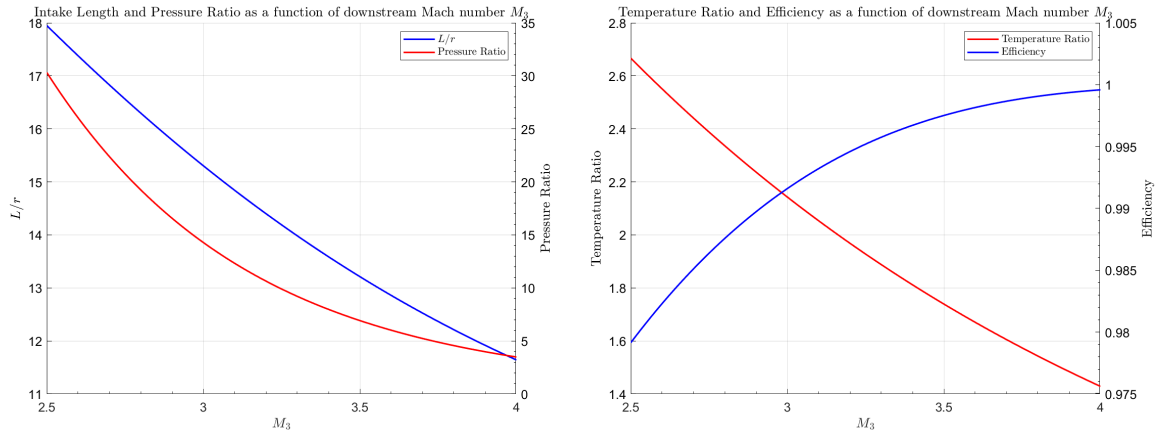
Figure 5.2: Intake length, pressure and temperature ratio and efficiency as a function of downstream Mach number M_3, with a constant upstream Mach number $M_1 = 5$.

M_3	P_{t_3}/P_{t_1}	L/h	A_3/A_1	S_i
2.5	0.9791	17.9492	0.1077	0.25098
2.75	0.9864	16.5612	0.1354	0.42758
3	0.9916	15.3048	0.1708	0.51832
3.25	0.9952	14.1895	0.2158	0.6191
3.5	0.9975	13.2129	0.2723	0.72973

Table 5.1: Different M_3 design properties for the same Mach flight $M_\infty = 5$.

In Fig. 5.2, the intake length, efficiency, pressure ratio, and temperature ratio are

plotted as functions of the downstream Mach number, M_3, for a constant upstream Mach number, $M_1 = 5$. As previously discussed, evaluating the variation of intake length with respect to M_3 becomes more intuitive in this representation. A lower M_3 results in a longer intake, whereas a higher M_3 corresponds to a shorter intake. Additionally, the figure illustrates how thermodynamic properties, such as pressure ratio, temperature ratio, and efficiency, are influenced by this parameter. A lower M_3 requires the intake to decelerate the airflow more significantly compared to a higher M_3, leading to an increase in pressure and temperature ratios while reducing efficiency due to the stronger shock interactions needed to slow down the incoming flow. Furthermore, the intake demonstrates high compression efficiency due to its specific design, with a minimum efficiency of 0.9791 observed in the most compressed case.

Additionally, Table 5.1 presents numerical values for five different designs. The table also includes the *Startability Index S_i*, introduced in Section 4.8, which quantifies *"how good is an intake to start"*. Specifically, values close to 0 indicate a design approaching the isentropic curve, making it more difficult to start, whereas values close to 1 correspond to a design closer to the Kantrowitz curve, facilitating easier starting. The table demonstrates that increased fluid compression corresponds to a lower S_i value, indicating that higher compression comes at the cost of a more challenging intake start, whereas a less compressed design facilitates easier starting.

5.1.2   Mesh convergence study

To validate the numerical simulation of the designed intake against the MATLAB-based predictions, a mesh convergence study is conducted for the 2D geometry. This analysis determines the minimum element size and the corresponding maximum number of elements beyond which the numerical results remain unaffected by discretization errors. For the numerical setup, the selected design parameters are $M_1 = 5$, $M_3 = 2.5$ and an exit radius of $r = 0.1m$. The ambient conditions correspond to an altitude of 25 km, with an ambient pressure of 2511 Pa and a temperature of 221.55 K.

A mesh convergence study was conducted using ten different mesh configurations, varying the element size until the results became independent of the mesh resolution, as shown in Table 5.2. A comparison of the finest and coarsest mesh configurations is presented in Figure 5.3. A structured mesh was selected due to its ability to enable faster mesh generation compared to an unstructured mesh for the same element size. Additionally, the structured configuration offers reduced computational cost and faster simulation time. Moreover, as it will be described later in Section 5.1.4, a structured mesh provides greater reliability in extracting data from the viscous simulation, particularly for calculating the boundary layer thickness.
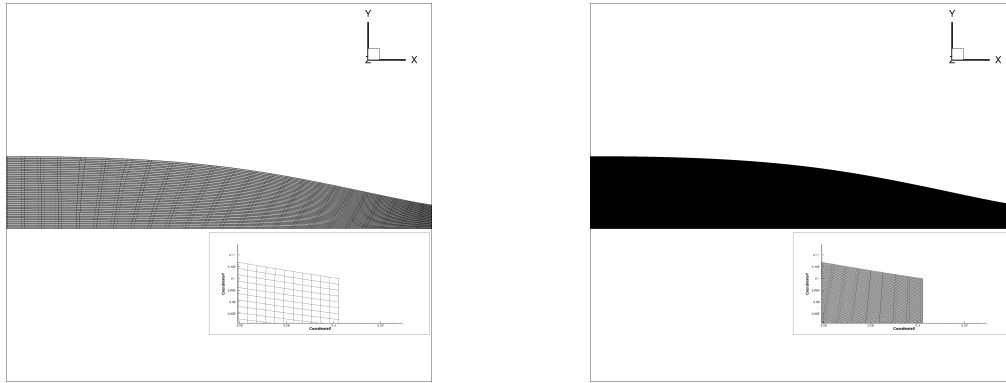
Figure 5.3: Comparison of the coarsest and finest mesh configurations, shown on the left and right, respectively.
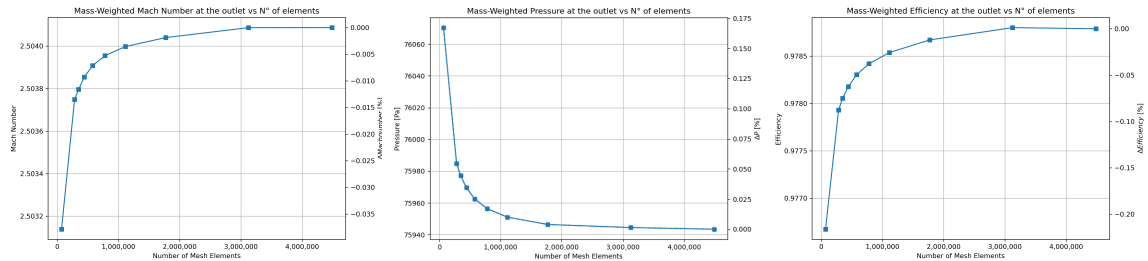
Figure 5.4: Mesh convergence study: Plot of pressure, Mach number, and efficiency at the outlet with different mesh resolutions.

76

Mesh	Element Size [m]	Mesh Elements	Pressure	Mach	Efficiency
Mesh 1	0.002	70547	76070.4	2.50314	0.97672
Mesh 2	0.001	283610	75984.9	2.50375	0.977931
Mesh 3	0.0009	348950	75977.1	2.5038	0.978053
Mesh 4	0.0008	442968	75969.7	2.50385	0.978178
Mesh 5	0.0007	579464	75962.5	2.50391	0.978304
Mesh 6	0.0006	780912	75956.4	2.50395	0.97842
Mesh 7	0.0005	1112900	75951	2.50400	0.978537
Mesh 8	0.0004	1771180	75946.4	2.50404	0.978671
Mesh 9	0.0003	3123914	75944.5	2.50409	0.9788
Mesh 10	0.0002	4487500	75943.4	2.50409	0.978789

Table 5.2: Mesh convergence study: variation of pressure, Mach number, and efficiency at the outlet with different mesh resolutions.

Analyzing Table 5.2 and Figure 5.4, a clear grid asymptote is observed. In particular, to optimize computational cost, Mesh 8 appears to be the most suitable choice, providing a balance between computational efficiency and result accuracy. Furthermore, the simulation results demonstrate strong agreement with the MATLAB-based design calculations. Specifically, for this intake configuration, the MATLAB code predicted an efficiency of 0.9791, while the asymptotic efficiency obtained from the simulations is approximately 0.9788, corresponding to a percentage variation of only 0.3%. Additionally, the outlet Mach number obtained from the simulations is consistent with the imposed design value of 2.5, further confirming the accuracy of the numerical approach. Furthermore, although the percentage difference, as shown in Fig. 5.4 and Table 5.2, does not differ significantly between the finest and coarsest meshes, it is evident from Figs. 5.5, 5.6, and 5.7 that the finest mesh captures the shock wave better, which is more defined at the origin (0,0). Additionally, as it will be discussed in more details in Section 5.1.3, a sufficiently refined mesh is crucial for resolving flow phenomena that would otherwise not be captured with a coarser mesh.
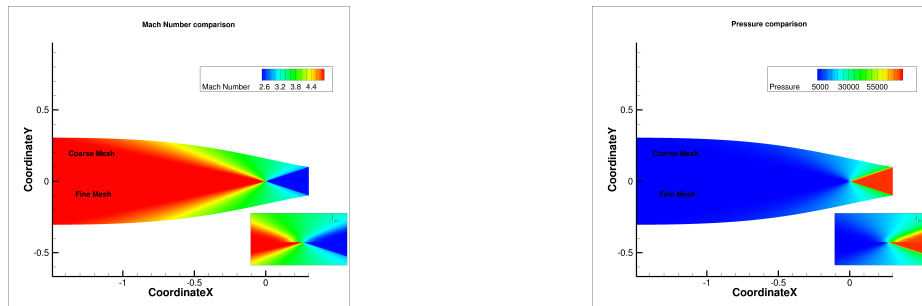
Figure 5.5: Mach Number and Pressure contour for the coarsest and finest mesh configuration.
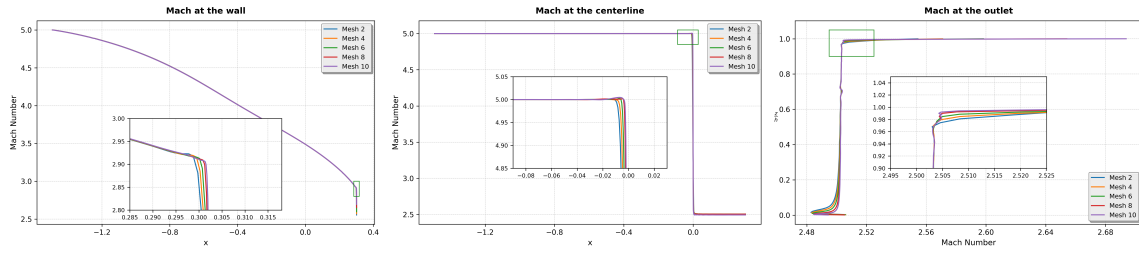
Figure 5.6: Mesh convergence study: Plot of mach distribution at the wall, axis and at the outlet.
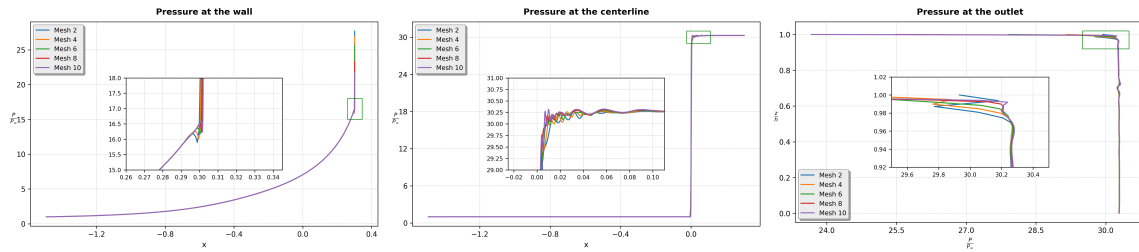
Figure 5.7: Mesh convergence study: Plot of pressure distribution at the wall, axis and at the outlet.

For the simulation in Fig. 5.8, a steady flight condition at Mach 5 and an altitude of 25 km is considered. This simulation will validate the predictions made by the MATLAB code design regarding variations in the downstream Mach number M_3. In particular, it will highlight the differences in the design with respect to the highly compressed case with M_3, illustrating the differences in length and area ratios.
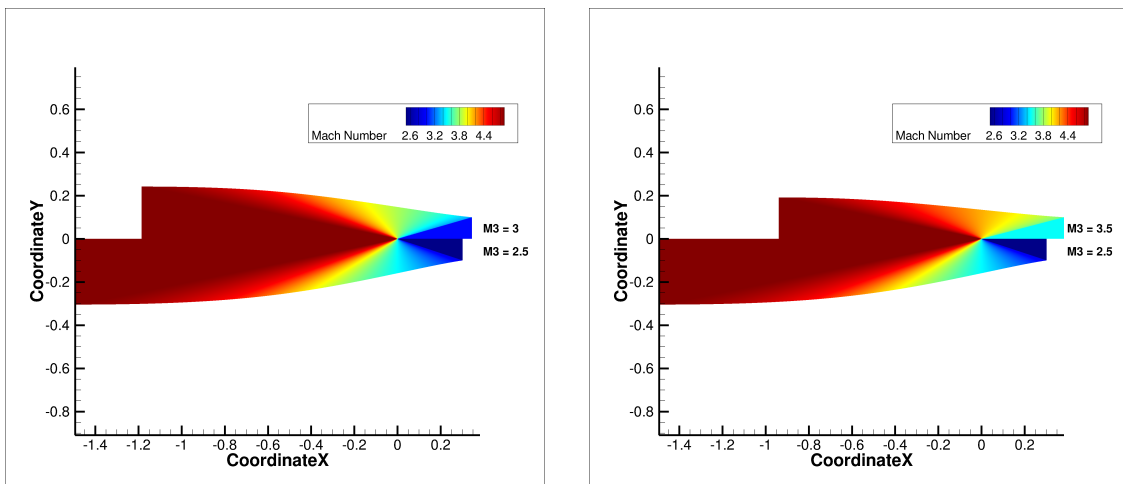
Figure 5.8: Comparison of different M_3 design.

	M_3			P_{t_3}/P_{t_1}			P_3/P_∞	
Design	Simulation	$\Delta[\%]$	Design	Simulation	$\Delta[\%]$	Design	Simulation	$\Delta[\%]$
2.5	2.5018	+0.072	0.9791	0.9741	-0.5107	30.3206	30.3650	+0.1462
3.0	3.0032	+0.107	0.9916	0.9911	-0.0504	14.2828	14.2564	-0.1848
3.5	3.5026	+0.074	0.9975	0.9972	-0.0300	6.9196	6.9103	-0.1344

Table 5.3: Comparison of different M_3 design properties obtained from the MATLAB code and the simulation for a flight Mach number of $M_\infty = 5$.

As shown in Table 5.3, the results obtained from the inviscid simulations are close to those computed with the design MATLAB code, thereby validating the accuracy of the design methodology.

5.1.3 Effect of Contour Truncation on Intake Performance

As discussed in Chapter 3, one of the main challenges associated with this type of intake is its considerable length, which is required to obtain an initial isentropic compression. However, excessive length increases viscous losses due to the larger wetted surface area available for boundary layer development. The Design Methodology employs the Taylor-Maccoll equation and terminates the integration when the imposed freestream conditions M_∞ are reached, ensuring that the final streamline is horizontally tangent to the freestream. Given this horizontal tangency condition, a significant portion of the leading edge may be excluded from the initial isentropic compression. This truncation results in both a reduction in weight—since a portion of the intake is removed—and a decrease in viscous losses due to the smaller surface area available for boundary layer growth.
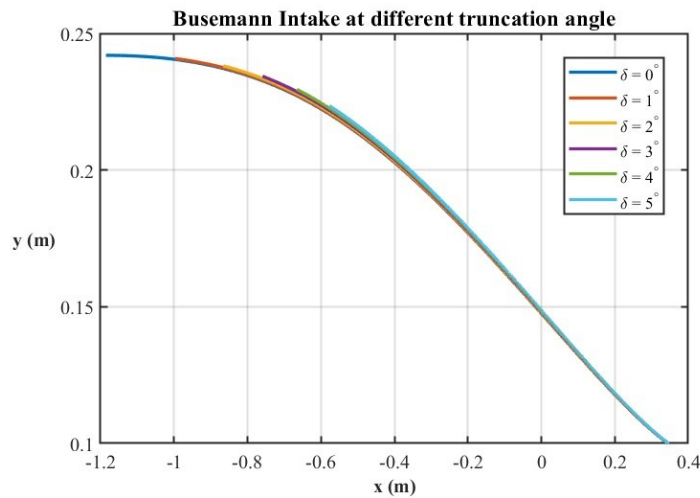
Figure 5.9: Influence of the truncation angle on the geometric length of the Busemann-designed intake.

Figure 5.9 illustrates the effect of terminating the integration process early by imposing a truncation angle $\delta > 0$ on the intake contour.

When a portion of the intake is truncated, a shock wave is generated at the leading edge and propagates toward the symmetry axis. Through this shock wave, the pressure increases, partially recovering the compression lost due to the truncation of the leading edge. As the truncation angle δ increases, the amplitude of the leading-edge shock wave also increases, distorting the compression flow field. This results in deviations in the computed pressure, temperature, and Mach number at the outlet compared to the analytically predicted values.

The internal conical flow causes the leading-edge shock wave to bend, disrupting the isentropic compression characteristic of the classical Busemann flow and leading to a nonuniform flow at the intake exit [37]. Ogawa and Mölder [42] analyzed the overall performance of shortened Busemann intakes, highlighting the transition in the shock reflection mode at the symmetry axis. Theoretically, regular shock reflection is not permissible at the centerline [43], leading to the formation of a small Mach disk that enables

shock reflection. This, in turn, generates a triple point where the incident shock wave, Mach disk, and reflected shock intersect, as it can be seen in Fig. 5.10.

As the truncation angle increases, the oblique shock wave angle also increases, intensifying the shock strength. Consequently, a stronger normal shock forms at the symmetry axis, exhibiting greater amplitude [37].
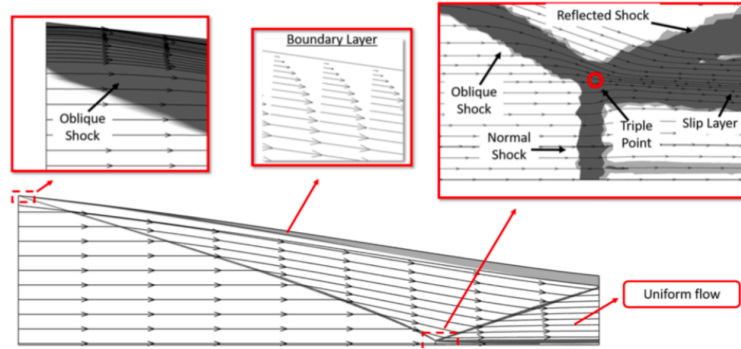
Figure 5.10: Flow field and shock structure in a truncated viscous Busemann intake [28].
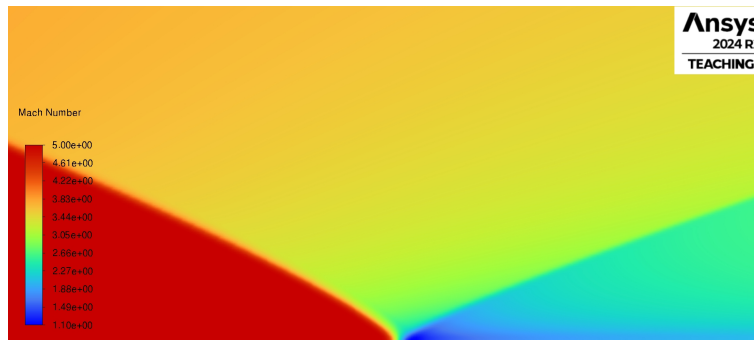
Figure 5.11: Flow-field solution with truncated geometry, without mesh adaption.

Figure 5.11 shows a converged steady-state solution for a downstream Mach number of $M_3 = 3$ and a truncation angle of $\delta = 5°$. As it has been observed from the mesh convergence study in Section 5.1.2, insufficient mesh refinement can lead to the inability to capture certain flow phenomena. In particular, in Figure 5.11, where a higher truncation angle (5°) had been used, the triple point observed in Figure 5.10 should be visible. However, in this case, the mesh resolution was not fine enough to accurately resolve this phenomenon.

To address this limitation, a mesh adaptation criterion was employed to refine the mesh in regions of shock waves. This refinement was performed using a mesh adaptation algorithm based on the pressure gradient. Figure 5.12 shows how this adaptation process evolved over the most significant iterations, showing both the changes in the mesh

structure and the corresponding improvements in the flow-field solution. As the mesh is refined using the pressure gradient-based algorithm, the refinement occurs in correspondence with the Mach disk, enhancing the resolution of the oblique shock wave generated by the truncated geometry, the reflected shock, and the slip layer.

Each mesh refinement step was performed at intervals of 1000 iterations, allowing sufficient time for the flow-field to adapt to the newly refined mesh and for the solution to reach convergence. Trial runs with smaller interval values resulted in inaccurate solutions, as the flow-field did not have enough time to evolve properly. This led to refinements in incorrect mesh regions and, consequently, a lack of convergence at each adaptation interval.

The selection of an appropriate mesh adaptation interval must balance computational cost and solution accuracy. Increasing the intervals allows longer time for the solution to converge, but is more computationally expensive, whereas decreasing the intervals can result in non-converged solutions. The optimal interval should thus be carefully chosen based on the specific requirements of the study.
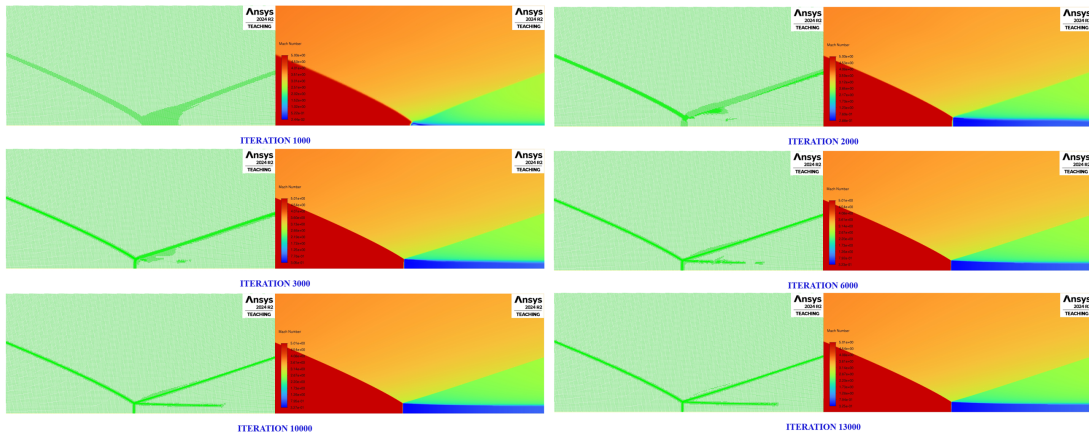
Figure 5.12: Mesh adaption iterations for capturing triple point.

Figure 5.13 presents different truncation angle designs for the same downstream Mach number $M_3 = 3$, ranging from $\delta = 1°$ to $\delta = 5°$ in the top contours of each plot, compared to the non-truncated configuration shown in the bottom part.

As observed, increasing the truncation angle results in a shorter intake contour, while the shock wave generated by the truncated leading edge shifts further downstream with increasing truncation angles relative to the non-truncated configuration. Additionally, the Mach disk amplitude increases with higher truncation angles, leading to a more disrupted and non-uniform flow at the outlet.
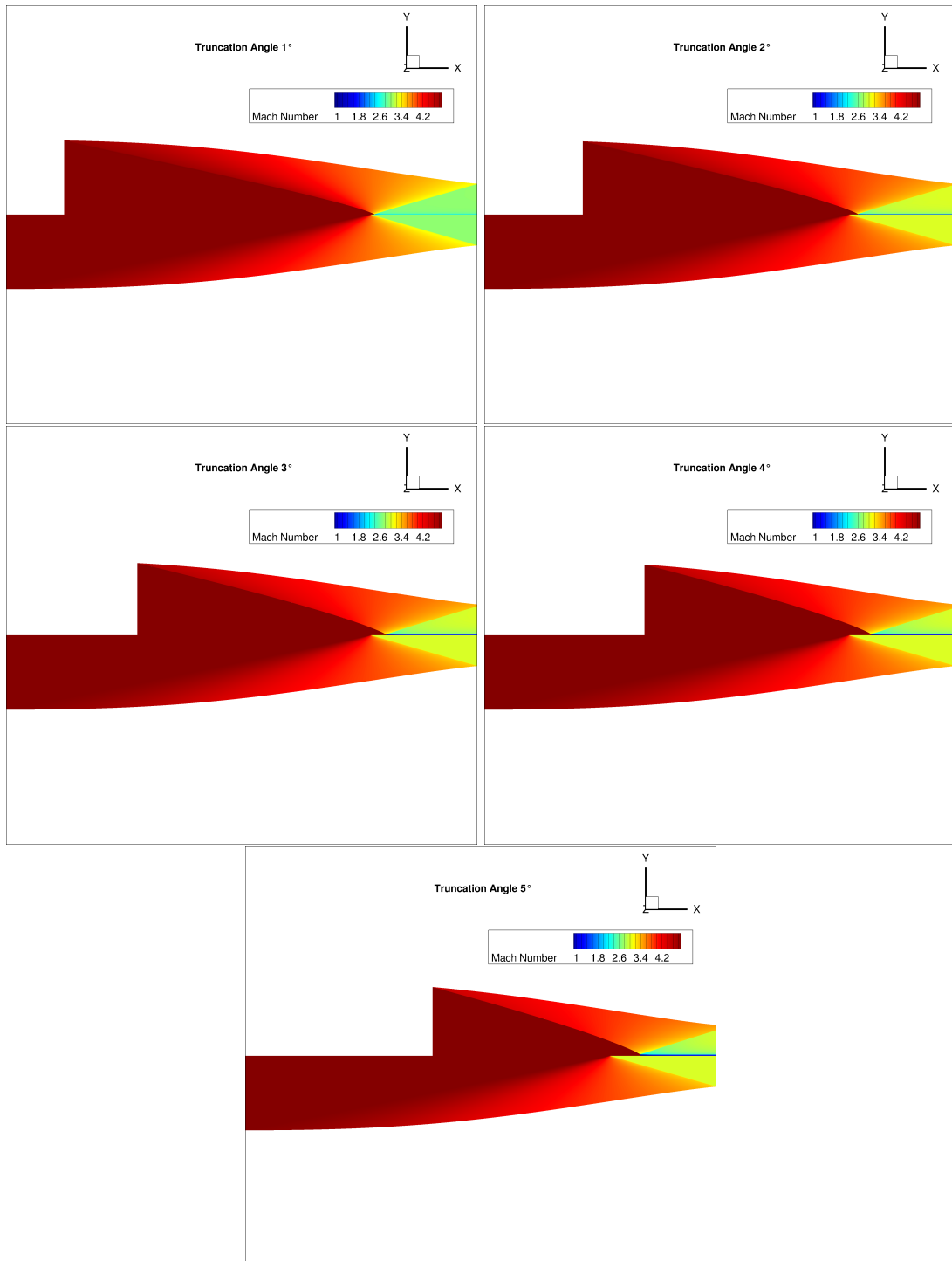
Figure 5.13: Flow field development with increasing truncation angle for $M_3 = 3$ design, compared to the non-truncated configuration. .

Figures 5.14 illustrate the normal shock for different truncation angles. It is clear

that an increase in the truncation angle results in a greater amplitude of the shock wave. Specifically, a higher truncation angle leads to an increased oblique shock wave angle, thereby intensifying the shock and resulting in a stronger normal shock along the symmetry axis [37].
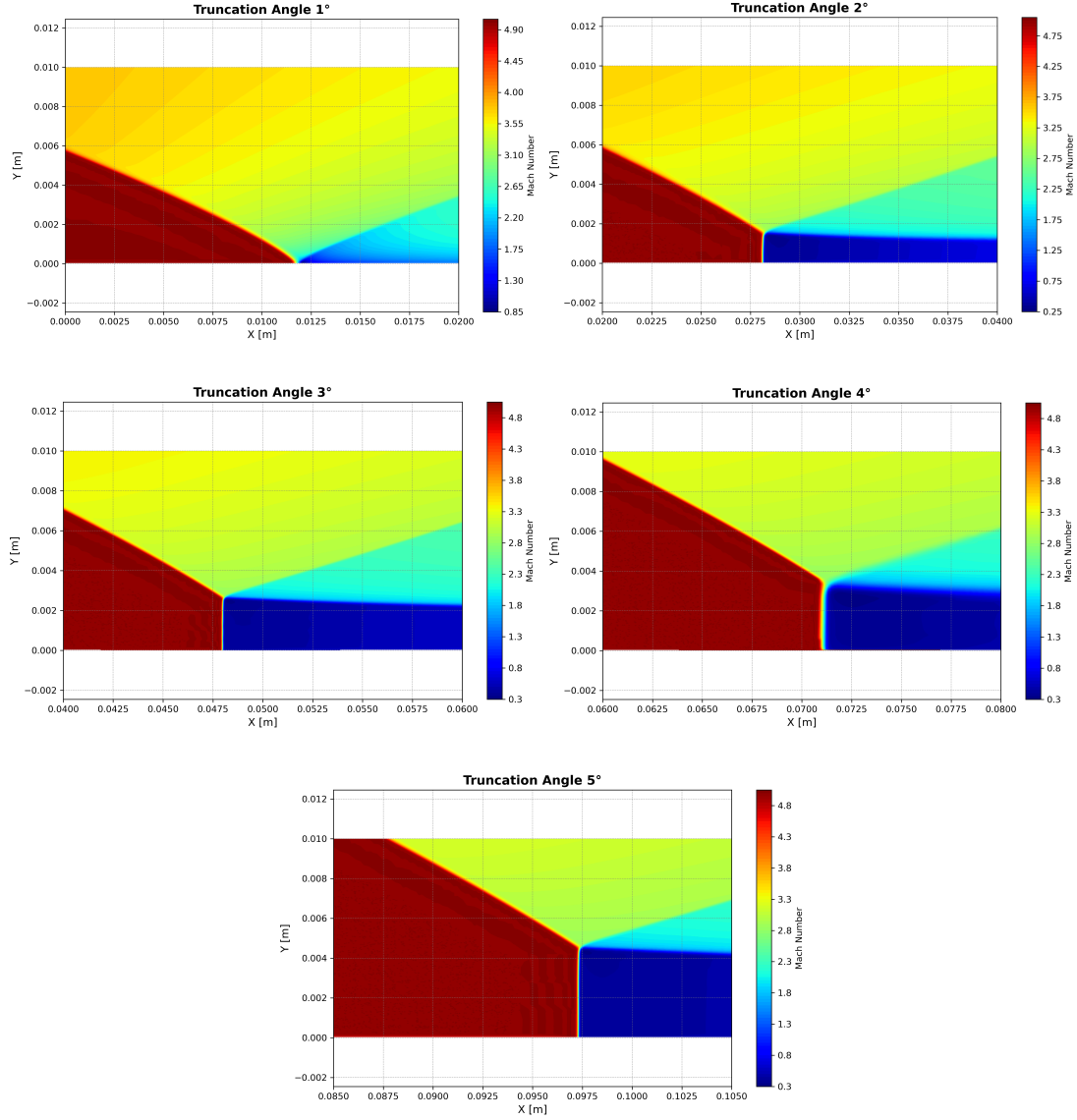
Figure 5.14: Detailed view of the triple point formation as the truncation angle increases.

Figures 5.15 illustrate the pressure and Mach number distributions along the wall and outlet sections of the intake for various truncation angles. It can be observed that the shock wave generated by truncating the leading edge partially compensates for the loss of initial compression but introduces additional total pressure losses. Furthermore, as depicted in Figures 5.13, increasing the truncation angle causes the conical shock

84

wave to shift downward. Consequently, the shock is no longer directly captured in the wall distribution plots due to this downward displacement. The absence of direct shock impingement results in higher Mach numbers and lower pressures in the affected regions of the outlet. Additionally, the Mach number distribution at the outlet confirms the presence of a stronger normal shock along the centerline and the associated triple-point structure.

The original MATLAB design methodology did not account for the effects of truncation. To address this limitation, the corrected Mach number immediately downstream of the truncated leading edge is calculated using oblique shock relations, assuming a deflection angle equal to the truncation angle δ. Subsequently, the Taylor–MacColl equations are integrated from the desired exit Mach number M_3 until this corrected initial condition is achieved.
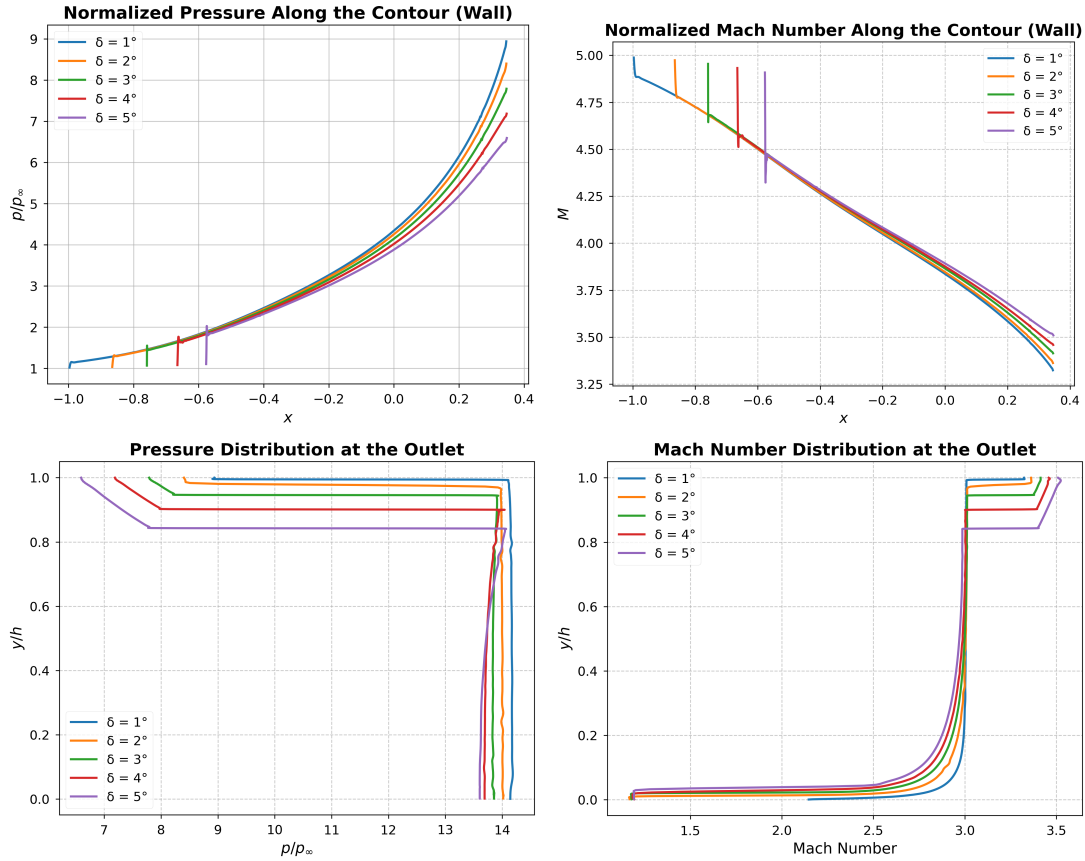
Figure 5.15: Mach number and pressure distribution along the wall and the outlet of various truncated geometries.

It has been shown that truncation reduces the overall length of the intake. However, truncating the intake's leading edge generates an oblique shock wave, which partially compensates for the lost compression but simultaneously increases total pressure losses. If the truncation angle is excessively large, the resulting flow field and performance parameters

deviate significantly from the intended design, negatively impacting intake operation.

A proposed mitigation strategy involves adding a neutral flat plate at the leading edge. This flat plate maintains the truncation angle relative to the freestream while moderating the formation of the oblique shock wave. The aim of the neutral flat plate is to make the shock wave converge at the focal point in order to preserve the desired flow characteristics at the outlet. Consequently, this approach preserves intake functionality and reduces performance losses. The required flat plate length depends on the truncation angle and freestream conditions, following the oblique shock angle relationship given by the equation:

$$\cot \delta = \tan \theta \left[\frac{(\gamma + 1)M_\infty^2}{2(M_\infty^2 \sin^2 \theta - 1)} - 1 \right] \tag{5.1}$$

$$M_1^2 \sin^2(\theta - \delta) = \frac{(\gamma - 1)M_\infty^2 \sin^2 \theta + 2}{2\gamma M_\infty^2 \sin^2 \theta - (\gamma - 1)} \tag{5.2}$$
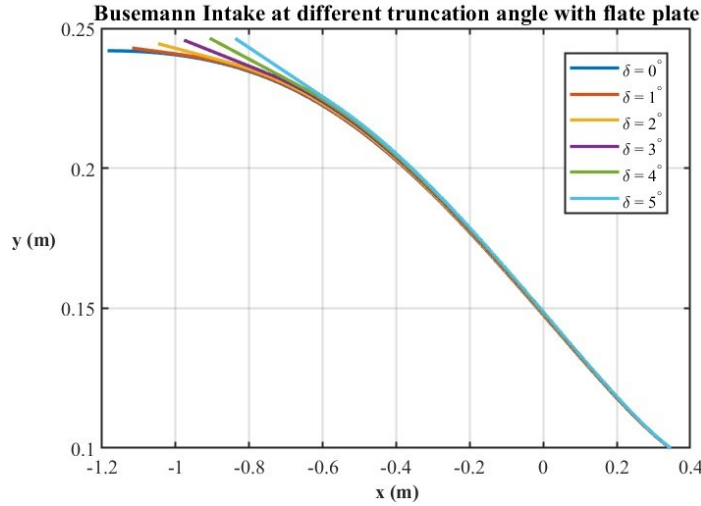
Figure 5.16: Truncated Busemann Contour with Flat Plate Design.

Figure 5.16 illustrates the modification introduced to the truncated intake design, which includes the addition of a flat plate maintaining the same truncation angle relative to the freestream flow. Figure 5.17 compares the length reductions achieved by truncated designs both with and without the flat plate. It is evident that the flat plate design results in a smaller length reduction compared to the purely truncated intake. However, the introduction of the flat plate is primarily justified by the requirement to achieve a more uniform flow distribution at the intake outlet. This uniformity is crucial because the airflow subsequently enters the combustion chamber, where uniform flow conditions significantly enhance combustion performance. Nonetheless, even with the flat plate modification at a truncation angle of $\delta = 5°$, a significant length reduction of approximately 22.5% of the original intake length is still achieved.
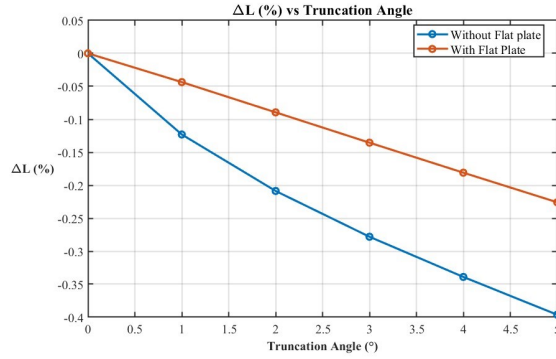
Figure 5.17: Comparison of length reduction relative to the original design for the truncated intake, with and without a flat plate.

Figures 5.18 present a comparison between the Mach number contour plots of the truncated geometry modified with a flat plate and the original (non-truncated) geometry for a downstream Mach number of $M_3 = 3$. The addition of the flat plate effectively prevents the focal point of the reflected shock wave from shifting downstream relative to its original position. Consequently, the triple-point structure is significantly less pronounced compared to the purely truncated configuration, resulting in improved flow uniformity at the outlet. Moreover, the reflected shock wave no longer shifts downward but rather impinges directly upon the wall slightly upstream of the corner, further contributing to a more favourable outlet flow field.
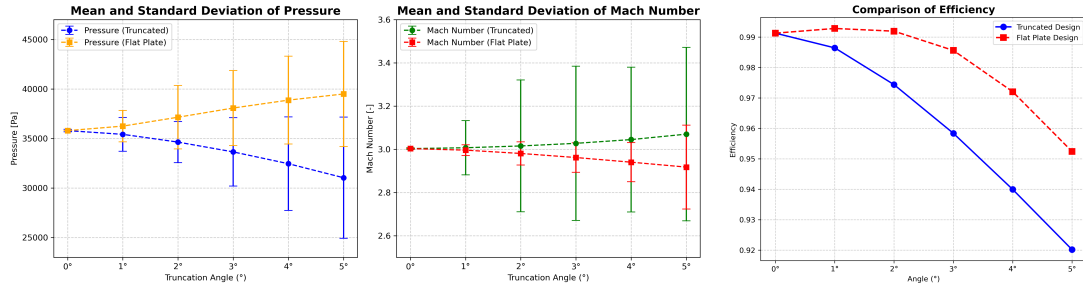
Figure 5.19: Efficiency, Standard Deviation and Mean Value of Pressure and Mach number for truncated design with and without flat plate.

Figures 5.19 show the efficiency, standard deviation and mass-weighted average values of pressure and Mach number at the intake outlet for different truncation angles, considering both truncated configurations—with and without a flat plate—for the same downstream design Mach number $M_3 = 3$. These parameters are crucial indicators for evaluating the flow uniformity at the outlet; notably, a lower standard deviation corresponds to a more uniform flow. As illustrated in Figures 5.19, the truncated design equipped with a flat plate exhibits significantly lower standard deviations for both pressure and Mach number compared to the configuration without the flat plate. This confirms that the inclusion of a flat plate effectively enhances outlet flow uniformity. Furthermore, it can be observed that the addition of the flat plate increases the available
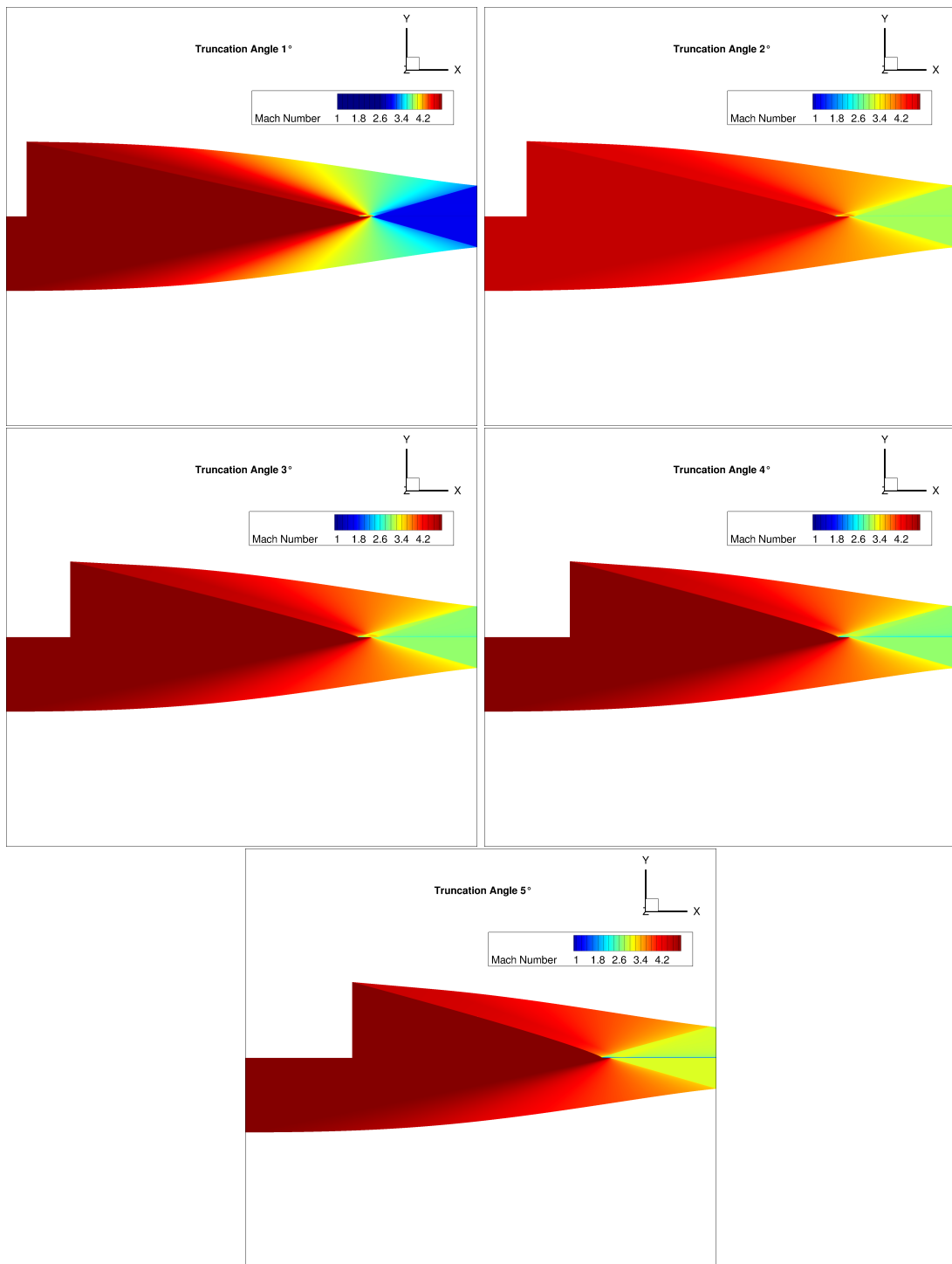
Figure 5.18: Flow field development with increasing truncation angle for $M_3 = 3$ design with flat plate.

surface area for flow compression. This explains the observed tendency for higher average pressure and correspondingly lower average Mach number at the outlet compared to the purely truncated design.

To further assess the performance differences between these two designs, the intake efficiency is also plotted in Figure 5.19. Once again, the flat plate configuration demonstrates improved performance by minimizing total pressure losses relative to the truncated design without this modification. Consequently, incorporating the flat plate represents a well-justified design choice for achieving better overall intake performance.
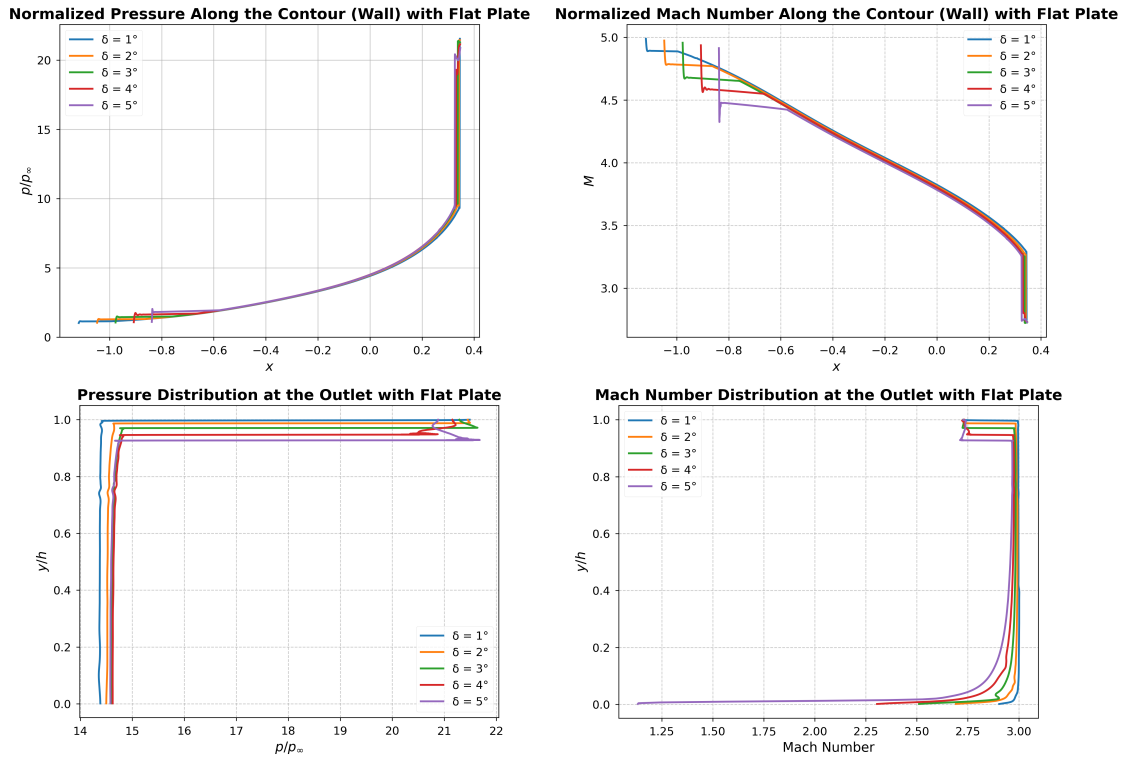
Figure 5.20: Mach number and pressure distribution along the wall and the outlet of various truncated geometries with Flat Plate Design.

For a complete analysis, Figures 5.20 present the pressure and Mach number distributions along the wall and at the outlet for the modified truncated geometry with the flat plate. As previously discussed, the flat plate configuration allows the shock wave to impinge directly on the wall, as clearly illustrated in Figures 5.18. This is in contrast to the purely truncated design shown in Figures 5.15, where the reflected shock wave does not directly reach the wall. Moreover, the contribution of the initial flat plate surface in compressing the incoming flow is evident and further confirmed by the higher mass-weighted average pressure values reported in Figures 5.19.

Additionally, from the Mach number distribution plots at the outlet, it can be observed that the triple-point structure is less pronounced compared to the truncated design

without the flat plate. As a consequence, the triple-point phenomenon has a reduced impact on the outlet conditions. The corresponding outlet pressure distribution also reveals higher pressure ratios, indicative of the reflected shock wave from the wall toward the outlet.

5.1.4 Viscous Correction

The theoretical axisymmetric Busemann intake, under inviscid flow conditions, is widely regarded as an efficient compression system and is frequently used as a reference model for hypersonic intake studies. In the previous Section, both fully enclosed and truncated inviscid Busemann intakes were analyzed to assess the influence of truncation angle and exit Mach number on intake performance. However, for a more accurate representation of real-world conditions, it is essential to incorporate a viscous correction methodology to account for boundary layer growth along the intake walls. The primary impact of viscosity is an increase in the intake contraction ratio, leading to a flow field that deviates significantly from the inviscid case. As a result, pressure rises within the intake, leading to higher static pressure and temperature at the exit. To apply viscous corrections, the geometry is extended normal to the surface by the computed boundary layer displacement thickness. Typically, this correction is applied once to obtain the viscous-corrected geometry. However, due to the complexity of the compression process at high supersonic speeds, an iterative correction procedure is required for improved accuracy. To validate the viscous correction procedure, a truncated Busemann contour with a truncation angle of $\delta = 5°$ is considered, corresponding to one of the 3D simulation cases. The intake is designed to capture a uniform freestream flow at Mach 5, with a static pressure of 2511 Pa and a temperature of 221.55 K. The target exit Mach number is $M_3 = 2.5$, with an exit radius of 1 m. The viscous simulations are conducted using the Shear Stress Transport (SST) $k - \omega$ Reynolds-Averaged Navier-Stokes (RANS) model, assuming adiabatic wall conditions and employing a wall-resolved approach for boundary layer modelling. The computational domain consists of a structured mesh, as shown in Fig. 5.21, where a bias factor is applied to increase resolution near the wall, ensuring a minimum cell thickness of $1 \times 10^{-5} m$, to maintain $y^+ < 1$. This meshing strategy is chosen to provide a structured grid suitable for extracting near-wall data required for computing the boundary layer thickness. Following the viscous simulations, total enthalpy profiles normal to the wall are extracted to determine the boundary layer displacement thickness, which is subsequently used to refine the intake geometry.
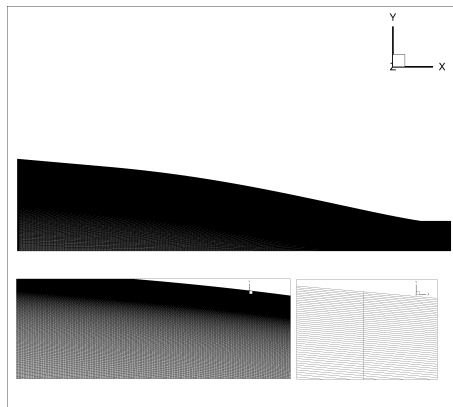
Figure 5.21: Detail of the structured 2D mesh using Bias Factor for resolving the boundary layer.
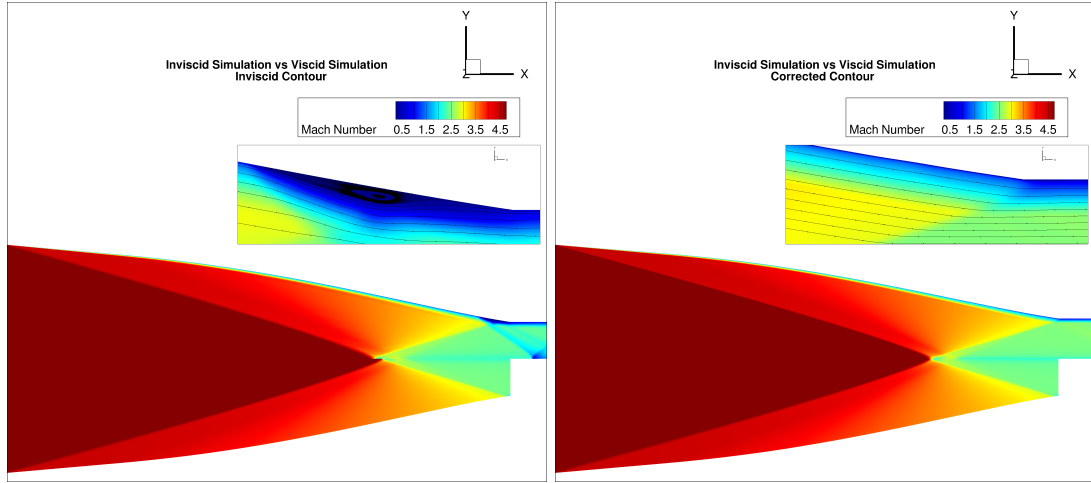
Figure 5.22: Comparison of inviscid and viscous simulations for the original (left) and final corrected (right) intake contours.

As shown in Fig. 5.22, the top contour on the left represents the viscous simulation of the original intake geometry, without any modifications. It is evident that the boundary layer growth significantly alters the flow field compared to the inviscid case, leading to increased flow compression due to the thickening boundary layer. Additionally, a strong Shock Wave–Boundary Layer Interaction (SWBLI) is observed (see Sec. 2.6.2), where the shock wave induces boundary layer separation, resulting in the formation of a separation vortex and increased pressure losses.

In contrast, the right side of Fig. 5.22 presents the final iteration of the corrected viscous contour, which incorporates modifications to account for the boundary layer displacement thickness. The viscous flow field of the corrected contour matches that of the inviscid configuration, and, importantly, the shock wave no longer induces strong interactions with the boundary layer, thereby preventing the formation of separation vortices.
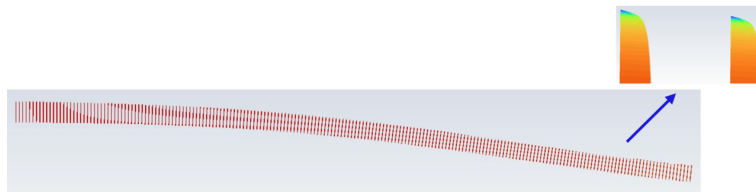
Figure 5.23: Boundary layer data extraction from the viscid simulation through 200 lines.

To calculate the displacement thickness induced by the boundary layer growth, an initial set of 200 lines is generated normal to the contour wall (see Fig. 5.23). Along these lines, the total enthalpy h_0, velocity magnitude u, and density ρ are extracted.

To compute the boundary layer edge—and consequently the displacement thickness—a MATLAB script was developed to extract the boundary layer edge from the total enthalpy distribution. The assumption of adiabatic wall conditions ensures that total enthalpy gradients are confined within the boundary layer, making total enthalpy a

reliable indicator for its extent.

The detection algorithm proceeds from the wall outward and finds the boundary layer edge when the following two conditions are simultaneously satisfied:

- The total enthalpy reaches within 1% of the freestream value;

- The gradient of total enthalpy with respect to the wall-normal distance approaches zero.

For the second condition, due to the limitations of machine arithmetic (i.e., the absence of an absolute zero), the total enthalpy gradient is first computed and then normalized by its maximum value—corresponding to the freestream. A threshold criterion of 1×10^{-3} is applied to identify points where the normalized gradient is effectively zero, indicating the location of the boundary layer edge.

Figures 5.24 illustrate the velocity and total enthalpy profiles along a representative wall-normal line. The red dashed line denotes the boundary layer edge as detected by the MATLAB algorithm described above.
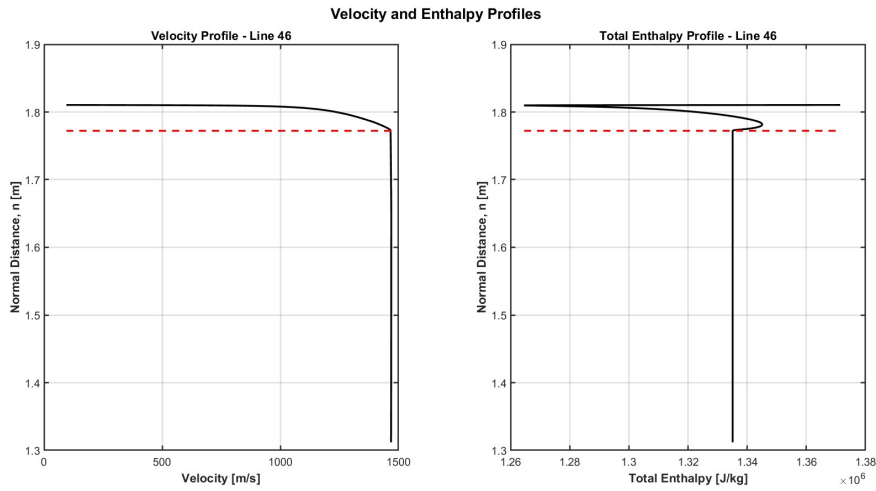
Figure 5.24: Velocity and Total Enthalpy profile and boundary layer edge indicated in red.

Once the boundary layer edge is identified for each extracted wall-normal line, the displacement thickness δ^* is computed using the following integral expression:

$$\delta^* \equiv \int_0^{y_e} \left(1 - \frac{\rho u}{\rho_e U_e} \right) dy \tag{5.3}$$

in which the index e represents quantities evaluated at the boundary layer edge.

After calculating the boundary layer displacement thickness, it is added in the wall-normal direction to the original inviscid contour to generate the first iteration of the corrected geometry. This procedure—comprising the extraction of displacement thickness from the viscous simulation and the application of the corresponding geometric correction—is repeated iteratively until convergence is achieved.

Figures 5.25 illustrate the computed boundary layer and displacement thickness profiles, as well as the resulting first corrected intake contour.
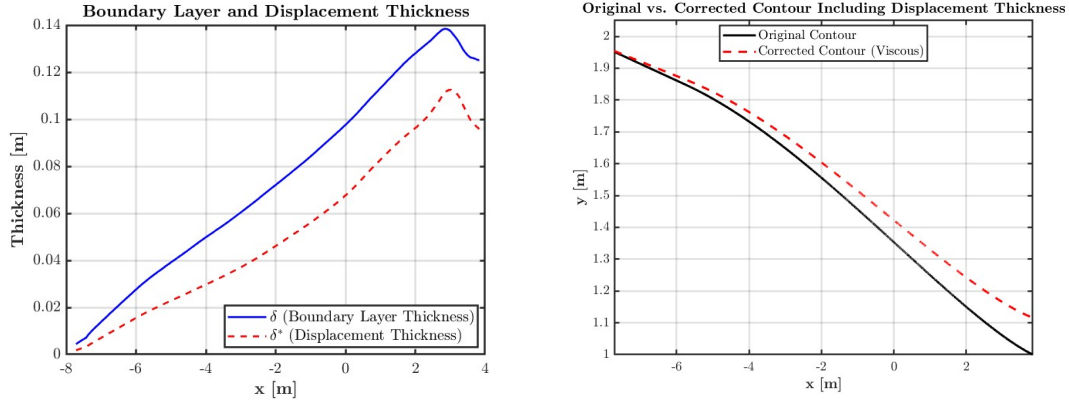
Figure 5.25: Displacement thickness and boundary layer profile (left), and corrected intake contour accounting for viscous effects (right).

Figure 5.26 shows the evolution of the boundary layer displacement thickness across successive correction iterations. A significant difference is observed between the displacement thickness obtained in the first iteration and that of the final one, highlighting the necessity of the iterative procedure.

This iterative correction has a substantial impact on the resulting flow field. In the first iteration, the viscous simulation is performed using the original inviscid contour. As shown in Fig. 5.22, this configuration leads to strong shock-wave/boundary-layer interaction, resulting in boundary layer separation. In contrast, the final iteration—based on the corrected contour—preserves the intended inviscid flow field in the viscous simulation, with no separation occurring.
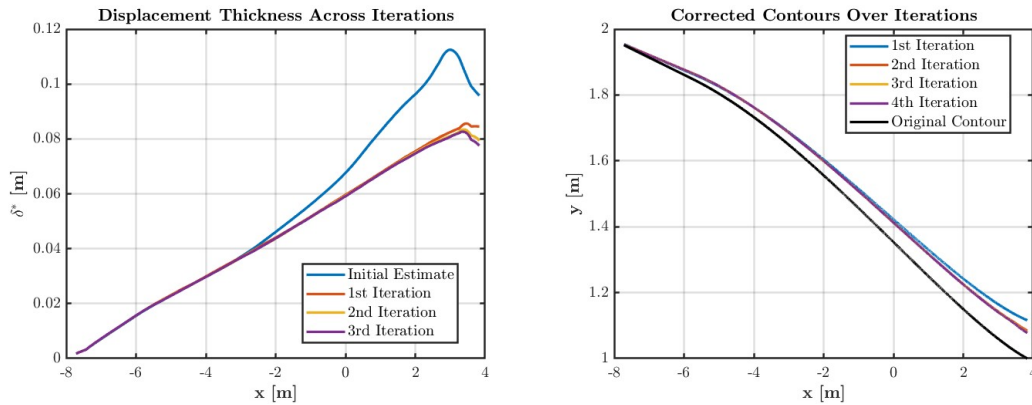
Figure 5.26: Displacement thickness and corresponding corrected contours over multiple iterations.

Further insights into the effect of the viscous contour correction can be drawn from the outlet flow parameters reported in Table 5.4. In particular, iteration 0 corresponds

94

to the viscous simulation performed on the uncorrected (inviscid) contour. As previously discussed, in this configuration, the growth of the boundary layer leads to additional flow compression, resulting in a higher static pressure and a lower Mach number at the outlet compared to the ideal inviscid solution.

On the other hand, the final iteration—based on the corrected contour—shows a restored agreement with the inviscid solution: the outlet Mach number is effectively preserved, and the static pressure closely matches the ideal inviscid result. This confirms the effectiveness of the correction in compensating for the viscous displacement effects.

Regarding the total pressure efficiency, it is expected that viscous simulations will not achieve the ideal values of the inviscid case, as the latter is based on the Euler equations and does not account for viscous losses. Nevertheless, the efficiency obtained in the final iteration remains relatively high, indicating minimal additional losses. The comparison also emphasizes the importance of the iterative correction: in the first iteration, where strong shock wave–boundary layer interactions and flow separation are present, the efficiency is lower than in the final, corrected configuration.

Iterations	Mach outlet	Pressure outlet [Pa]	Efficiency
0 (inviscid)	2.504	70547	0.979
0	2.136	107940	0.825
1	2.449	63986	0.875
2	2.449	69915	0.876
3	2.506	69973	0.877

Table 5.4: Impact of contour correction on outlet flow properties: Mach number, static pressure, and total pressure efficiency.

5.1.5   Unsteady Analysis of Intake Startability

As described in Section 3.3, this class of hypersonic intakes is prone to operate in an unstarted condition under certain off-design scenarios—a situation that must be avoided due to the associated performance degradation, reduced mass flow rate, and potential instability of the overall propulsion system. In practice, the design of a hypersonic vehicle powered by air-breathing engines presents several challenges, among which the intake starting problem is one of the most critical. These engines rely on the ability to ingest large amounts of air and compress it efficiently to high pressures—often up to 30 times the freestream value. The compressed air is then mixed with fuel in the combustor to increase its internal energy before being expanded through a nozzle to generate thrust. However, the process of starting and unstarting an intake is inherently unsteady and complex, often characterized by localized flow phenomena such as shock-shock interactions, moving shock waves, contact surfaces, slip lines, and vortex structures. Time-accurate Computational Fluid Dynamics (CFD) simulations were conducted for studying these transient processes in detail. In this section, unsteady inviscid simulations were performed to replicate the dynamic unstarting behavior of a fixed-geometry intake by imposing high temporal and spatial gradients at the domain boundaries [44]. The goal of this analysis is to investigate the mechanisms that govern the transition between started and unstarted conditions and to identify the critical parameters that trigger flow breakdown. This contributes to a better understanding of the operational robustness of the intake and supports the development of design strategies to prevent unstart during off-design or transient flight conditions.
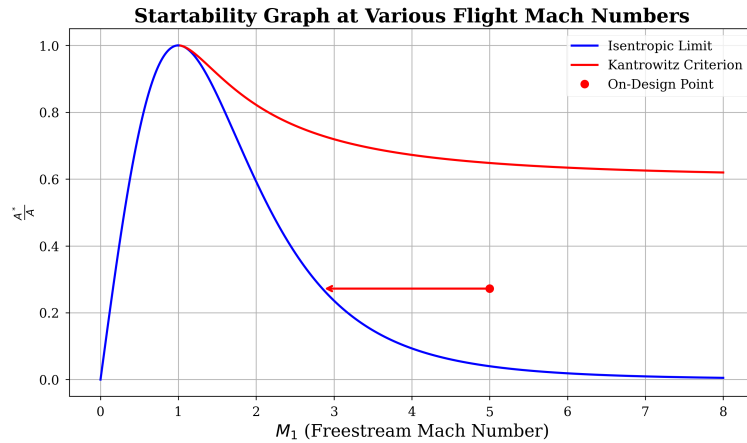
Figure 5.27: Detail of the isentropic limit and Kantrowitz criterion, illustrating the reduction in freestream Mach number from the on-design condition to the unstart threshold for an intake with $M_3 = 3.5$ and an area ratio of $A^*/A = 0.27$.
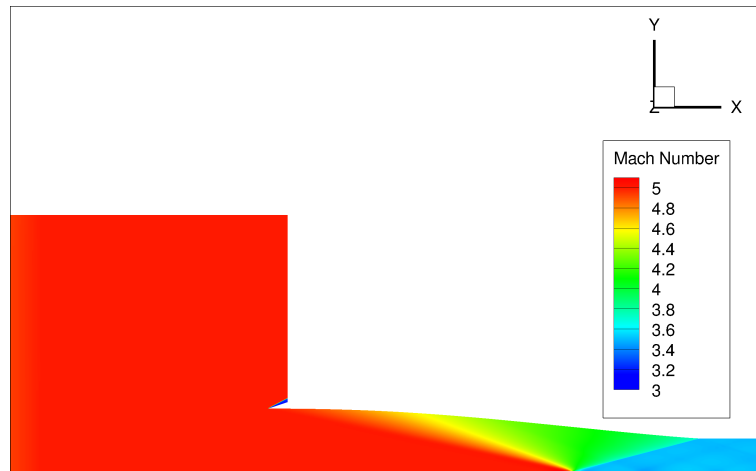
Figure 5.28: Detail of intake flow-field On-Design condition initial time $t = 0$ s.

Figure 5.27 shows the critical area ratio corresponding to the intake presented in Figure 5.28, along with the objective of the unsteady simulation: to drive the intake into an unstarted condition by crossing the isentropic limit curve.

In this analysis, the inlet boundary conditions are made time-dependent, and the freestream Mach number is gradually reduced from $M_\infty = 5$ to $M_\infty = 2.80$. This approach allows for the investigation of the dynamic behavior of the intake during deceleration and the identification of the precise conditions that lead to unstart.
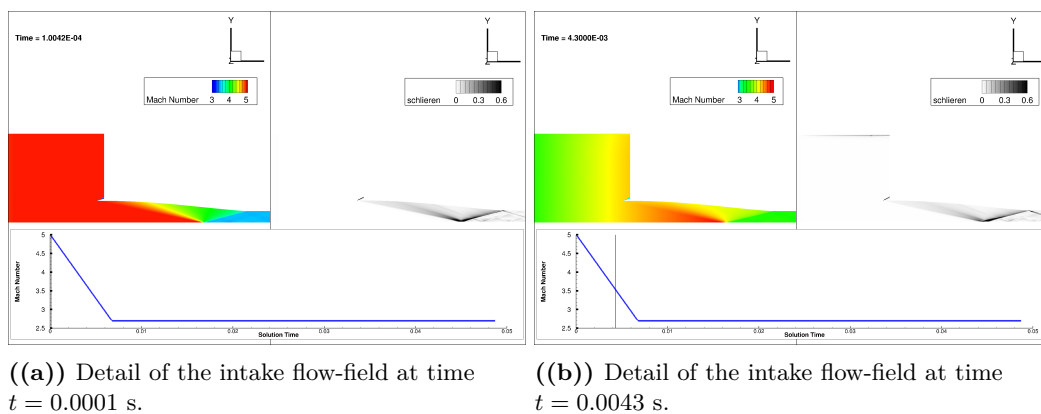
((a)) Detail of the intake flow-field at time $t = 0.0001$ s.

((b)) Detail of the intake flow-field at time $t = 0.0043$ s.

Figure 5.29: Mach number contour and Schlieren visualization, along with the time history of the inlet freestream Mach number.

As shown in Figure 5.29(b), the outlet section begins to respond to the changes in inlet conditions only after approximately $t = 0.0043$ s. This is evident from both the Mach number contour and the Schlieren visualization, which reveal the upstream displacement of the shock system induced by the evolving boundary conditions.
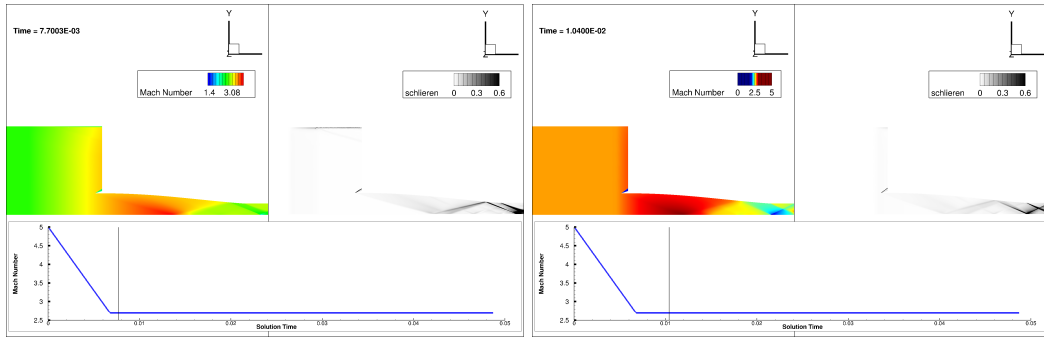
((a)) Detail of the intake flow-field at time $t = 0.0077$ s.

((b)) Detail of the intake flow-field at time $t = 0.0104$ s.

Figure 5.30: Mach number contour and Schlieren visualization, along with the time history of the inlet freestream Mach number.

As shown in Figure 5.30(a), the plot of the Mach number at the inlet section indicates that the boundary condition has reached its minimum value of $M_\infty = 2.80$.
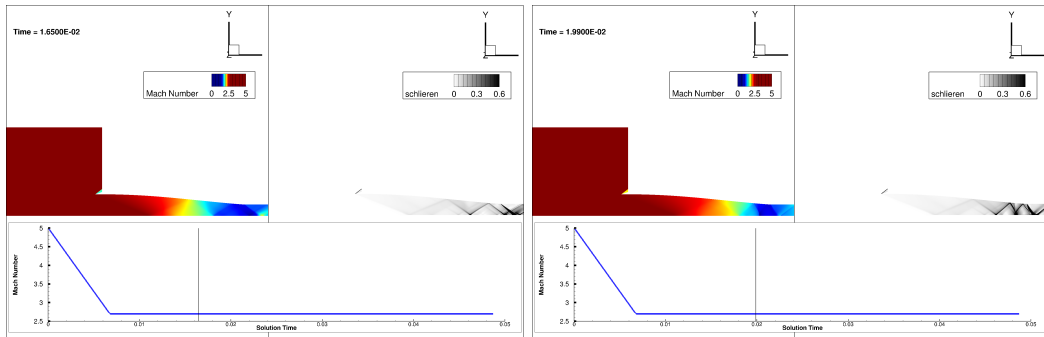
((a)) Detail of the intake flow-field at time $t = 0.0165$ s.

((b)) Detail of the intake flow-field at time $t = 0.0199$ s.

Figure 5.31: Mach number contour and Schlieren visualization, along with the time history of the inlet freestream Mach number.

From Figures 5.30(b), 5.31(a), and 5.31(b), it can be observed that the intake compression system undergoes significant changes, progressively adapting to the upstream conditions and shifting the shock waves further upstream.
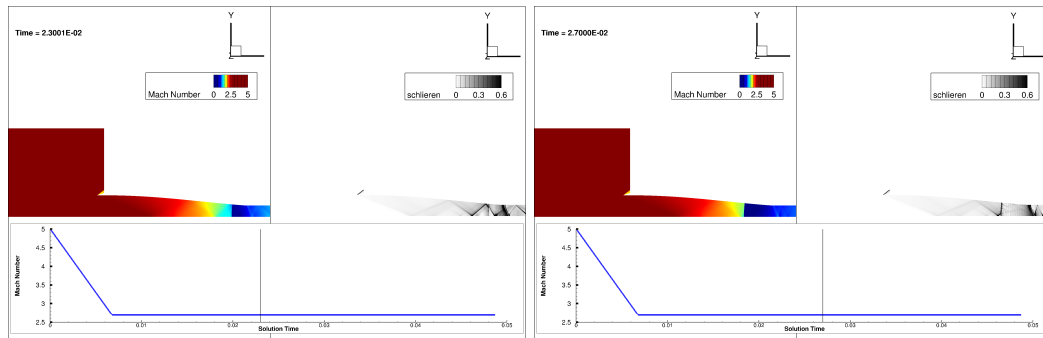
((a)) Detail of the intake flow-field at time $t = 0.0203$ s.

((b)) Detail of the intake flow-field at time $t = 0.0207$ s.

Figure 5.32: Mach number contour and Schlieren visualization, along with the time history of the inlet freestream Mach number.

In Figure 5.32(a), the formation of a normal shock wave is already evident at time $t = 0.0203$ s. This is clearly shown in the Mach number contour, where the flow downstream of the shock reaches subsonic values, a characteristic feature of a normal shock.
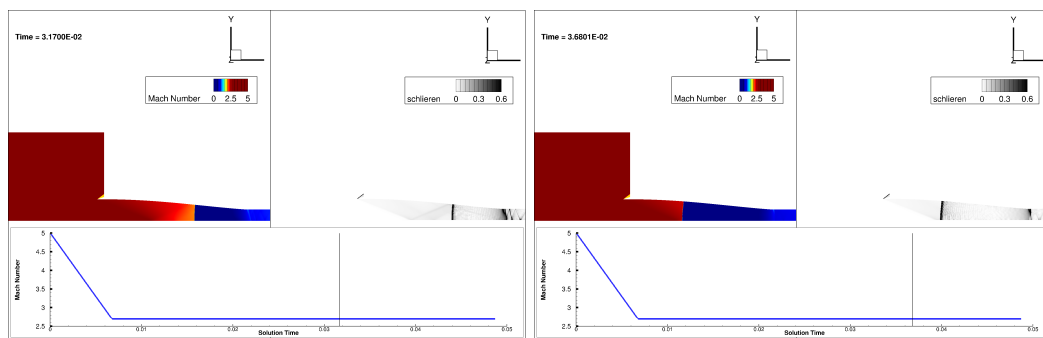
((a)) Detail of the intake flow-field at time $t = 0.0317$ s.

((b)) Detail of the intake flow-field at time $t = 0.0368$ s.

Figure 5.33: Mach number contour and Schlieren visualization, along with the time history of the inlet freestream Mach number.

99

((a)) Detail of the intake flow-field at time $t = 0.0408$ s.

((b)) Detail of the intake flow-field at time $t = 0.0437$ s.
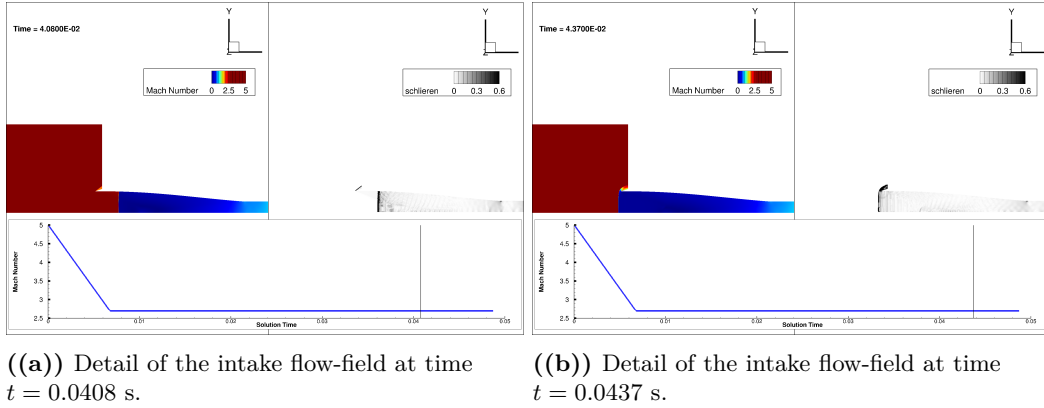
Figure 5.34: Mach number contour and Schlieren visualization, along with the time history of the inlet freestream Mach number.

Figures 5.32(b), 5.33(a), 5.33(b), 5.34(a), and 5.34(b) show the upstream propagation of the normal shock wave, ultimately leading to the complete unstart of the intake.

((a)) Detail of the intake flow-field at time $t = 0.0457$ s.

((b)) Detail of the intake flow-field at time $t = 0.0485$ s.
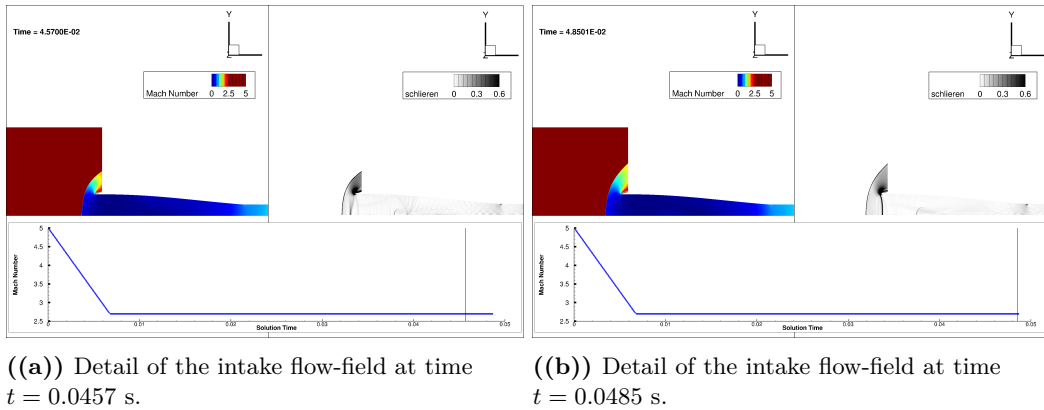
Figure 5.35: Mach number contour and Schlieren visualization, along with the time history of the inlet freestream Mach number.

Finally, Figures 5.35(a) and 5.35(b) show that the normal shock wave exits the intake and stabilizes upstream of the inlet, marking the complete unstart of the intake system after a total elapsed time of $t = 0.0485$ s.

A detailed analysis of these time steps reveals that, as the intake adjusts to lower flight conditions, the oblique shock system evolves and eventually gives rise to a normal shock. This phenomenon is primarily due to the reduced mass flow rate entering the intake. As the inflow becomes insufficient to sustain the designed compression system, the normal shock travels upstream, leading to a breakdown of the compression mechanism.

Such a condition is highly undesirable during flight operation, not only because it fundamentally disrupts the designed shock structure, but also because it severely limits the mass flow rate entering the engine, directly reducing the thrust generated by the propulsion system.

100

It is also observed that, at the outlet section, the Mach number reaches sonic conditions ($M_3 = 1$). This behavior results from the imposition of a supersonic outlet boundary condition, in which no static pressure is prescribed. In supersonic regimes, characteristic lines and flow information propagate only downstream, preventing any information from traveling toward the upstream flow. To satisfy this boundary condition, when a subsonic region is formed downstream of the normal shock, it re-accelerates to sonic conditions at the outlet ($M_3 = 1$).

5.2 3D Analysis

After gaining a comprehensive understanding of the 2D Busemann intake—including the influence of freestream Mach number, truncation angle, and the viscous contour correction—the focus is shifted to the three-dimensional modeling of the intake geometry, as described in Section 4.9.

The previous analyses provided a modified 2D contour, which serves as the basis for constructing the 3D geometry. This is achieved by revolving the 2D profile and redefining the exit section as an ellipse, rather than maintaining axisymmetry. The elliptical cross-section was chosen because it integrates more effectively with conventional airframe geometries and offers practical advantages over a purely axisymmetric design.

In particular, the elliptical outlet section—tangent to the intake's axis of symmetry—leads to a 3D streamline-traced geometry that naturally induces flow spillage, thereby reducing the risk of intake unstart.

The reference design parameters selected for the 3D model include an inlet Mach number $M_1 = 5$, a downstream Mach number $M_3 = 3$, a truncation angle $\delta = 5°$, and an elliptical exit cross-section with an axis ratio of 1:3. The total exit area was set to $4.57m^2$, to satisfy the airflow requirements of the combustion chamber for adequate thrust generation. This configuration results in an intake length of approximately $30.26m$.

The atmospheric conditions correspond to a flight altitude of 25 km, with a static pressure of 2511 Pa and a temperature of 221.55 K. The streamlines generated according to this design were imported into SolidWorks and are shown in Fig. 5.36.
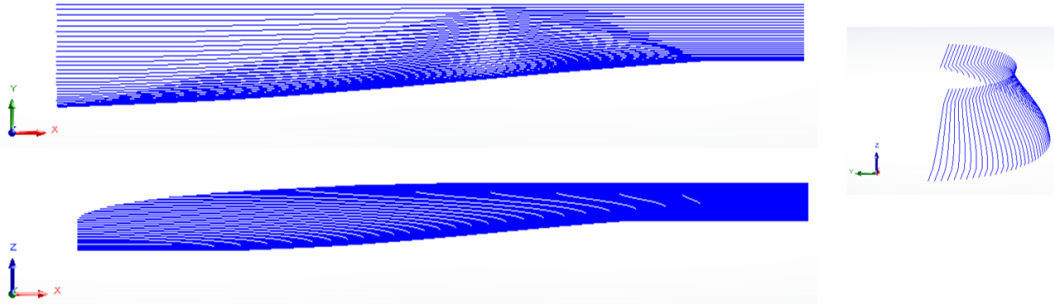
Figure 5.36: 3D Streamline imported in Solidorks for $M_1 = 5$, $M_3 = 3$, $\delta = 5°$ design.

Only half of the streamlines are imported, as the geometry is symmetric with respect to the $x - z$ plane. Additionally, due to software constraints, importing only one half of the streamline set allows for a denser distribution of curves in that region, resulting in a more accurate and refined design. This is particularly important in hypersonic applications, where even minor geometric distortions can lead to the formation of shock waves, significantly affecting intake performance.

A loft surface is then generated from the imported curves. This surface is mirrored to reconstruct the full geometry, after which a uniform wall thickness of 11.3 mm is added to create the solid intake body (see Fig. 5.37).

Furthermore, a 4-meter extension is added to the exit section to represent the beginning of the isolator. This extension allows for analysis of boundary layer development in

the region immediately upstream of the combustor, where flow uniformity is critical for combustion stability and performance.
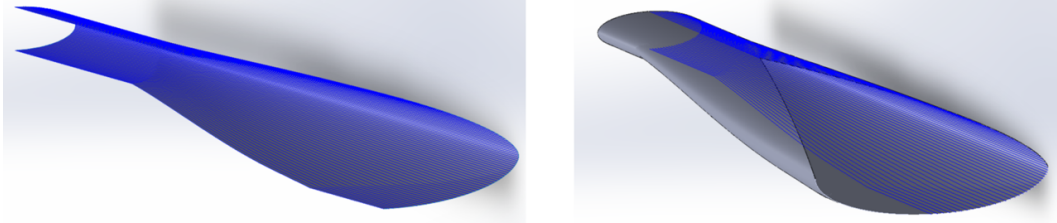
Figure 5.37: 3D Intake for $M_1 = 5$, $M_3 = 3$, $\delta = 5°$ design.

5.2.1 Mesh convergence study

Due to the complexity of the geometry under investigation, a watertight mesh approach was adopted using *Fluent Meshing*, available within the *ANSYS* software suite. This meshing technique offers improved element quality compared to traditional meshing tools, for equivalent settings of element size and inflation layers. In particular, the use of poly-hexcore elements enables both a reduction in the total number of elements and an overall increase in mesh quality. These characteristics are especially advantageous in complex geometries such as the present case, as they enhance numerical stability and improve computational efficiency.

Several mesh configurations were evaluated, and a mesh convergence study was conducted to determine the minimum mesh resolution beyond which the results become independent of discretization errors introduced by the computational grid. To accurately resolve the boundary layer, an inflation layer strategy was adopted for all mesh configurations. Specifically, the first layer thickness was set to $1 \times 10^{-5} m$, with a total of 25 inflation layers. This approach ensured adequate near-wall resolution, maintaining $y^+ < 1$ across the entire wall surface.
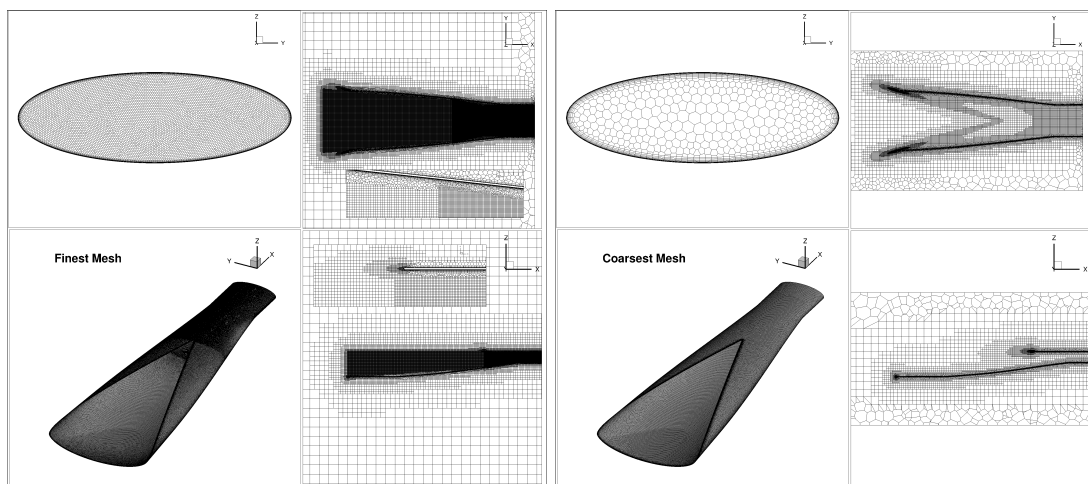
Figure 5.38: Details of finest and coarsest mesh.

103

In this study, two Body of Influence (BOI) sizing regions were implemented as part of the meshing strategy, with the goal of refining the mesh only in areas of particular interest. The first BOI was placed along the isolator region to ensure proper resolution of the shock wave, while the second was applied in the compression zone of the intake.

Figure 5.38 illustrates both mesh configurations—coarsest and finest. In the finest mesh (top and bottom left of the first four subfigures), the effect of the two BOIs is clearly visible in both the cross-sectional and axial views. In particular, the BOI around the isolator and shock wave region features a finer element sizing, while a similar refinement is observed in the area corresponding to the second BOI in the compression region.

Conversely, in the coarsest mesh configuration (also shown in Figure 5.38), the element sizing within the two BOIs is significantly larger, resulting in a mesh where localized refinement is no longer distinguishable.

To provide a preliminary qualitative comparison between these two mesh configurations, Figure 5.39 presents selected flow variables. In particular, a contour plot of total pressure is shown at the outlet section—a key metric for evaluating the intake compression efficiency and estimating pressure losses due to viscous effects. It is evident that the finer mesh yields a more accurate and less distorted representation of total pressure at the outlet compared to the coarser mesh.

In addition, Schlieren plots—based on the density gradient and commonly used to visualize shock waves—demonstrate that the finer mesh is more effective at capturing the compression field and shock structures with higher fidelity and detail. These visualizations already offer a clear qualitative distinction between the two mesh resolutions.
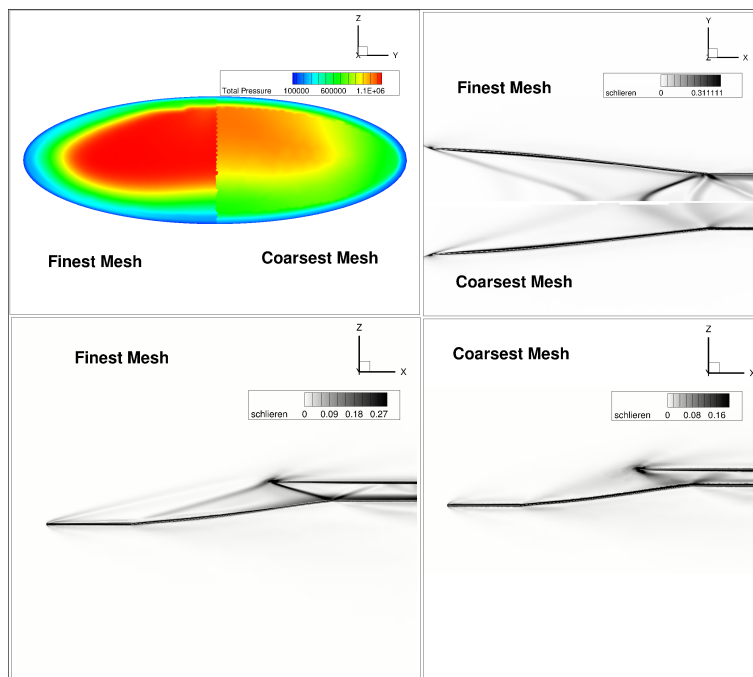
Figure 5.39: Coarsest and Finest Mesh comparison.
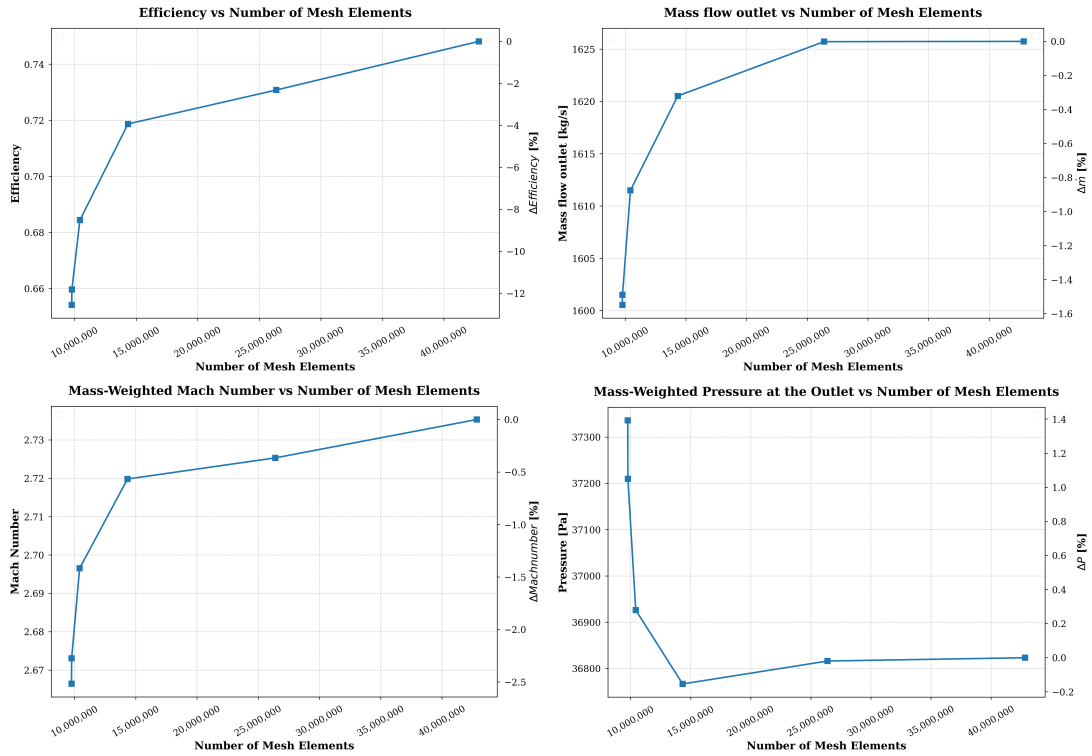
Figure 5.40: 3D mesh convergence analysis. Plots of mass flow rate, compression efficiency, and mass-weighted average of Mach number and static pressure at the outlet as a function of the total number of mesh elements.

As shown in Fig. 5.40, key parameters such as mass flow rate, compression efficiency, and the mass-weighted average values of Mach number and static pressure at the outlet are plotted as functions of the total number of mesh elements.

Although each trend exhibits a clear asymptotic behavior—indicating mesh independence—the variations in mass flow rate, Mach number, and static pressure between the coarsest and finest mesh configurations remain within a maximum deviation of approximately 2.5%. These small differences are not significant enough to favor one mesh over another solely based on these parameters.

However, a different conclusion emerges when evaluating compression efficiency. As illustrated in Fig. 5.39, efficiency is highly sensitive to how accurately the intake compression is resolved. In this case, the discrepancy between the coarsest and finest meshes exceeds 12%, highlighting a more pronounced dependence on mesh resolution.

Taking all these parameters into account—along with the computational cost associated with each mesh (see Fig. 5.41)—the fifth mesh configuration, consisting of approximately 26 million elements, was selected for the remainder of the simulations. This mesh achieves a good balance between accuracy and efficiency, requiring less than one hour to reach convergence using 150 computing cores. Since multiple simulations are required for off-design condition analyses, this configuration represents an optimal compromise between solution fidelity and computational expense.
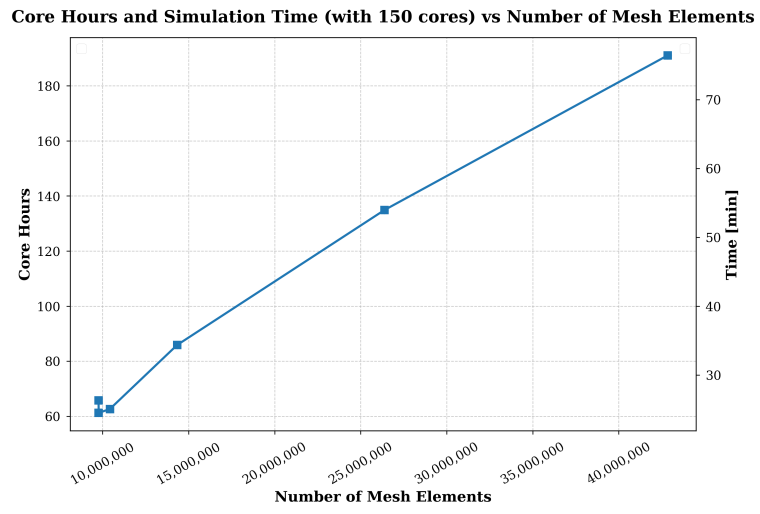
Figure 5.41: Simulation time and total core-hours required to reach convergence for each mesh configuration.

5.2.2   On Design Results
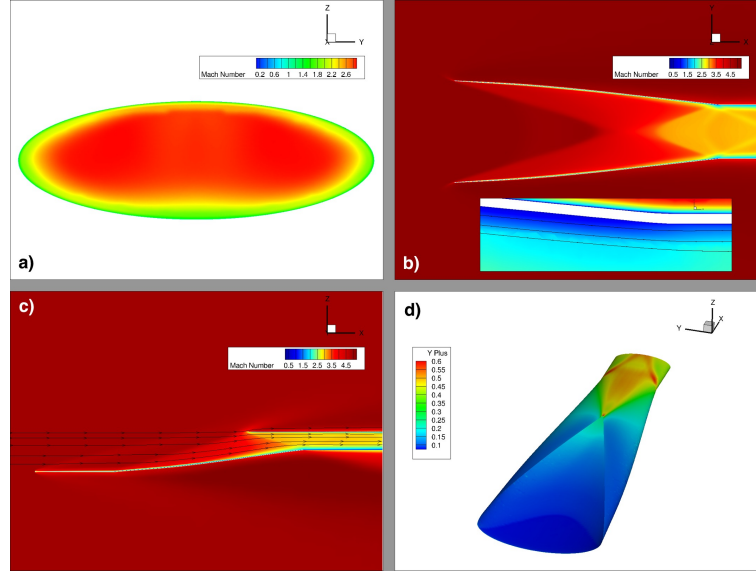
Figure 5.42: Mach number contours under on-design flow conditions, displayed at the outlet section, on a cross-sectional plane, and along the axial symmetry plane. A wall surface plot of y^+ values is included to evaluate near-wall mesh quality and boundary layer resolution.

To analyze the on-design performance of the Busemann intake, Figures 5.42 and 5.43 are examined in detail.

Figure 5.42a shows the Mach number contour at the intake outlet. A noticeable boundary layer development can be observed, which is more pronounced along the lower wall than the upper wall. This asymmetry results from the intake geometry, which features an elliptical upper contour tangent to the axis, creating a notch designed to promote mass flow spillage and reduce the risk of unstart.

Figures 5.42b and 5.42c present Mach number contours on a transverse plane and the axial symmetry plane, respectively. These plots highlight the progressive flow compression induced by the intake geometry. In particular, these Figures show the 3D shock structure impingement on the wall corner without any evidence of flow separation, as confirmed by the streamline pattern. Furthermore, the streamline behaviour near the notch indicates the presence of slight mass flow spillage even under on-design conditions. The shock-induced flow deflection, combined with the intake geometry, ensures that the flow enters the isolator nearly parallel to the intake walls.

Figure 5.42d displays the y^+ distribution on the internal wall surface of the intake. The maximum y^+ value is approximately 0.6, occurring near the shock impingement and reflection points, and remains below the critical threshold of $y^+ < 1$, thereby ensuring accurate resolution of the boundary layer.

Turning to Figure 5.43, the first three subfigures (a–c) illustrate the static pressure distribution. Figure 5.43a shows the outlet cross-section, where a higher pressure is observed along the centerline. This corresponds to the region of shock reflection, as seen

in the transverse section in Figure 5.43b. Figure 5.43c highlights the flow compression in the symmetry plane, where the initial isentropic compression is followed by a strong shock generated from the upper notch, which impinges on the lower wall and then reflects toward the outlet.

Finally, Figure 5.43d presents the total pressure ratio, which serves as a measure of the intake's compression efficiency. The most significant losses due to viscous effects are concentrated along the lower and side walls, where the boundary layer has a longer development path. In contrast, the upper wall near the notch exhibits smaller losses due to the reduced surface area available for boundary layer growth. In the central core region, the total pressure recovery is relatively uniform, with values around 0.96. This indicates that the dominant losses in this area are attributable to shock waves, confirming the effectiveness of the shock-based compression system.
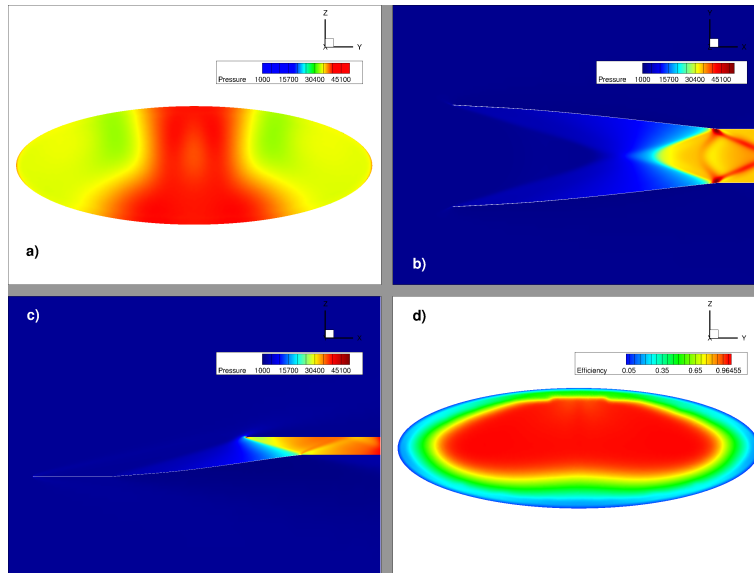
Figure 5.43: Pressure contour plots under on-design flow conditions, shown at the outlet section, on a transverse plane, and along the axial symmetry plane. The total pressure ratio is computed at the outlet to assess the intake's compression efficiency.

By examining the mass-weighted average values reported in Table 5.5, the increased complexity of the intake in the 3D case becomes evident when compared to the simpler 2D configuration previously analyzed. Notably, the average efficiency at the outlet decreases to approximately 0.73 in the 3D case, whereas in the 2D viscous simulation it reached values as high as 0.87. This reduction highlights both the geometric and physical complexity of the 3D intake, as well as the compromises introduced by modifying the intake cross-section. Specifically, the shape is no longer axisymmetric but elliptical, a change that led to increased total pressure losses and a stronger compression. This is evidenced by a higher static pressure and a lower Mach number at the outlet, compared to the ideal design condition with a downstream Mach number of $M_3 = 3$.

Mach Number	Static Pressure	Mass-flow rate	Efficiency
[-]	[Pa]	[kg/s]	[-]
2.72	36816	1625	0.7307

Table 5.5: Mass-weighted averages of key flow parameters—mass flow rate, static pressure, Mach number, and intake efficiency—evaluated at the outlet section.

5.2.3 Test Matrix

The previous subsection analyzed the intake performance under on-design conditions, considering a freestream Mach number of $M_\infty = 5$ and a flow direction aligned with the intake axis. The present analysis focuses on off-design conditions, introducing variations in the angle of attack α and the sideslip angle β. Furthermore, different values of freestream Mach number M_∞ are considered to assess intake behavior and to investigate the onset of the unstart phenomenon under non-ideal operating scenarios.
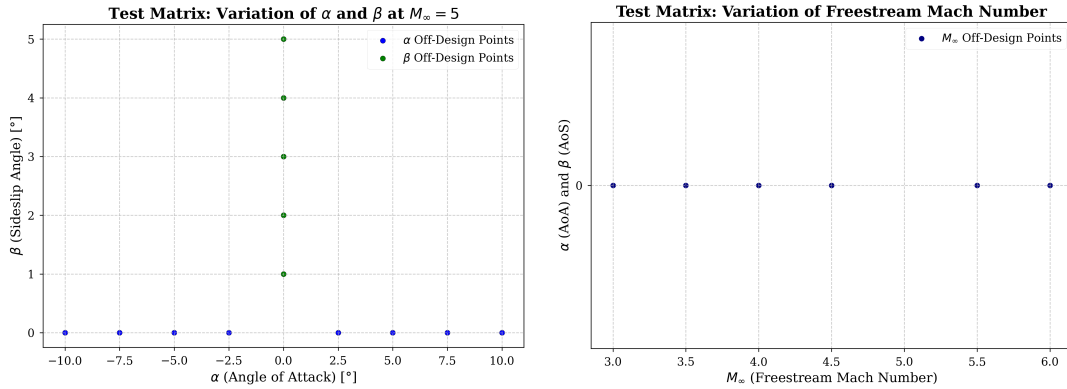
Figure 5.44: Definition of the 19 off-design test conditions considered for the parametric study, including variations in angle of attack, sideslip angle, and freestream Mach number.

Additionally, five alternative intake designs are considered to further assess design robustness and flow uniformity. The first set of variations involves modifying the downstream Mach number of the ideal contour, with cases corresponding to $M_3 = 2.5$, 3, 3.5. The second set explores the effect of varying the ellipse aspect ratio of $1{:}2$, $1{:}3$, and $1{:}4$.

Regarding the simulation setup for the various analyses, due to the high number of cases to be evaluated, a simulation is considered converged when key output variables—such as mass flow rate, outlet Mach number, static pressure, and efficiency—reach a residual threshold of 1×10^{-4}. Specifically, convergence is assumed when these quantities remain stable within this tolerance over the course of 100 iterations.

To accelerate convergence when varying boundary conditions (e.g., angle of attack or freestream Mach number), a sequential initialization strategy is adopted. Each new simulation is initialized using the converged solution from the preceding case. For instance, the simulation at $\alpha = 5°$ is initialized using the solution from the converged case at $\alpha = 2.5°$, thereby improving convergence speed.

109

To prevent the solver from prematurely identifying a case as converged, the convergence criteria are temporarily disabled for the first 200 iterations. This allows the outlet region sufficient time to adjust to the new boundary conditions before residual monitoring resumes.

5.2.4   Effect of Angle of Attack (α) Variation — $M_3 = 3$ Baseline Design
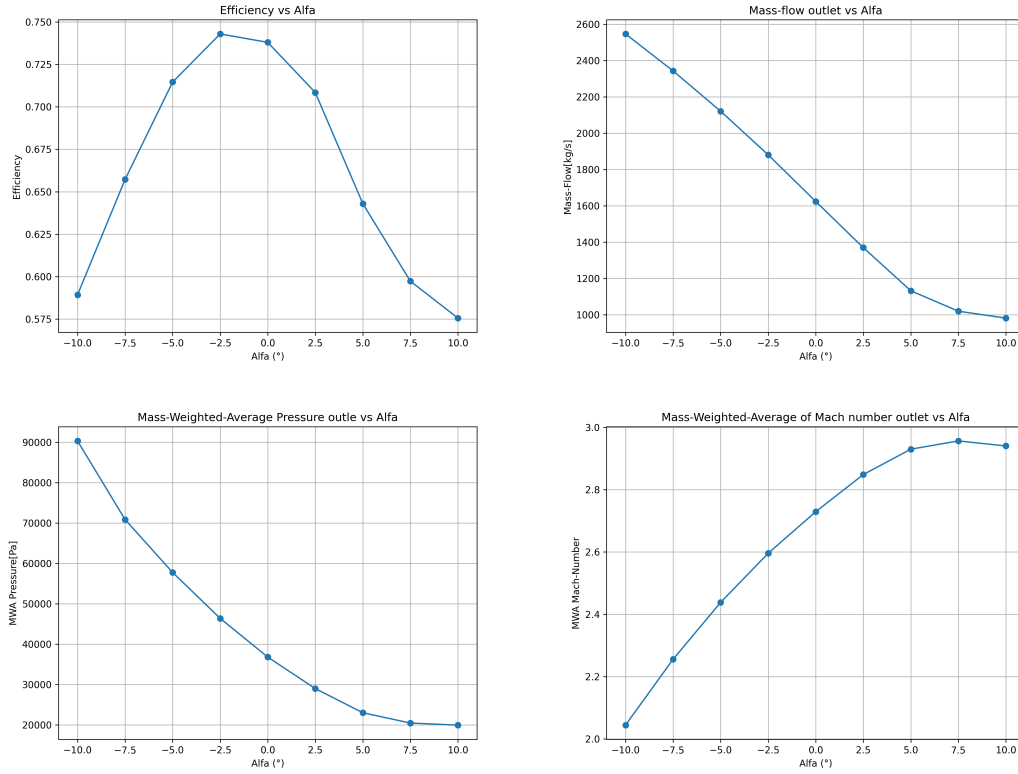
Figure 5.45: Effect of angle of attack (α) variation on the mass-weighted average values of Mach number, static pressure, compression efficiency, and mass flow rate at the outlet.

A preliminary assessment of intake performance as a function of angle of attack is shown in Figure 5.45. It can be observed that, in general, increasing or decreasing the angle of attack from the on-design condition ($\alpha = 0°$) leads to a deterioration in performance. An exception is found at $\alpha = -2.5°$, where a slight increase in compression efficiency is observed.

The trend in mass flow rate with respect to angle of attack reveals that negative angles result in an increase in mass flow rate, while positive angles lead to a decrease. This behavior can be attributed to changes in the effective capture area, given that the freestream Mach number is held constant. For negative angles of attack, the capture area increases, whereas for positive angles, it decreases. This is primarily due to the intake geometry, which features an opening in the upper region. When the intake is inclined downward (negative α), this upper opening becomes more exposed to the incoming flow, effectively enlarging the apparent intake area. This geometric effect is illustrated in Figures 5.46, 5.47 and 5.48.

111
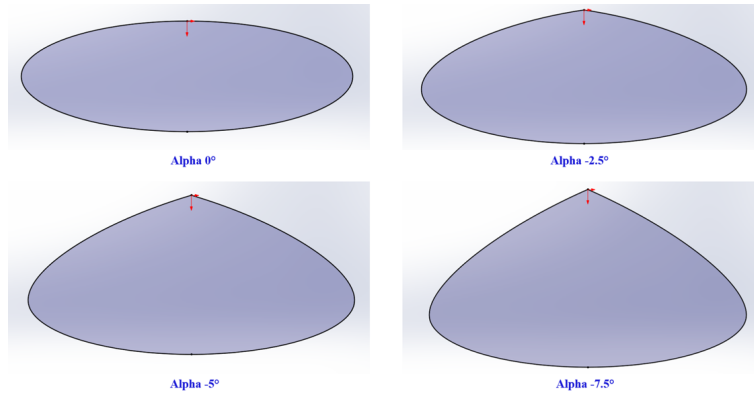
Figure 5.46: Effect of negative angle of attack on the intake capture area.
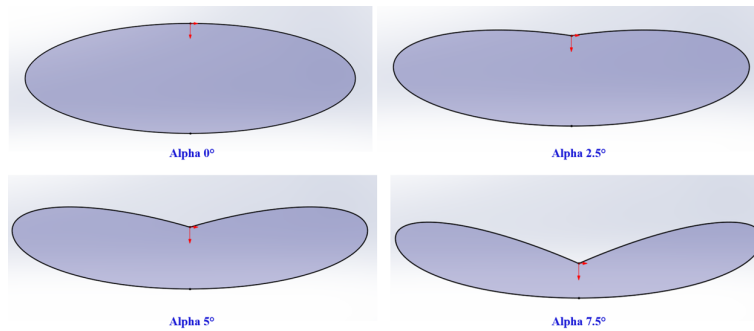
Figure 5.47: Effect of positive angle of attack on the intake capture area.
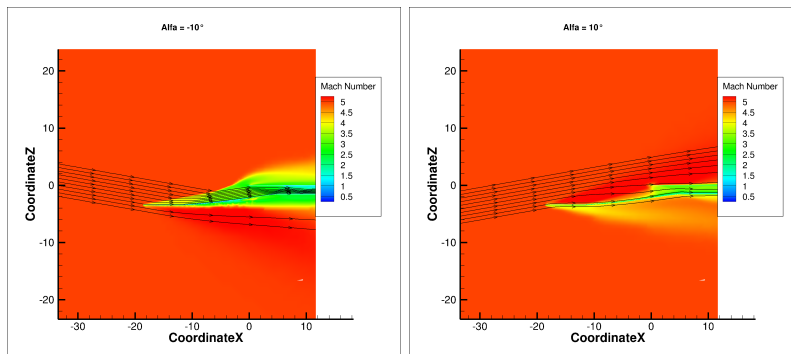
Figure 5.48: Mach number contours along the intake symmetry plane for $\alpha = 10°$ and $\alpha = -10°$, illustrating the velocity streamlines.

Continuing the analysis of performance parameters in Figure 5.45, it can be observed that, in addition to the variation in mass flow rate with angle of attack, both static pressure and Mach number exhibit similar trends. Specifically, for negative angles of attack—where a larger amount of air is captured by the intake—the flow undergoes greater compression, as evidenced by the increase in outlet static pressure, and experiences

a stronger deceleration, as shown by the reduction in Mach number. Conversely, at positive angles of attack—where the effective capture area is reduced—the intake captures less air, resulting in lower compression and less deceleration of the flow.

A comparison of the flow-field structures for the two extreme cases, $\alpha = 10°$ and $\alpha = -10°$, is presented in Figures 5.49. The Schlieren contours reveal that, for positive angles of attack, the compression system remains largely similar to that of the on-design case. In contrast, negative angles of attack significantly alter the compression structure. Due to the increased amount of air captured, the configuration at negative α results in a forward displacement of the shock system, bypassing the isentropic compression region at the intake's entrance. This behavior explains the increase in outlet pressure observed for such conditions.

Regarding the outlet section, the Mach number contours show that positive angles of attack maintain a similar flow structure to the on-design case, including the presence of vortices near the lateral walls. On the other hand, at negative angles, the outlet flow structure changes considerably, with the formation of vortices along the centerline, consistent with the altered flow pattern observed in the transverse plane.

Despite the significant flow modifications observed, it is important to highlight that the intake does not exhibit the unstart phenomenon, even under negative angles of attack. This result is particularly relevant, as operating at negative α values plays a crucial role in scenarios where the intake has become unstarted. In such cases, the vehicle must adopt a negative angle of attack to maximize the captured airflow and promote re-starting of the intake as quickly as possible. Therefore, the intake's ability to maintain attached flow and avoid unstart under these off-design conditions represents a key advantage in terms of operational stability and recovery strategies.
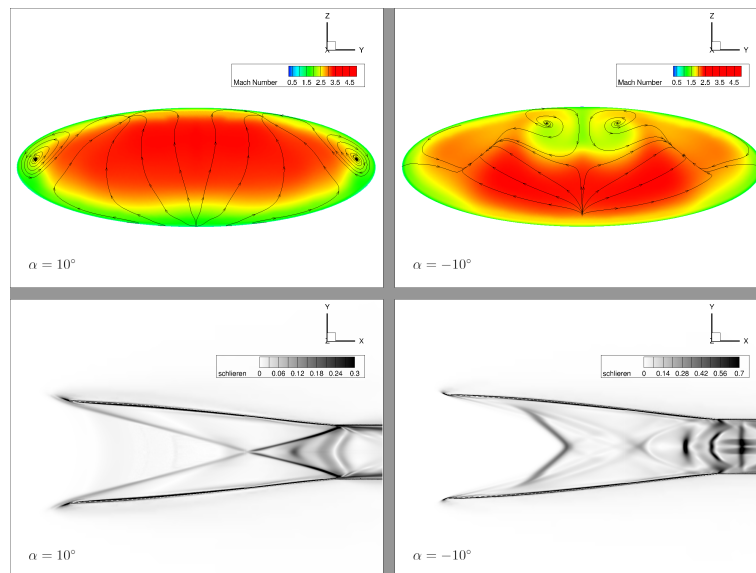
Figure 5.49: Comparison of flow-field structures for $\alpha = 10°$ and $\alpha = -10°$, showing Schlieren contours on the transverse plane and Mach number contours at the outlet section.

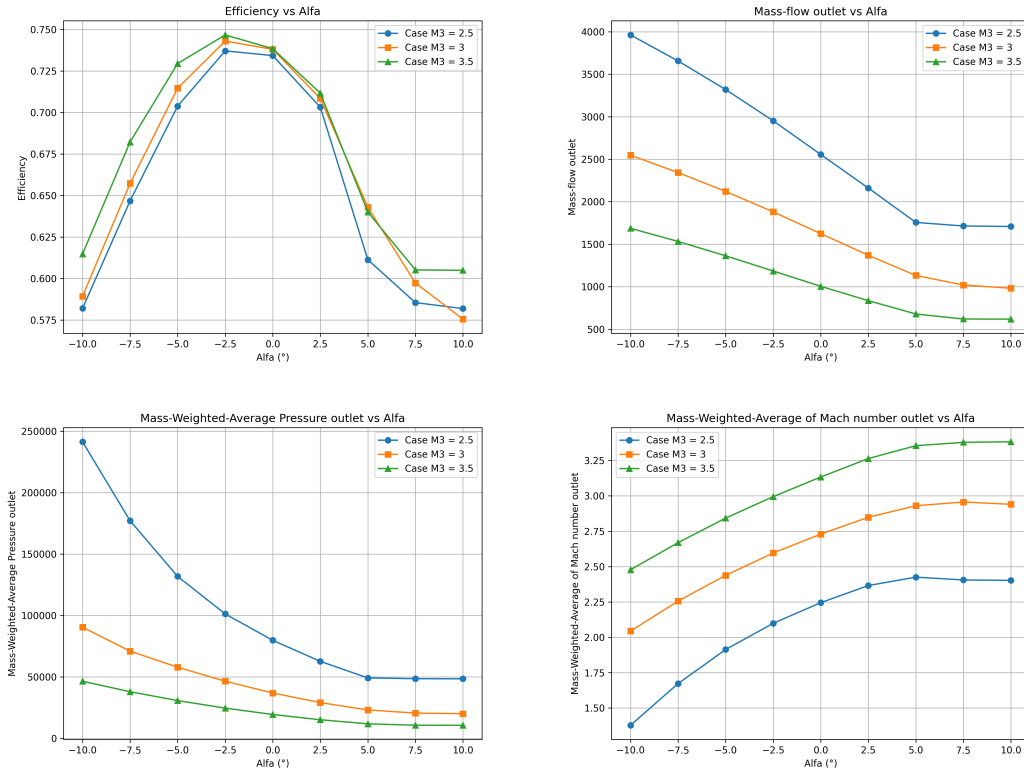### 5.2.5 Effect of Sideslip Angle (β) Variation — $M_3 = 3$ Baseline Design
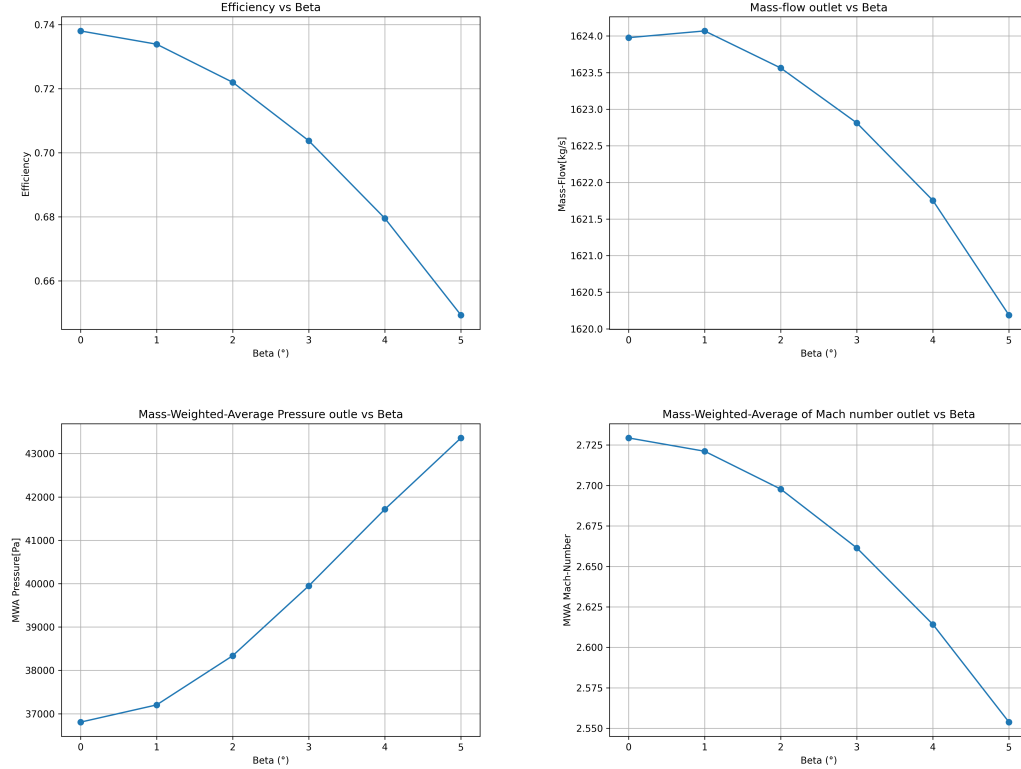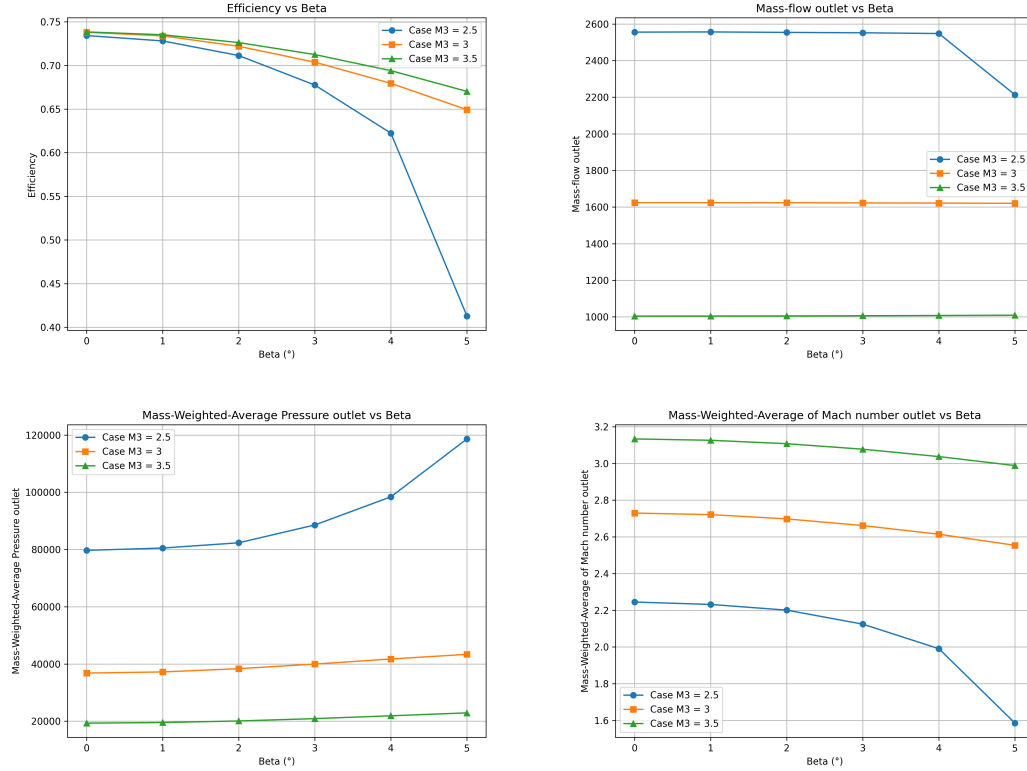

Figure 5.50: Effect of angle of sideslip (β) variation on the mass-weighted average values of Mach number, static pressure, compression efficiency, and mass flow rate at the outlet.

The influence of sideslip angle (β) variation on intake performance is presented in Figure 5.50, where trends of mass flow rate, efficiency, and the mass-weighted average values of Mach number and static pressure at the outlet are reported.

Only positive values of β are considered, as the intake geometry is symmetric with respect to the *x-z* plane. Consequently, negative sideslip angles would produce mirrored, and thus equivalent, results due to the symmetry of the configuration.

It is immediately evident that, unlike angle of attack variations, the mass flow rate remains nearly constant with increasing sideslip angle. This suggests that the effective capture area is not significantly affected by β, in contrast to its strong sensitivity to α variations.

However, other performance parameters show notable variations. In particular, an increase in β leads to a degradation of overall performance and an increase in flow compression. This is reflected in the rise of static pressure at the outlet and the decrease in Mach number, indicating a stronger deceleration of the flow. These observations imply a modification of the shock structure and compression pattern compared to the on-design condition.

114
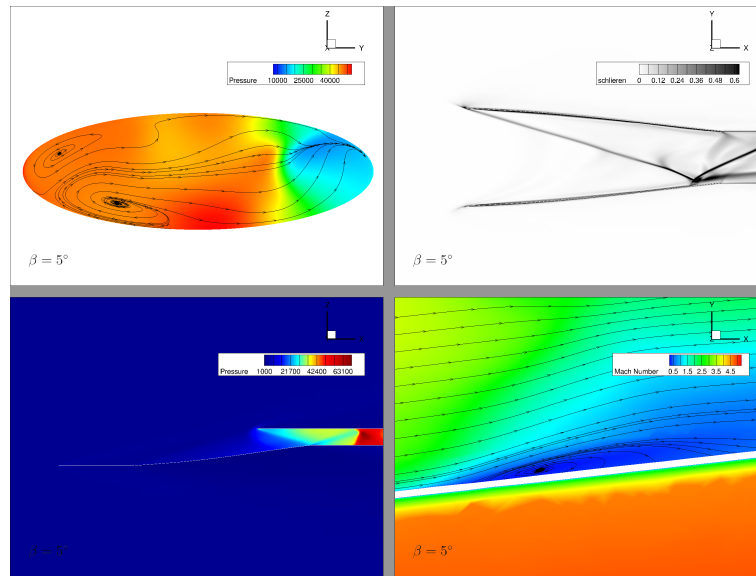
Figure 5.51: Comparison of flow-field structures for $\beta = 5°$, including Schlieren contours on the transverse plane and static pressure distributions at the outlet and along the symmetry plane.

As shown in Figure 5.51, the compression structure changes significantly under sideslip conditions. In particular, the Schlieren visualization on the transverse plane (top right) reveals the loss of the isentropic compression pattern observed in the on-design case. Instead, an oblique shock forms and impinges on the lower wall. In the zoomed view (bottom right), focusing on the shock impingement region, a strong interaction between the shock wave and the boundary layer can be observed. This interaction leads to boundary layer separation and the formation of vortices, as highlighted by the streamlines. These features contribute to a loss in total pressure and, consequently, efficiency.

In the top-left image, the static pressure contour at the outlet shows a markedly different structure compared to the on-design configuration. The flow appears more compressed on the left-hand side of the outlet, and vortical structures are again present, negatively affecting flow uniformity at the exit.

The bottom-left image, showing the symmetry plane, indicates a sudden pressure rise near the end of the isolator, likely caused by the reflection of the wall-bounded shock wave.

Despite these significant changes in the internal flow structure, it is important to note that the intake does not experience unstart. This suggests that for small sideslip angles, the intake remains stable and functional. Given the high-speed flight conditions typical of this engine configuration, where large sideslip maneuvers are uncommon, this result is particularly relevant. It confirms that the intake design can tolerate small deviations in β without flow breakdown, maintaining operational robustness.

5.2.6 Effect of Freestream Mach Number (M_∞) Variation — $M_3 = 3$ Baseline Design
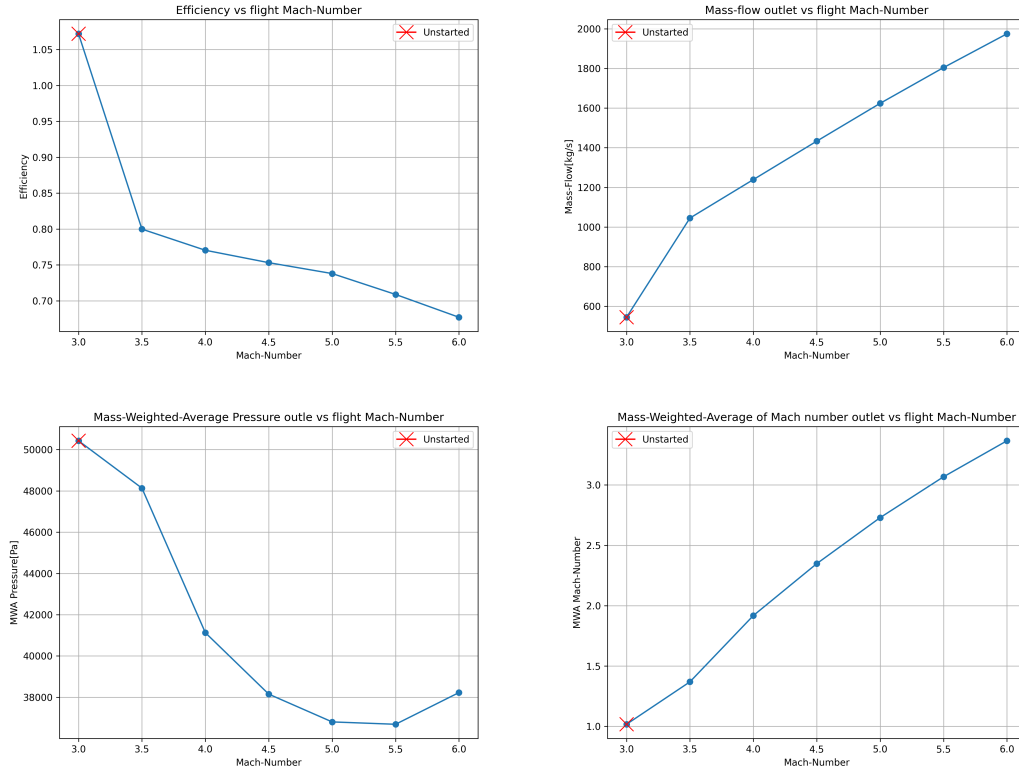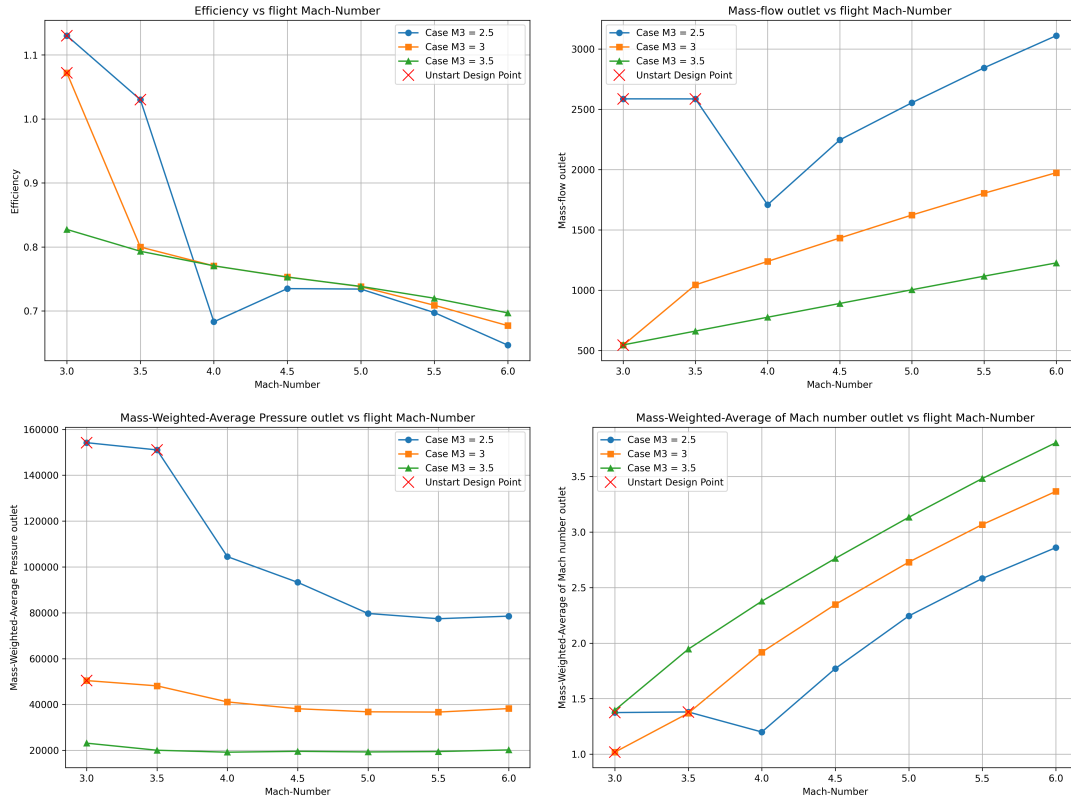

Figure 5.52: Effect of flight Mach Number (M_∞) variation on the mass-weighted average values of Mach number, static pressure, compression efficiency, and mass flow rate at the outlet.

Figure 5.52 presents the effects of varying the freestream Mach number on key performance parameters, namely the mass flow rate, compression efficiency, and the mass-weighted average values of Mach number and static pressure at the outlet.

The first notable observation is that, as the flight Mach number decreases to $M_\infty = 3$, the intake exhibits an unstarted configuration. This behavior is primarily due to the specific geometry of the intake and the area ratio between the inlet and outlet in the studied design.

The mass flow rate shows an approximately linear trend with respect to the flight Mach number: as the Mach number increases, more air is ingested by the intake, and vice versa. This aligns with physical expectations. Regarding the static pressure, it is observed that higher flight Mach numbers do not significantly alter the compression system. According to shock wave theory, as the Mach number increases, the shock angle becomes more oblique, allowing the shock to extend further downstream, which results in some of the incoming air entering the intake without being compressed, as it can be seen in Fig 5.54. Despite this, the increased velocity results in greater compression, which also

116

leads to higher total pressure losses, as reflected by a decrease in compression efficiency.

At lower flight Mach numbers, the flow experiences an overboard spillage phenomenon, wherein the percentage of captured mass is reduced. This is due to the fact that, at lower Mach numbers and fixed geometry, the shock wave becomes less inclined and deflects the flow more strongly, thereby reducing the effective capture area. Nevertheless, a higher efficiency is observed at these lower Mach numbers. This indicates that the total pressure losses are smaller in this regime, and that the intake—processing a lower mass flow—compresses it more effectively, which explains the rise in outlet pressure.

The efficiency value at $M_\infty = 3$ should not be considered physically meaningful, as an efficiency greater than one is not realistic. This artifact results from the fact that, when the inlet Mach number is reduced from 3.5 to 3, the intake becomes unstarted and the shock wave moves outside the intake. Consequently, the simulation diverges numerically due to the increased complexity of the unstarted configuration. In this condition, the outlet flow does not respond consistently to changes in the inlet conditions. In particular, assuming a constant outlet total pressure p_{t_3}, a reduction in M_∞ leads to a lower inlet total pressure p_{t_∞}. Since efficiency is defined as the ratio p_{t_3}/p_{t_∞}, the result may erroneously suggest that $p_{t_3} > p_{t_\infty}$, which violates physical principles and confirms the presence of numerical divergence. This explains the non-physical efficiency value greater than one.
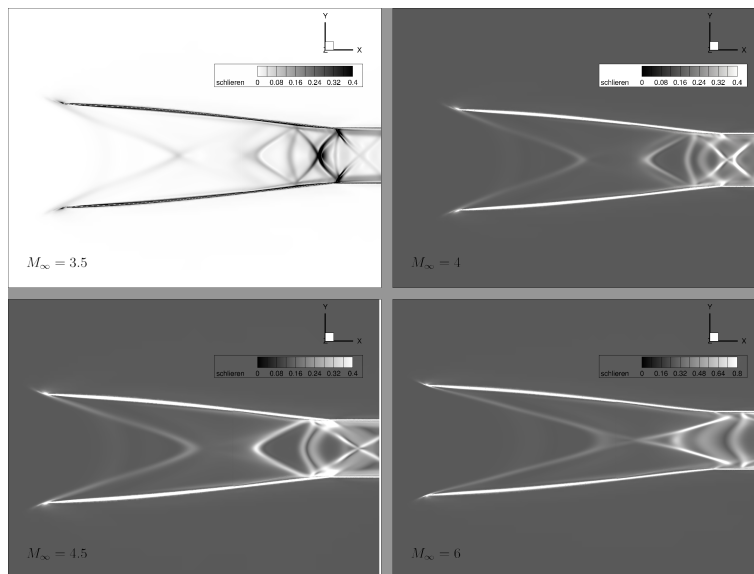
Figure 5.53: Schlieren contours illustrating the evolution of the compression shock structure for different freestream Mach numbers.

The Schlieren visualizations in Figure 5.53 illustrate how the shock wave structure evolves with different freestream Mach numbers. Specifically, it can be observed that as the Mach number decreases (e.g., $M_\infty = 4.5$, 4.0, and 3.5), the shock waves tend to move upstream and widen, due to the increased amount of spillage occurring at lower speeds.

In contrast, at higher freestream Mach numbers (e.g., $M_\infty = 6$), the shock system

appears more elongated and shifts downstream along the intake. This behavior is consistent with shock wave theory, which predicts that as the Mach number increases, shock waves become more oblique and are deflected further downstream.
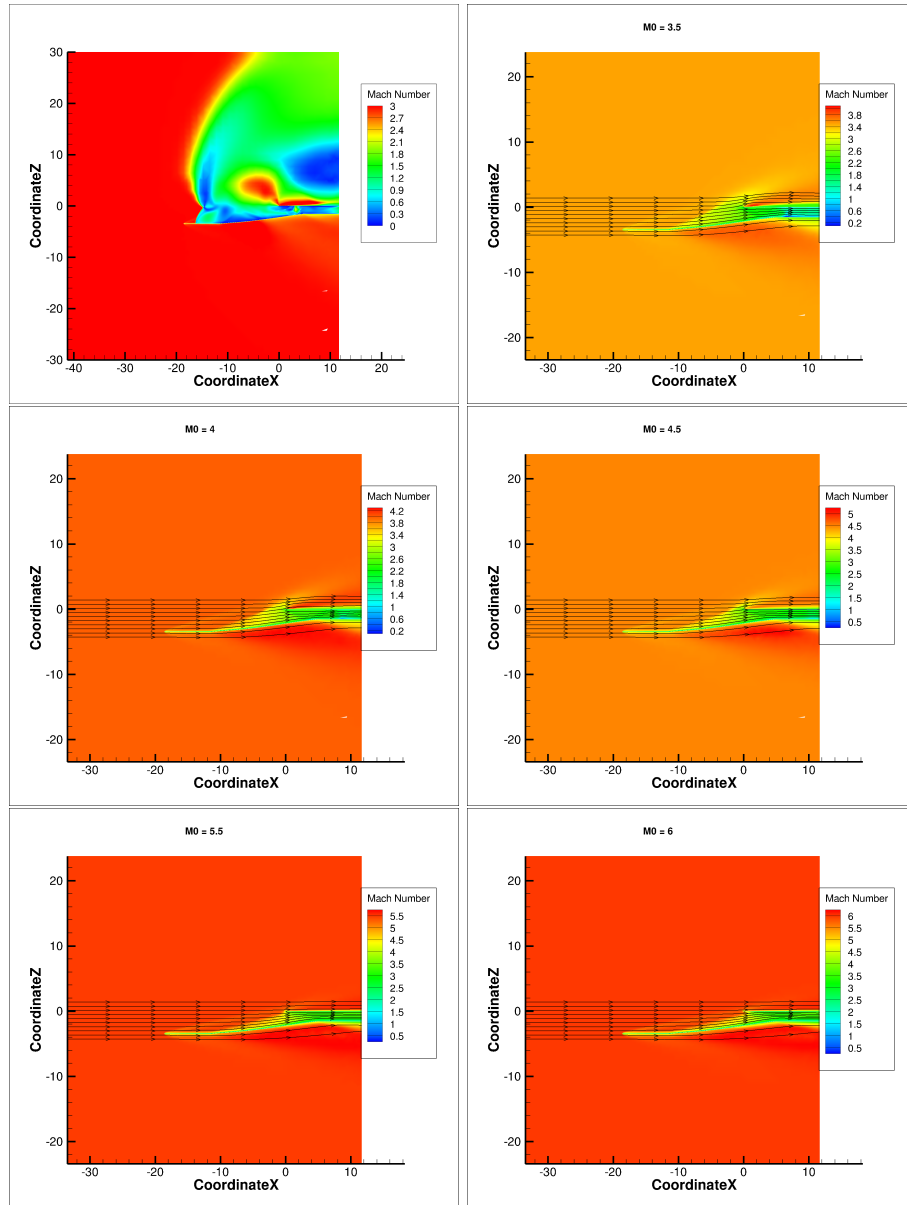
Figure 5.54: Mach number contours along the symmetry plane for different freestream Mach numbers. Velocity streamlines are also shown to highlight the overboard spillage phenomenon occurring at lower Mach numbers.

5.2.7 Comparison of Intake Designs with Varying Downstream Mach Number (M_3)

After analyzing how the flow field evolves with variations in angle of attack (α), sideslip angle (β), and freestream Mach number (M_∞), attention is now turned to a comparison between different intake designs. This comparison focuses on the effect of varying the downstream Mach number (M_3), which directly influences the level of flow compression achieved by the intake.
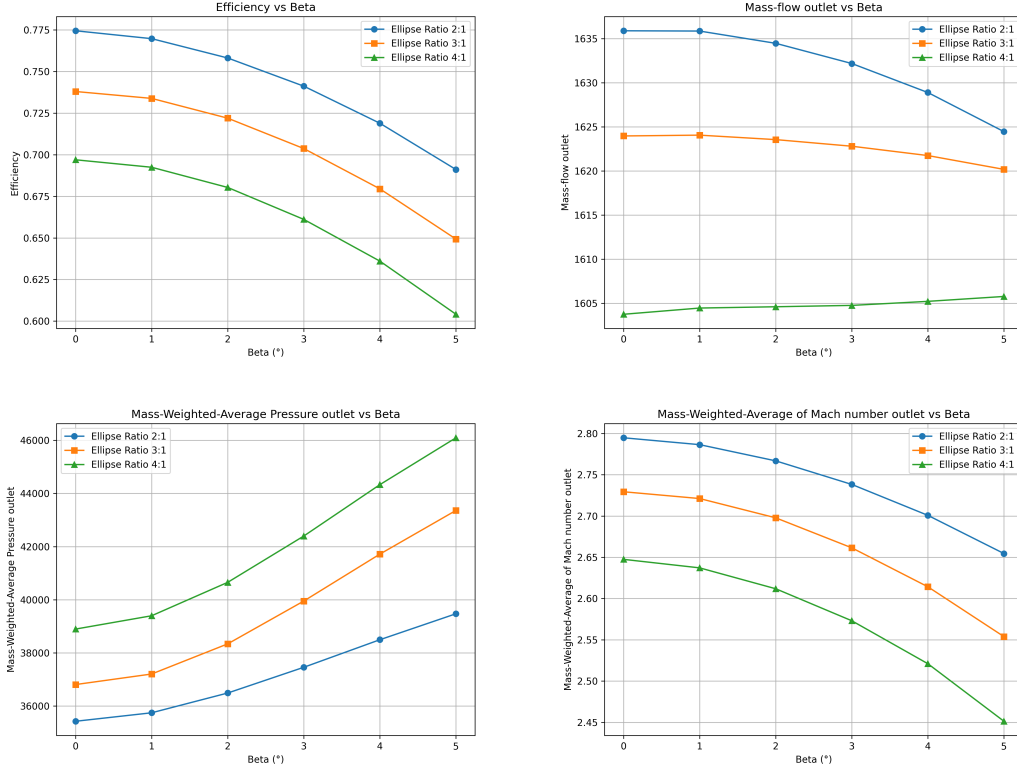

Figure 5.55: Effect of angle of attack (α) variation on the mass-weighted average values of Mach number, static pressure, compression efficiency, and mass flow rate at the outlet for $M_3 = 2.5, 3, 3.5$ design.

Figure 5.55 shows the variation of mass-weighted average Mach number, static pressure, efficiency, and mass flow rate at the outlet as a function of the angle of attack α for the three intake designs corresponding to $M_3 = 2.5, 3.0,$ and 3.5.

It is immediately evident that all curves follow similar trends, and thus the considerations made for the on-design case in Section 5.2.4 remain valid. However, it can be observed that the intake designed for $M_3 = 3.5$ exhibits higher efficiency compared to the other two configurations. Since this design is intended to compress the flow less, it experiences lower total pressure losses across the shock system. This is confirmed by the Mach number plot, where the $M_3 = 3.5$ design shows a higher outlet Mach number, consistent

with its intended design. Likewise, the static pressure plot is coherent with this behavior: less flow deceleration leads to lower compression and consequently a lower static pressure compared to the other two intakes, which are designed for stronger compression.

Particular attention should be given to the mass flow rate plot, where the behavior differs from the other parameters. As detailed in Section 4.4, when solving the Taylor–Maccoll equations and implementing the design algorithm in MATLAB, the intake geometry was defined by prescribing the inlet Mach number M_1, the target outlet Mach number M_3, and the outlet radius r_3. This implies that all three intake designs share the same outlet area, while the inlet area varies. In particular, the intake with $M_3 = 2.5$, being designed to compress the flow more, requires a lower area ratio A_3/A_i. Therefore, for a fixed outlet area A_3, the corresponding inlet area A_i must be larger. This explains the observed differences in mass flow rate between the three configurations: $A_{i_{M3.5}} < A_{i_{M3.0}} < A_{i_{M2.5}}$. As the inlet area increases—under the same inlet Mach number—the intake captures a larger mass flow.

Figure 5.56: Effect of angle of sideslip (β) variation on the mass-weighted average values of Mach number, static pressure, compression efficiency, and mass flow rate at the outlet for $M_3 = 2.5, 3, 3.5$ design.

Figure 5.56 shows the variation of mass-weighted average Mach number, static pressure, compression efficiency, and mass flow rate at the outlet as a function of the sideslip angle β for the three intake designs corresponding to $M_3 = 2.5, 3.0,$ and 3.5.

The observed trends are consistent with the results discussed in Section 5.2.5, as well as with the considerations made previously regarding the influence of α on mass flow rate. In particular, similar behavior is seen in how the mass flow rate varies with the intake geometry and design Mach number.

However, a noteworthy distinction arises for the intake designed with $M_3 = 2.5$, which exhibits significantly different behavior at sideslip angles approaching $\beta = 5°$. Specifically, this configuration shows a sudden drop in efficiency, a reduction in mass flow rate, an increase in outlet static pressure, and a stronger deceleration of the flow. These characteristics suggest that the $M_3 = 2.5$ intake is more sensitive to off-design conditions involving lateral inflow components compared to the other two designs.
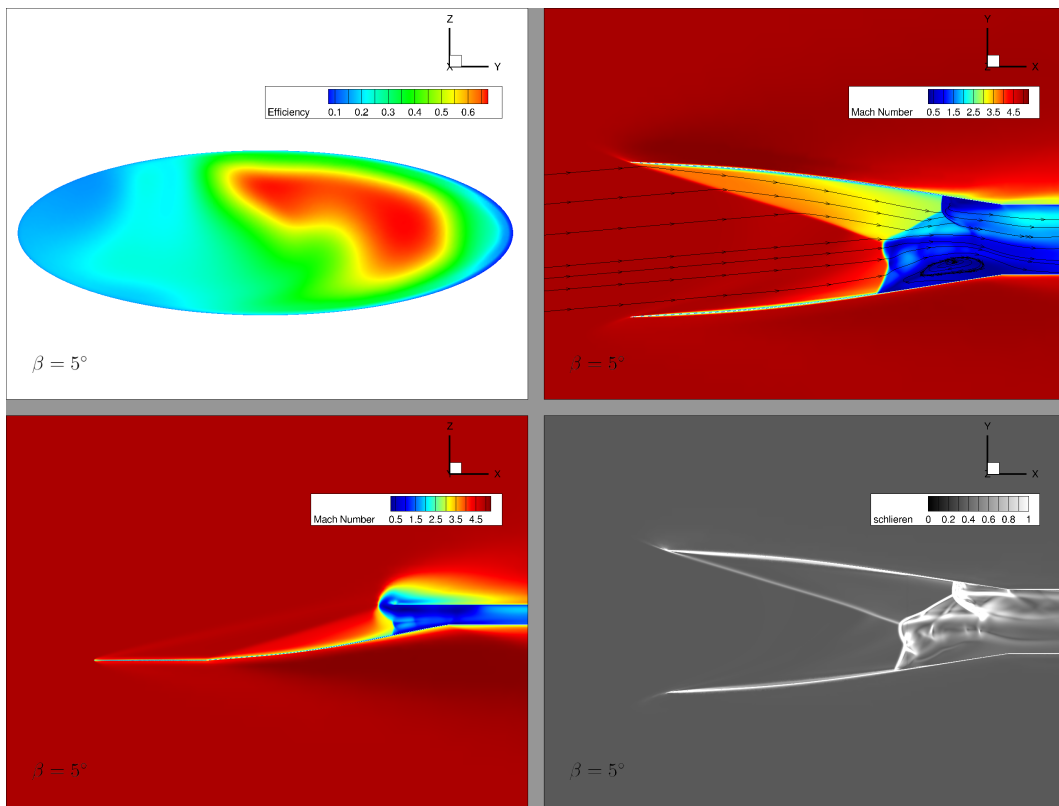
Figure 5.57: Intake Design $M_3 = 2.5$ unstarted at $\beta = 5°$.

Figure 5.57 illustrates that this particular intake design is significantly more sensitive to variations in sideslip angle β compared to the other two configurations. In fact, even small deviations, such as $\beta = 5°$, are sufficient to induce unstart in this intake. The corresponding simulation did not reach convergence, as the shock system could not stabilize within the internal geometry. Instead, the shock propagates outside the intake, ultimately causing flow separation and complete unstart of the intake.

121

Figure 5.58: Effect of flight Mach number (M_∞) variation on the mass-weighted average values of Mach number, static pressure, compression efficiency, and mass flow rate at the outlet for $M_3 = 2.5, 3, 3.5$ design.

Also in this case, the same considerations discussed in Section 5.2.6 apply. It is particularly important to highlight that the intake designed for $M_3 = 2.5$ exhibits an earlier unstart compared to the $M_3 = 3$ configuration. Specifically, it loses its started condition already at $M_\infty = 3.5$, as the internal shock system is no longer stable and moves outside the intake, rendering the configuration highly sensitive not only to the sideslip angle β but also to variations in freestream Mach number. This sensitivity makes the $M_3 = 2.5$ intake less suitable for off-design operation.

On the other hand, a noteworthy result is that the intake designed for $M_3 = 3.5$ remains started even at $M_\infty = 3.0$, unlike the other two configurations which experience unstart under the same condition. As shown in Figure 5.59, this intake maintains all flow characteristics typical of a stable, started condition. Due to its larger area ratio, the $M_3 = 3.5$ intake can more effectively handle lower freestream Mach numbers, making it more robust in off-design conditions.

However, it is important to note that this increased robustness comes at the cost of reduced compression. The $M_3 = 3.5$ intake compresses the flow significantly less than the other two designs. Therefore, a trade-off must be considered between achieving the required level of compression—dictated by combustion chamber requirements—and ensuring robustness of the intake across a range of flight conditions.
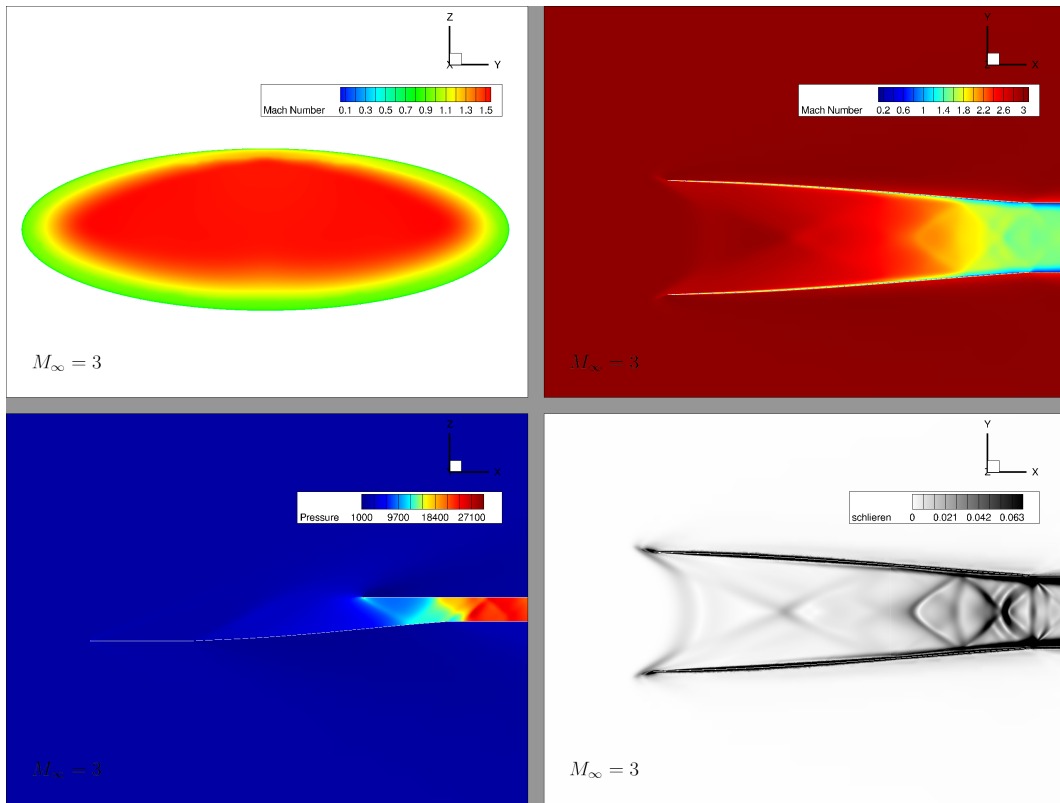
Figure 5.59: Intake Design $M_3 = 3.5$ remain started at $M_\infty = 3$ condition.

5.2.8 Comparison of Intake Designs with Different Ellipse Aspect Ratios

After identifying potential criticalities arising from variations in flight conditions, and having examined in detail several intake designs with different compression characteristics, the next step is to investigate how the shape of the outlet cross-section influences flow uniformity and the performance parameters previously analyzed. In particular, this section aims to assess how varying the outlet geometry affects key quantities such as mass flow rate, static pressure, Mach number, and overall efficiency.
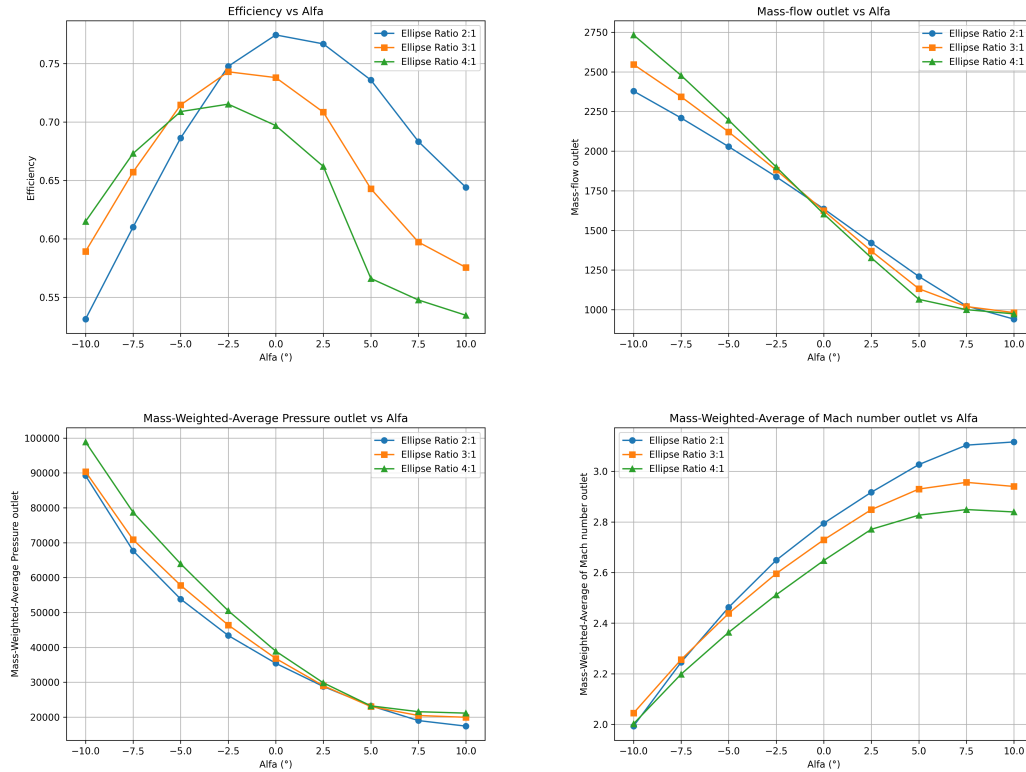
Figure 5.60: Effect of angle of attack (α) variation on the mass-weighted average values of Mach number, static pressure, compression efficiency, and mass flow rate at the outlet for different ellipse ratio design.

Figure 5.60 shows the variation of mass-weighted average Mach number, static pressure, efficiency, and mass flow rate at the outlet as a function of the angle of attack α for three intake designs characterized by ellipse ratios of 2:1, 3:1, and 4:1.

From the plots, it is immediately evident that a lower ellipse ratio—i.e., a geometry closer to a circular cross-section—results in higher efficiency under on-design conditions, as observed at $\alpha = 0°$. This trend can be attributed to the assumptions made during the 2D design phase, where an axisymmetric intake geometry was considered. Consequently, the closer the geometry approaches axisymmetry, the more its performance tends to

align with that of the 2D reference case. Conversely, increasing the ellipse ratio (i.e., more flattened cross-sections) leads to a departure from the axisymmetric assumption, which results in reduced efficiency.

This behavior is further confirmed by the Mach number contours in Figure 5.61(a), where it is observed that more flattened ellipse shapes develop a thicker boundary layer along the lower wall. On the other hand, more regular (closer to circular) cross-sections demonstrate improved total pressure recovery and better flow uniformity, as highlighted by the outlet efficiency contours.

Interestingly, the trend reverses slightly for negative angles of attack ($\alpha < 0$): in this off-design condition, the intake with the more flattened ellipse shows slightly higher efficiency compared to the circular-like configuration. As shown in Figure 5.61(b), despite the greater flow non-uniformity and the formation of vortical structures in the upper region of the intake for higher ellipse ratios, the efficiency of the more circular geometry is marginally lower in this case.
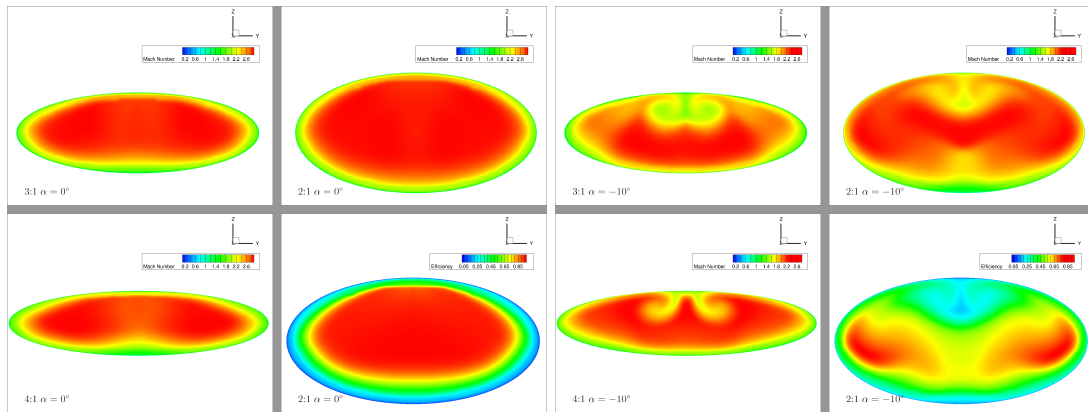
((a)) Effect of outlet shape variation on Mach number distribution and efficiency under on-design conditions ($\alpha = 0°$).

((b)) Effect of outlet shape variation on Mach number distribution and efficiency under off-design conditions ($\alpha = -10°$).
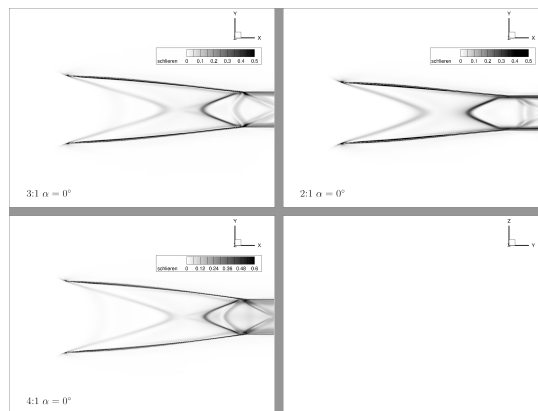
Figure 5.62: Schlieren visualizations showing the influence of outlet geometry on the shock structure under on-design conditions ($\alpha = 0°$).

Figure 5.63: Effect of angle of sideslip (β) variation on the mass-weighted average values of Mach number, static pressure, compression efficiency, and mass flow rate at the outlet for different ellipse ratio design.

Similarly, in Figure 5.63, which shows the variation of performance parameters as a function of the outlet ellipse shape, the same trend is observed across all three intake designs. The results confirm the earlier considerations: for this off-design condition as well, the closer the cross-sectional shape is to a circle, the higher the overall efficiency. This is consistent with the fact that more circular geometries approximate the idealized 2D axisymmetric conditions more closely, while increasingly flattened ellipse shapes deviate from this assumption, leading to reduced performance.

In addition to the drop in efficiency, the more flattened configurations exhibit a noticeable increase in static pressure compared to the more circular ones, indicating stronger compression. This is accompanied by a greater deceleration of the flow, further contributing to the performance degradation.
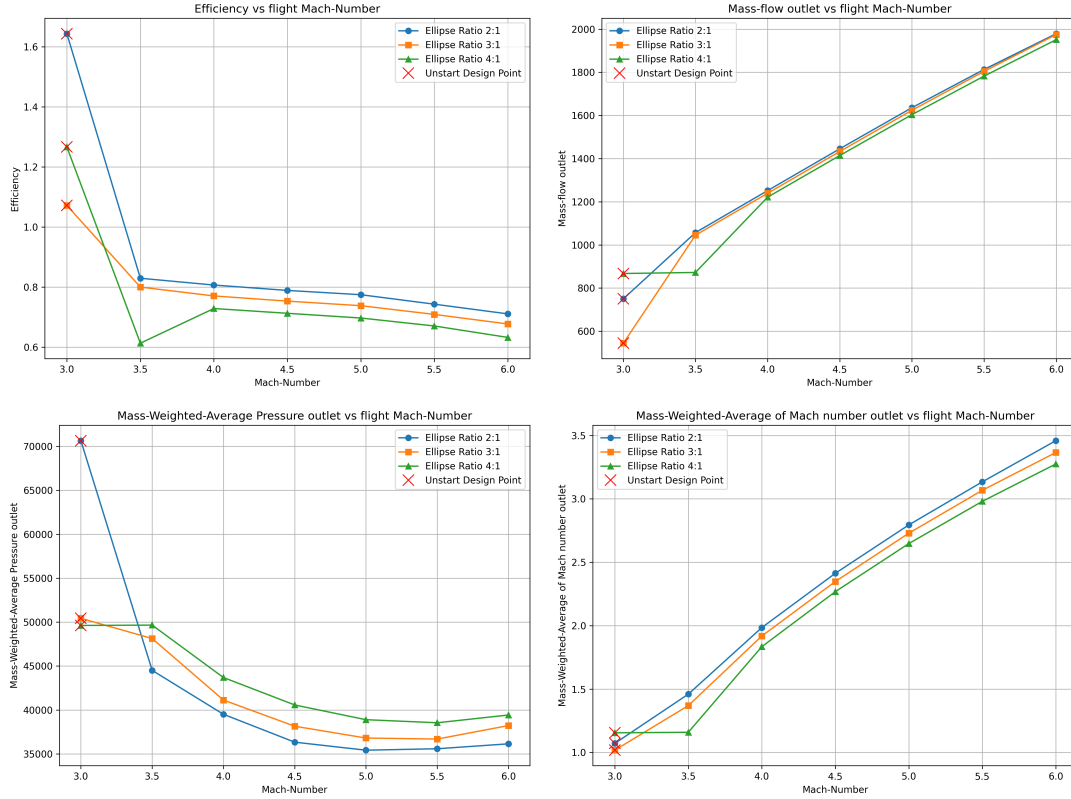
Figure 5.64: Effect of flight Mach number (M_∞) variation on the mass-weighted average values of Mach number, static pressure, compression efficiency, and mass flow rate at the outlet for different ellipse ratio design.

With respect to the variation of the freestream Mach number, Figure 5.64 shows that there is no significant difference in the behavior of the three intake designs. The unstart phenomenon occurs in all cases, as each design was developed for the same target downstream Mach number ($M_3 = 3$) and with identical outlet areas. Consequently, the area ratio remains constant across all configurations— a key parameter in determining whether the intake undergoes unstart.

Therefore, despite differences in outlet cross-sectional shape, the onset of unstart appears to be largely independent of the ellipse geometry. This suggests that geometric shape alone is not sufficient to mitigate unstart under off-design conditions governed primarily by area ratio and shock positioning.

The selection of the outlet cross-sectional shape must thus represent a trade-off between aerodynamic performance and integration constraints. From a performance perspective, a more circular cross-section leads to improved efficiency, as it better approximates the ideal axisymmetric flow conditions assumed during 2D design. However, more flattened shapes are often preferred for integration within the vehicle structure, and such constraints may outweigh the aerodynamic benefits in practical design scenarios.

Chapter 6

Conclusion

This thesis focused on the development and validation of an analytical tool for the design of two-dimensional and three-dimensional hypersonic Busemann-type intakes, with the aim of comparing the performance parameters of different configurations.

The initial part of the work was dedicated to the creation of a MATLAB-based design tool that, through the solution of the Taylor–Maccoll equations, allows the generation of a two-dimensional intake contour. Given a set of input parameters—the freestream Mach number M_∞, the target Mach number at the isolator entrance M_3, and the outlet radius—the tool iteratively computes the intake geometry to maximize total pressure recovery. This is achieved by optimizing the angle of the final conical shock and, consequently, the upstream Mach number, in order to exploit an initial isentropic compression surface and reduce total pressure losses.

A parametric analysis was then conducted to investigate the influence of M_3 on intake characteristics such as length, flow compression, and efficiency. Due to the elongated nature of the resulting geometries, a truncation angle δ was introduced to shorten the intake forebody, eliminating unnecessary length that does not significantly contribute to the compression process.

Initial inviscid simulations were carried out in *Ansys Fluent* to validate the analytical results by comparing them with CFD data. These comparisons confirmed the effectiveness of the tool and allowed for the evaluation of trade-offs between key performance parameters—compression ratio and efficiency.

Subsequently, viscous effects were taken into account to identify the deviations from the ideal inviscid model. A correction method was implemented, based on increasing the intake wall height by an amount corresponding to the boundary layer displacement thickness calculated from viscous CFD simulations. This adjustment improved the correlation between the analytical and numerical results under realistic conditions.

Transient simulations were also performed to study the unstart phenomenon in greater detail—a critical event in hypersonic intake operation that must be avoided during flight. These simulations helped identify the flow mechanisms responsible for intake unstart and contributed to the understanding of critical conditions.

The study then transitioned to the design and evaluation of three-dimensional intakes. Initially, an on-design case was analyzed for the configuration with $M_3 = 3$ and

truncation angle $\delta = 5°$, selected as a trade-off between performance and efficiency. A 3D geometry was constructed with an elliptical outlet section of 3:1 ratio, which represents a compromise between circularity—favorable for axisymmetric flow assumptions—and integration with the vehicle, which typically requires more flattened cross-sections.

The 3D intake was then tested under varying flight conditions, including angle of attack α, sideslip angle β, and freestream Mach number M_∞. A detailed analysis was conducted to understand how these parameters influence mass flow rate, outlet pressure, outlet Mach number, and overall efficiency. Critical off-design conditions leading to unstart were identified and discussed.

Following this, six different intake geometries were compared by varying either the degree of compression (the area ratio) or the shape of the outlet cross-section (ellipse ratio). The objective was to perform a comprehensive trade-off study between performance, robustness, and flow uniformity. It was shown that higher flow compression generally results in increased sensitivity to off-design conditions, with a greater risk of unstart. In contrast, intakes with lower flow compression exhibited greater robustness and reliability.

Regarding the variation of outlet cross-section shape, no significant influence on unstart behavior was observed as a function of the ellipse ratio. However, intakes with more circular sections demonstrated improved performance under on-design conditions, due to better alignment with the axisymmetric assumptions used in the Taylor–Maccoll-based design. Conversely, more flattened shapes—while beneficial for vehicle integration—resulted in lower overall intake efficiency.

In conclusion, the work demonstrated a complete design and validation workflow for hypersonic Busemann-type intakes, from analytical modeling to detailed CFD analysis. The findings emphasize the importance of balancing compression efficiency with off-design robustness and geometrical integration requirements, providing a useful framework for future hypersonic intake design studies.

6.1 Future Developments

Building upon the results obtained in this thesis, several future developments can be envisioned to further refine the analytical framework and improve the predictive accuracy of the intake design methodology.

First, the MATLAB tool developed for the analytical design could be enhanced by integrating empirical corrections to account for viscous effects. This would allow for more realistic performance estimates during the preliminary design phase and reduce the reliance on high-fidelity CFD in the early stages.

Regarding off-design analysis, the current study has investigated the variation of individual flight parameters—such as angle of attack, sideslip angle, and freestream Mach number—independently. A natural extension would be to explore combined off-design conditions, such as simultaneous variations of α and M_∞, or α and β, to gain a deeper understanding of how their interaction influences intake behavior. This would allow for a more comprehensive evaluation of flow distortions, pressure losses, and potential unstart phenomena under more realistic operational scenarios.

Moreover, future work could aim to develop a complete operational map of the intake

system by systematically evaluating a broader range of design and flight conditions. Such a map would serve as a valuable tool for assessing intake robustness and identifying safe operational envelopes, providing a 360-degree overview of intake performance across the entire design space.

List of Figures

List of Tables

Bibliography

[1]   M. K. Smart, "Scramjet inlets", in *RTO-EN-AVT-185*, NATO Research and Technology Organisation (RTO), 2014.

[2]   NASA. "X-43a hypersonic aircraft", NASA. (2024), [Online]. Available: https://www.nasa.gov/reference/x-43a/.

[3]   M. Berglund, K. Fedina, C. Fureby, J. Tegnér, and V. Sabel'nikov, "Finite rate chemistry large-eddy simulation of self-ignition in supersonic combustion ramjet", *AIAA Journal*, vol. 48, no. 3, pp. 540–550, 2010. DOI: 10.2514/1.43746.

[4]   D. Musielak, *Scramjet Propulsion: A Practical Introduction*, G. Pezzella and A. Viviani, Eds. John Wiley Sons Ltd, 2023, pp. 123–161.

[5]   D. M. V. Wie, "Scramjet inlets in scramjet propulsion", in *Scramjet Propulsion*, ser. Progress in Astronautics and Aeronautics, vol. 189, Reston, VA, USA: American Institute of Aeronautics and Astronautics (AIAA), 2001, pp. 447–511. DOI: 10.2514/5.9781600866387.0447.0511.

[6]   F. S. Billig and L. S. Jacobsen, "Comparison of planar and axisymmetric flowpaths for hydrogen fueled space access vehicles", in *Proceedings of the 39th Joint Propulsion Conference and Exhibit*, American Institute of Aeronautics and Astronautics (AIAA), 2003, pp. 1–12.

[7]   R. J. M. S, "Modular hypersonic inlets with conical flow", in *AGARD Conference on Hypersonic Boundary Layers and Flow-fields*, NATO/AGARD, 1968.

[8]   R. D. Seddon, "Parametric study of busemann inlets", Applied Physics Laboratory (APL), Johns Hopkins University, Tech. Rep. BBP Memo 77-128, 1977.

[9]   S. E. Molder, "Busemann inlet for hypersonic speeds", *Journal of Spacecraft and Rockets*, 1966.

[10] R. Courant, *Supersonic Flow and Shock Waves*. New York: Interscience, 1948.

[11] S. Mölder, "The busemann air intake for hypersonic speeds", in *Hypersonic Vehicles - Past, Present and Future Developments*, G. Pezzella and A. Viviani, Eds., IntechOpen. DOI: 10.5772/intechopen.82736.

[12] Heritage Concorde. "Air intake system". (2024), [Online]. Available: https://www.heritageconcorde.com/air-in-take-system.

[13] R. I. and L. W., "Design and development of an air intake for a supersonic transport aircraft", *AIAA Journal of Aircraft*, vol. 5, no. 6, pp. 513–521, 1968.

[14] F. S., "Tests at mach 1.915 on an air intake proposed for concorde", National Gas Turbine Establishment, Tech. Rep. Report No. R.290, 1967.

[15] T. Cain, "Ramjet intakes", in *RTO-EN-AVT-185: Lecture Series on Supersonic Intake Design*, Farnborough, UK: NATO Research and Technology Organisation, 2010.

[16] K. Oswatitsch, "Pressure recovery for missiles with reaction propulsion at high supersonic speeds (the efficiency of shock diffusers)", Tech. Rep., 1944.

[17] T. W., "High-velocity free-flying ramjet units (tr-missiles)", in *History of German Guided Missiles Development: AGARD First Guided Missiles Seminar*, Munich, Germany, 1956.

[18] S. Mölder and E. Timofeev, "Hypersonic air intake design for high performance and starting", in *RTO-EN-AVT-195: Lecture Series on Supersonic and Hypersonic Intake Design*, North Atlantic Treaty Organization, Research and Technology Organization (NATO RTO), Neuilly-sur-Seine, France: Educational Notes, RTO-EN-AVT-195, 2003, pp. 7-1–7-40.

[19] D. V. Wie and M. S., "Application of busemann inlet designs for flight at hypersonic speeds", in *Aerospace Design Conference*, American Institute of Aeronautics and Astronautics (AIAA), 1992.

[20] J. B. Keirsey, C. B., and S. M. L., "Design and test evaluation of a three module hypersonic inlet", Johns Hopkins University, Applied Physics Laboratory (APL/JHU), Tech. Rep. TG-699, 1965.

[21] A. J. T. Matthews, "Design and test of a modular waverider hypersonic intake", Department of Engineering Science, Oxford University, Tech. Rep., 2003.

[22] J. John D. Anderson, *Modern Compressible Flow with Historical Perspective*, 4th. New York, NY, USA: McGraw-Hill Education, 2021, ISBN: 978-1-260-57082-3.

[23] H. Babinsky and J. K. Harvey, Eds., *Shock Wave–Boundary-Layer Interactions* (Cambridge Aerospace Series). Cambridge, UK: Cambridge University Press, 2011, vol. 32.

[24] H. T. S. Alkasasbeh, "Numerical solutions for convective boundary layer flow over a solid sphere of newtonian and non-newtonian fluids", PhD thesis, Universiti Malaysia Pahang, 2015.

[25] National Advisory Committee for Aeronautics (NACA). "Supersonic inlets - nasa tm c-1955-37520". (1955), [Online]. Available: https://archive.org/details/C-1955-37520.

[26] A. Kantrowitz and C. d. Donaldson, "Preliminary investigation of supersonic diffusers", *NACA L5D20*, 1945.

[27] V. J. Babu, U. Pathak, and K. Sinha, "COMPARATIVE ANALYSIS OF RAMP-TYPE AND BUSEMANN INTAKES FOR HYPERSONIC AIR- BREATHING ENGINE", *Proceedings of the 1st National Aerospace Propulsion Conference*, 2017.

[28] A. Tognelli, "Multifidelity design and assessment of air intakes for high-speed propulsion systems", Master's thesis, Politecnico di Milano, 2021-2022.

[29] T. Drayna, I. Nompelis, and G. Candler, "Hypersonic Inward Turning Inlets: Design and Optimization", in *44th AIAA Aerospace Sciences Meeting and Exhibit*, Reno, Nevada: American Institute of Aeronautics and Astronautics, Jan. 2006. DOI: `10.2514/6.2006-297`.

[30] H. Ogawa, B. Shoesmith, S. Mölder, and E. Timofeev, "Viscous Correction and Shock Reflection in Stunted Busemann Intakes", in *Shock Wave Interactions*, K. Kontis, Ed., Cham: Springer International Publishing, 2018, pp. 179–196. DOI: `10.1007/978-3-319-73180-3_14`.

[31] Z. Zhao and W. Song, "Effect of Truncation on the Performance of Busemann Inlet", *Modern Applied Science*, vol. 3, no. 2, Jan. 2009. DOI: `10.5539/mas.v3n2p168`.

[32] D. Van Wie and S. Molder, "Applications of Busemann inlet designs for flight at hypersonic speeds", in *Aerospace Design Conference*, American Institute of Aeronautics and Astronautics, Feb. 1992. DOI: `10.2514/6.1992-1210`.

[33] M. Smart., "Design of three-dimensional hypersonic inlets with rectangular to elliptical shapre transition", in *Hypersonic Airbreathing Propulsuion Branch*, American Institute of Aeronautics and Astronautics, Feb. 1998.

[34] A. J. Matthews, T. V. Jones, and T. M. Cain, "Design and Test of a Hypersonic Isentropic-Spike Intake with Aligned Cowl", *Journal of Propulsion and Power*, vol. 21, pp. 838–843, Sep. 2005. DOI: `10.2514/1.13000`.

[35] E. Kreyszig, *Differential Geometry*. Dover Publications, 1991.

[36] J. (Fabri, "Air intake problems in supersonic propulsion", in *AGARD Combustion and Propulsion Panel Meeting*, ser. AGARDograph, Paris: Pergamon Press, Dec. 1958.

[37] C. O'Brien, "Analytical computation of leading-edge truncation effects on inviscid busemann-inlet performance", Aerojet, Sacramento, California 95813-6000, Tech. Rep., 2008.

[38] P. C. Walsh, R. B. Tahir, and S. Molder, "Boundary-layer Correction for the Busemann Hypersonic Air Inlet", en, *Canadian Aeronautics and Space Journal*, vol. 49, pp. 11–17, Mar. 2003. DOI: `10.5589/q03-003`.

[39] T. P. W. Holden and M. M. M. S. Holden, "Measurements in regions of shock wave/turbulent boundary layer interaction from mach 4 to 10 at flight duplicated velocities to evaluate and improve the models of turbulence in cfd codes", in *44th AIAA Fluid Dynamics Conference*, American Institute of Aeronautics and Astronautics (AIAA), 2014.

[40] C. J. Cook, "A new boundary-layer interaction technique for separated flows", NASA, Technical Memorandum NASA-TM-78690, 1978.

[41] J. H. Gusman and C. K. M. Gusman, "Best practices for cfd simulations of launch vehicle ascent with plumes - overflow perspective", in *49th AIAA Aerospace Sciences Meeting*, American Institute of Aeronautics and Astronautics (AIAA), Orlando, FL, USA, Jan. 2011.

[42]   H. Ogawa and M. S. B. R., "Effects of leading-edge truncation and stunting on drag and efficiency of busemann intakes for axisymmetric scramjet engines", *Journal of Fluid Science and Technology*, vol. 8, no. 2, pp. 186–199, 2013.

[43]   A. Rylov, "On the impossibility of regular reflection of a steady-state shock wave from the axis of symmetry", *Prikladnaya Matematika i Mekhanika (Prikl. Mat. Mekh.)*, vol. 54, pp. 200–203, 1990.

[44]   R. B. Tahir, S. Mölder, and E. V. Timofeev, "Unsteady starting of high mach number air inlets – a cfd study", in *39th AIAA/ASME/SAE/ASEE Joint Propulsion Conference and Exhibit*, American Institute of Aeronautics and Astronautics, Jul. 2003. DOI: 10.2514/6.2003-5191.